Title	Effect of Wave-Induced Vibrations on Structural Strength of Ships by CFD-FEM Coupling
Author(s)	Pal, Kumar Sumit
Citation	大阪大学, 2023, 博士論文
Version Type	VoR
URL	https://doi.org/10.18910/91963
rights	
Note	

Doctoral Dissertation

Effect of Wave-Induced Vibrations on Structural Strength of Ships by CFD-FEM Coupling

（CFD-FEM 連成による波浪中弾性応答が船体強度に与える影響の評価）

PAL SUMIT KUMAR

December 2022

Graduate School of Engineering,

Osaka University

Effect of Wave-Induced Vibrations on Structural Strength of Ships by CFD-FEM Coupling

By

PAL SUMIT KUMAR

A Dissertation for Doctor of Engineering Degree
submitted to Graduate School of Engineering

Department of Naval Architecture and Ocean Engineering

Osaka University

in

December 2022

Supervised by

Prof. Kazuhiro Iijima

Committee members:

Prof. Kazuhiro Iijima

Prof. Naoki Osawa

Prof. Munehiko Minoura

Abstract

High-frequency wave-induced vibrations can be broadly categorized into whipping and springing. While the hull girder transient vibration after slamming is known as whipping and can influence the hull girder safety, steady-state resonance vibration due to higher-order wave components is known as springing and can also cause accumulation of fatigue damage over the years. Therefore, from these concerns, consideration of these wave-induced vibrations in the hull girder design is very important. In this thesis, the effect of whipping and springing on structural strength is studied thoroughly with the help of Computational Fluid Dynamics (CFD)- Finite Element Method (FEM) coupling.

An in-house coupling method between CFD and FEM solvers is developed and validated against experimental results in the case of a flexible barge. First, rigid body motions are validated for frequency response functions together with time series comparisons. To consider the added-mass effect in the one-way coupling, the mass of the structure is artificially adjusted to obtain the same wet natural frequency from the numerical and experimental hammering test. It is found that the one-way coupling can give a good estimate of the wave-induced vibrations in comparison to the experimental results. A Reduced Order Model (ROM) is developed based on the CFD-FEM coupling to reproduce the target physical phenomenon more efficiently. In formulation of the ROM, transfer functions (TF) for rigid body motions, and normal wave-induced loads can be obtained by CFD-FEM, however, non-linear strip theory is used. A simple momentum theory can be a suitable candidate for the whipping model. This model is corrected against CFD-FEM coupling. A springing ROM is developed based on the experimental results and CFD-FEM coupling validation. The extreme value distribution of VBM is calculated using CFD-FEM coupling. The influence of springing, consecutive slamming at bow and stern in determining extreme value distribution are discussed. At the end, the effect of wave-induced vibrations on the hull girder collapse analysis is analyzed using CFD-FEM coupling method. Still water load (SWL) has been applied first, which results the containership to bend in hogging direction in calm water condition. Thereafter, a design wave load (DWL) has been applied using CFD, which pushes the structure further towards the ultimate hogging strength. Collapse behavior between one-way and two-way coupling results are compared and discussed.

Acknowledgements

Firstly, I want to express my sincere gratitude to my advisor Prof. Kazuhiro Iijima for his continuous support towards the completion of my thesis. I want to thank him for his constant encouragement, immense faith, and sharing his valuable knowledge in each and every aspect of this beautiful journey. His guidance helped me from the preparation of manuscripts to the final writing of this thesis.

I am also grateful to Prof. Masahiko Fujikubo and Asst. Prof. Akira Tatsumi for all the technical discussions we had and thankful for their valuable comments on my research. I appreciate the time, helpful criticism, and assessment of this thesis by Prof. Naoki Osawa and Prof. Munehiko Minoura, who serve on my dissertation committee. I appreciate Ms. Sachi Chayama, the laboratory secretary, for making the administrative process simpler for me.

I would like to address special thanks to Dr. Tomoki Takami of NMRI for his help in completing this research by providing the necessary data and giving suggestions. I am also very thankful to Mr. Tomoki Ono for his precious contribution towards completion of this thesis. I extend my appreciation to all the current and previous laboratory members who helped me in various ways during this journey.

This study was made possible by the financial support of the Japanese Government (MONBUKAGAKUSHO: MEXT Scholarship). Without this financial support I could not complete this work. Also, I am very grateful to Prof. Kazuhiro Iijima for the financial support toward the end this journey.

To my friends, I am eternally grateful for your unwavering companionship and the unforgettable memories we have shared.

Last but not the least, I would like express my deepest appreciation to my parents and brother for their unwavering support and love throughout this journey.

Contents

List of Figures

List of Tables

1 Introduction

1.1 Background and Motivation

In the design of a ship hull structure, one of the most important aspects is its strength as a hull girder, as it should be higher than all the loads it is going to experience during its service life. Therefore, the evaluation of the extreme load events and their consequences on the structural integrity is prerequisite from the viewpoint of engineering risk analysis. In the recent past, due to inadequate buckling strength in the way to the engine room and the contribution of increased load due to whipping, caused the failure of the MSC Napoli in 2007 [1]. Also, one of the causes behind the accident of MOL COMFORT in 2013 [2] was increase of VBM due to transient vibrations. Usually in severe seas, when the ship may undergo extreme loads due to slamming, hull girder vibrations increases significantly (i.e., whipping). Due to increase in global trade, the size of containerships is getting larger, which makes the structure more flexible and vulnerable to damage due to increased transient vibrations. Other than the effect of extreme wave loads, fatigue and corrosion could also be possible sources of weakness in the structural failure of Prestige in 2002 [3]. Exposure to the steady state resonant vibrations (i.e., springing) can reduce the fatigue strength of the structure. In the case of whipping, transient vibrations can increase the VBM, which influences the ultimate hull girder strength and long-term distribution of whipping bending moments (Derbanne et al., [4]; Ćorak et al., [5]). On the other hand, springing can also cause accumulation of fatigue damage over years. Therefore, to avoid such scenarios, a systematical study on these wave-induced vibrations in the hull girder design is very important.

In order to investigate the effect of wave-induced vibrations on the hull girder, the fluid and the structure models are needed to be coupled together. For the structural modelling a robust and efficient method like Finite Element Analysis (FEA) can be a suitable choice. On the other hand, for the fluid modelling, the direct use of potential theory-based code can be very effective in terms of time constraints and computational power. Recently, Riesner and Moctar [6] used the Rankine source Boundary Element Method (BEM) in time domain coupled with elastic beam element to study the global resonant vibrations of ships. However, when it comes to the robustness in modeling any structures, or capability to calculate preciously phenomenon like slamming, springing, green-water on deck, or simply free surface nonlinearity, it is logical to use Reynolds Average Navier-Stokes (RANS) based solvers to some extent.

With the advancement of computers, more and more researchers are inclining toward the application of CFD-FEM coupling for an understanding of complicated physics involved in naval hydrodynamics. Seng et al. [7] coupled OpenFOAM and modal superposition approach to perform hydroelasticity of an elastic barge. Recently many researchers (Lakshmynarayanana and Temarel, [8]; Jiao et al., [9]) used STAR-CCM+ and Abaqus co-simulation software to study the whipping and springing phenomenon of a S175 containership. Takami and Iijima [10] calculated VBM and double bottom bending moment (DBM) using inhouse coupling between STAR-CCM+ and LS-DYNA solvers. They mentioned the time taken per 10s simulation of a full-scale model is 29.4 hours for strong coupling. Moctar et al. [11] used domain separated approach to couple RANS equations with Timoshenko beam theory. For calculating and validating exceedance probability they chose the wave of duration 30 min in full scale in both numerical and experimental cases in order to avoid cost-intensive simulations. However, to derive an accurate estimate of extreme value predictions one needs a much higher duration of sample data.

To overcome the time constraint, the use of extreme value statistics in the development of hydroelastic methods became popular. Der Kiureghian [12] offered a new outlook on linear systems subjected to Gaussian or non-Gaussian excitation by detailing approximate solutions using the first and second-order reliability methods (FORM and SORM). Jensen [13] presented the extreme value vertical bending moment of a containership using FORM by considering the nonlinearity of wave load and flexibility of the hull. Garre and Der Kiureghian [14] used the frequency domain Tail Equivalent Linearization Method (TELM) for the analysis of the nonlinear sway displacement of a jack-up platform subjected to Gaussian waves. Choi et al. [15] applied FORM to improve extreme value prediction for non-linear parametric roll motion of ships. Pal et al. [16] used First Order Reliability Method (FORM) together with the Reduced Order Model (ROM) to capture the exceedance probability of whipping-induced VBM at a lower probability range. The influence of the initial design point on finding the minimum distant point in the limit surface was pointed out. The results were compared with the crude Monte Carlo (MC) method with or without important sampling and Markov Chain Monte Carlo (MCMC) methods. The methods like MC where direct sampling is taken using random variables are always better as a brute force technique. The solution of these statistical models largely depends on being able to correctly analyze the hydrodynamics load effects like impact bow-stern slamming and green water on deck.

In order to accurately capture the extreme value distributions, modeling an accurate Reduced Order Model (ROM) is very necessary. Seng and Jensen [17] used nonlinear strip theory as a predictor step and CFD as a corrector step to calculate the extreme value distribution of VBM. They attempted to use a Model Correction Factor (MCF) in order to resolve the difference between two responses in deriving reliability indices. However, in their method, inaccuracy in modeling the whipping response affected the extreme value distributions directly. Bow and consecutive stern slamming are mentioned by Seng and Jensen [17]. However, the extent of it was unable to get predicted using their ROM and overestimated the result by about 29 % from CFD. Takami et al. [18] used nonlinear strip theory for calculating the wave-induced load and added whipping induced component based on the impulse response function of slamming impact force based on momentum theory.

The study on the effect of springing in floating structures already started a long time ago (Van Gunsteren, [19]). As the fluid solver is very important in order to capture the springing phenomenon, it was limited to mostly linear springing only. However, with technological development use of RANS equation-based solver can be used in capturing springing more accurately (Lakshmynarayanana and Temarel, [8]; Jiao et al., [9]). Recently, current authors pointed out the capability of one-way CFD-FEM coupling to capture the springing phenomenon of a barge-type structure and validated it with an in-house experiment. Therefore, CFD-FEM one-way coupling would be useful to correct the springing ROM (Pal et al., [20]; Pal and Iijima, [21]).

In the previous research, Takami et al. [18] compared extreme value distributions of slamming-induced whipping VBM calculated from ROM+FORM with the experimental result. However, there are considerable disagreements in the tail of the probability of exceedance (PoE) curve with the experiment. It can be due to insufficient tuning of the ROM with CFD-FEA or a mismatch of physical phenomena involved with the experiment and ROM. The concept of ROM is to reduce the high-fidelity models into lower dimensions by just modeling specific phenomena of interest. Therefore, an improvement of ROM is necessary to calculate the extreme value distributions.

While an accurate evaluation of the extreme value distribution of VBM is important, analysis of the effect of wave-induced vibration on the hull girder collapse behavior is also important to understand the severity of collapse and consequences beforehand. Failure of the hull girder under the extreme waves is a catastrophic circumstance as it is directly associated with the loss of ship, cargos, and human lives, etc. Hence, the investigation of the post-ultimate strength behavior of floating structures in extreme waves is very necessary for contributing to the existing rules and regulations on the ultimate strength.

In the past, researchers tried to simulate such failure analysis through numerical or some experimental measures, such as: Caldwell [22] attempted to evaluate the ultimate ship strength using the rigid plastic mechanism analysis where he accounted the effect of buckling reducing the yield stress of the material at the buckled part. Masaoka et al. [23] used an intact and damaged hollow thin-walled box structure for analyzing elasto-plastic dynamic behavior in large regular waves, where the wave loads are calculated using strip theory. Yao et al. [24] simulated the progressive collapse behavior of a ship's hull girder considering Smith's method [25]. Xu et al. [26] used analytical solution to investigate post-ultimate strength behavior of a ship hull girder for an arbitrary sinusoidal load. However, these studies do not focus on the effect of dynamic fluid-body interactions on collapse analysis.

In this regard, the post-ultimate strength behavior including the fluid-structure interaction was investigated using a segmented model by Iijima et al. [27]. Pei et al. [28] used potential flow theory to exert pressure time history on a bulk carrier to examine the collapse analysis. In their calculation it is assumed that the loads are not influenced by the progress of collapse. Recently, Han et al. [29] used sinusoidal half wave load on a containership to analyze collapse behavior using Smith's method. They included added mass and damping effect separately to study the effect on the analysis. However, the effect of deformation on the calculation of the external load is not considered.

Therefore, in this thesis, a direct coupling between CFD and FEA is used to investigate the hull girder collapse analysis. A direct coupling between CFD and FEA to understand the failure has not been studied in the literature. A direct coupling between CFD and FEA has certain benefits, such as: (i) incorporation of structural and fluid non-linearities is easier (iii) hydroelastic effect on collapse analysis (iv) applicability of the method to any other structures (v) effect of nonlinear phenomenon like springing, slamming induced whipping can be studied. Takami and Iijima [10] developed a direct coupling method between CFD and FEM in previous studies to investigate local and global hydroelastic effects. In this thesis, the same coupling method has been extended towards elasto-plastic analysis.

1.2 Research Objectives

The objective of this thesis can be summarized as follows:

- An in-house one-way and two-way coupling method between CFD and FEM is developed and validated against experimental results for the rigid body motions and vertical bending moment.
- To investigate springing phenomenon with the help of one-way and two-way coupling methods in case of a flexible barge. Two-way coupling is used to perform a numerical hammering test to obtain the wet natural frequency of the hull and compare it with experiment. It is found that the one-way coupling can give a good estimate of the wave-induced vibrations when the mass is artificially increased to account for the added mass effect. Calculated springing vibrations are compared with experiment in case of vertical bending moment time series for different wave frequencies.

- A ROM is developed based on CFD-FEM coupling to reproduce the target physical phenomenon more quickly. Inside the ROM, transfer functions (TF) for rigid body motions, and normal wave-induced loads can be obtained by CFD-FEM, however, nonlinear strip theory is used. The TF of normal wave load is corrected for sagging-hogging nonlinearity by using CFD-FEM coupling.
- A simple momentum theory can be a suitable candidate for the whipping model. This model is also corrected against CFD-FEM coupling.
- To develop a springing ROM based on the experimental results and CFD-FEM coupling validation.
- To calculate the extreme value distribution of VBM using CFD-FEM coupling. The influence of consecutive slamming at bow and stern in determining extreme value distribution is discussed.
- To investigate the effect of wave-induced vibrations on the hull girder collapse analysis using CFD-FEM coupling method. Collapse behavior between one-way and two-way coupling results are compared.

1.3 Organization of Thesis

In Chapter 1, the background and motivation of this problem statement is elaborated with current research objectives.

In Chapter 2, an in-house coupling method between CFD and FEM for a floating body is detailed for one-way and two-way coupling schemes. In the one-way coupling, the hydrodynamic pressures derived from CFD, are mapped into the FE model to calculate structural responses. In this case, the deformation of the structure is not further fed back to the CFD model. However, in the case of two-way coupling, the structural deformation calculated using FEM fed back into CFD. Overset mesh approach is used to stabilize the CFD solver during morphing process. Since, the hydroelasticity problem is solved using domain separated approach, to converge the pressure to the corresponding deformation, inner iterations are performed at each time step. The accuracy and effectiveness of these two schemes are discussed as well.

In Chapter 3, the validity of the aforementioned coupling method is shown in comparison with experimental results. For the validation, a simple modified barge has been chosen as a test subject. First, rigid body responses of the barge are validated for different Response Amplitude Operators (RAOs) together with time series comparisons. Since the added mass effect is automatically considered in two-way direct coupling method, hammering test is performed to know the wet natural frequency of the structure. Upon comparison of the wet natural frequency with experiment, the same is adopted in the one-way coupling structure model. This method is chosen to eliminate the drawback of the high computational cost of the two-way coupling method. Later, the flexible vertical bending moment time series derived from the numerical analysis are compared with the experiment.

In Chapter 4, the utilization of a Reduced Order Model (ROM) is discussed, which will be used further to study the effect of wave-induced vibrations on shipload. A correction factor is introduced to adjust the difference between ROM prediction and CFD-FEM result. Components related to Froude-Krylov, whipping, and springing are modeled separately and superimposed for calculating total VBM. The developed ROM is used with First Order Reliability Method (FORM) to design a Maximum Probable Wave Episode (MPWE), which is considered as an input wave field.

In Chapter 5, the proposed ROM is validated against the experimental results for an extreme value distribution of VBM. Probability of exceedance at various target VBM are compared for ROM and experiment. The effectiveness of the current ROM in capturing complicated behaviors like a consecutive bow and stern slamming is discussed. The effect of the inclusion of springing ROM in extreme value distribution is also discussed herein.

In Chapter 6, the mentioned coupling schemes between CFD and FEM has been chosen to analyze and understand the effect of direct coupling in ultimate strength assessment of a hull girder under extreme wave condition. The obtained collapse behaviors from one-way and two-way couplings are compared and discussed in global and local scales.

In Chapter 7, the conclusion of the current study is discussed with suggestions for future work.

2 Coupled CFD-FEM Model

In this study, the CFD and FEM coupling is considered using domain separated approach. In the following subsections, the modeling of fluid domain, structure domain, and their coupling scheme is discussed elaborately.

2.1 CFD Modelling

The fluid domain is modeled in STAR-CCM+ 14.06.012 CFD solver [30] using the Finite Volume Method (FVM). Water and air phases are considered to capture free surface using the volume of fluid (VOF) formulation. An overview of the whole domain with the free surface can be seen in Figure 2.1. First the whole domain is discretized into finite volumes. Then, the numerical method involves solving the governing mass and momentum equations (2.1-2.2) over each discretized control volume. In equations (2.1-2.2), u is the velocity vector, g is the gravitational acceleration vector, and ρ is the volume-fraction-averaged density. To represent the volume of q^{th} phase fluid in a cell a volume fraction term (a_q) is multiplied with fluid density ρ and fluid dynamic viscosity μ (equation 2.3). Thereafter, Semi-Implicit Pressure Linked equations (SIMPLE) are used to achieve an implicit coupling between pressure and velocity.

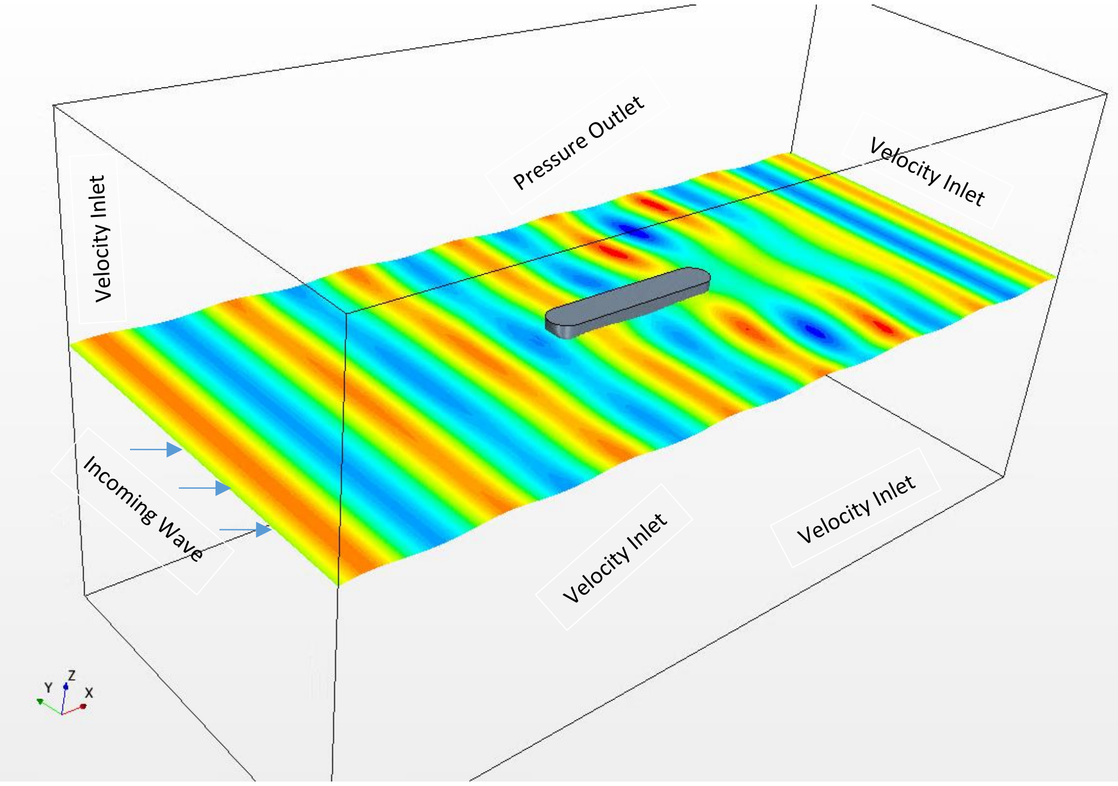

Figure 2.1 CFD domain used in this study

$$\frac{\partial \rho}{\partial t} + \frac{\partial}{\partial x_i}(\rho u_i) = 0 \tag{2.1}$$

$$\frac{\partial}{\partial t}(\rho u_i) + \frac{\partial}{\partial x_j}(\rho u_i u_j) = -\frac{\partial p}{\partial x_i} + \frac{\partial}{\partial x_j}\left[\mu\left(\frac{\partial u_i}{\partial x_j}\right)\right] + \rho g_i \tag{2.2}$$

$$\rho = \sum_{q=1}^{2} a_q \rho_q \tag{2.3}$$

All the boundaries are illustrated in Figure 2.1, where each boundary is considered as a velocity inlet except the top boundary as a pressure outlet. The size of the domain is shown in terms of ship particulars in Table 2.1 Water is modeled as a constant density incompressible fluid and air is modeled as an ideal gas. For the turbulence model $k - \omega$ model was chosen. The solution has been achieved using an unsteady implicit approach. The overview of the meshing is shown in Figure 2.2 in XZ, XY, and YZ planes. The overset mesh approach has been chosen to accurately capture the dynamics of the hull. In Figure 2.2, the red-colored mesh is the overset mesh and the black-colored mesh is the background mesh. At each time step first the governing equations are solved in the background region, then solution values are transferred in the overset region using linear interpolation. To capture the flow dynamics around the hull, a finer mesh is used, which is subsequently faded away from the hull. To avoid any interpolation error, the around region and overset region are discretized with the same mesh quality. In free-surface, at least 10 grids are considered along the height of the wave, to accurately capture the wave. The details of the mesh are shown in Table 2.1. In Table 1.1 H_w , T_w , L are wave height, wave time period, and length of the ship respectively.

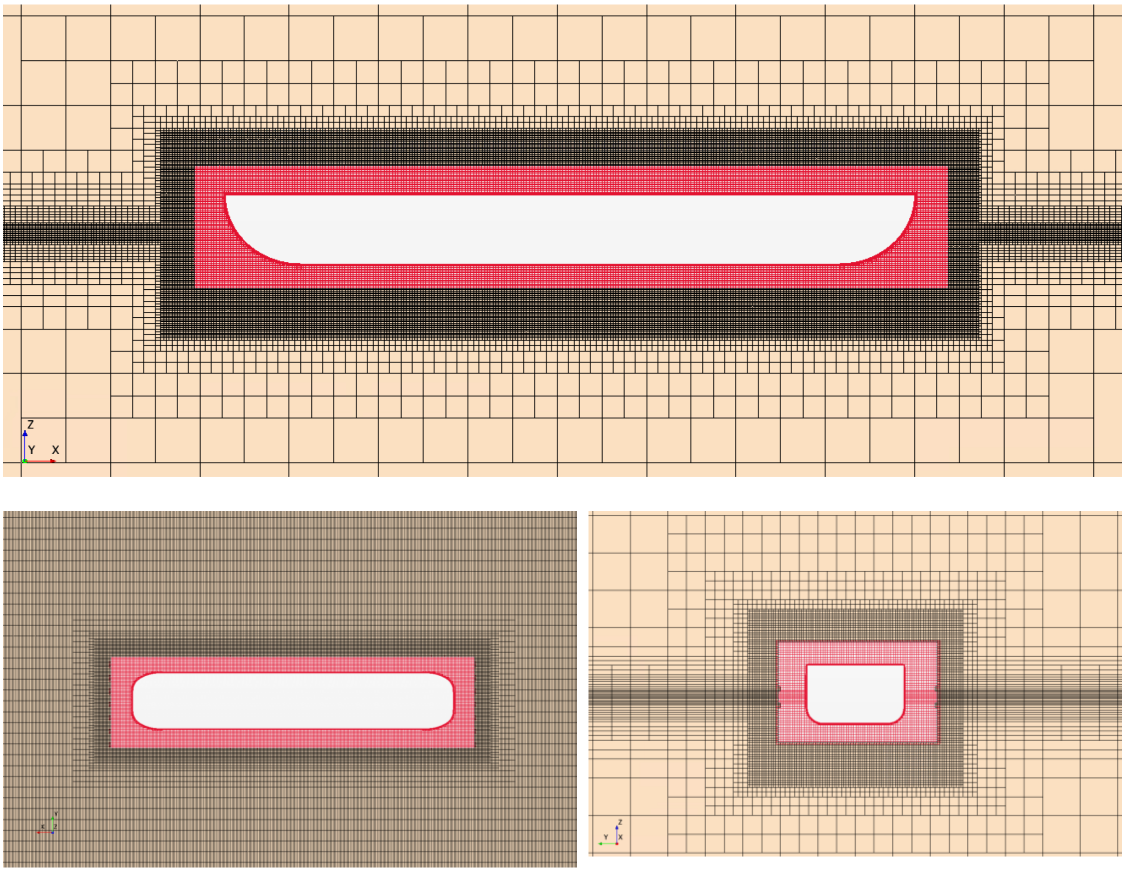

Figure 2.2 Mesh layout of the model with mesh refinement at free-surface and around the body

Table 2.1 Domain and mesh sizes

dx	dy	dz	dt	Domain size ($L \times B \times D$)
$2dz$	$10dx$	$H_w/10$	$T_w/500$	$4L_{pp} \times 12B \times 25D$

To avoid the problem of reflection from boundaries, VOF wave forcing is used. In VOF wave forcing the solution of the discretized Navier-Stokes equations is forced towards another simplified numerical solution over a specified distance, therefore, reduces the computing effort by using a reduced-size solution domain [30]. In Figure 2.3, the relative zone distance of VOF wave forcing at boundaries is plotted. From the color bar, it can be observed that the magnitude of the VOF wave forcing is slowly decaying away from the boundary and merges at the end of the defined zone. The length of the zone is considered as 1.5 m upstream and downstream, and 0.2 m at side boundaries. The proportions of the mentioned zone length to the size of the domain are kept same for all the simulations. These lengths of forcing zones are chosen from experience by always keeping a sufficient distance away from the hull so as to not affect the flow field near it. While starting the simulation, to avoid sudden initial transient body-structure interaction, a ramp function equal to one wave period has been applied for all simulations.

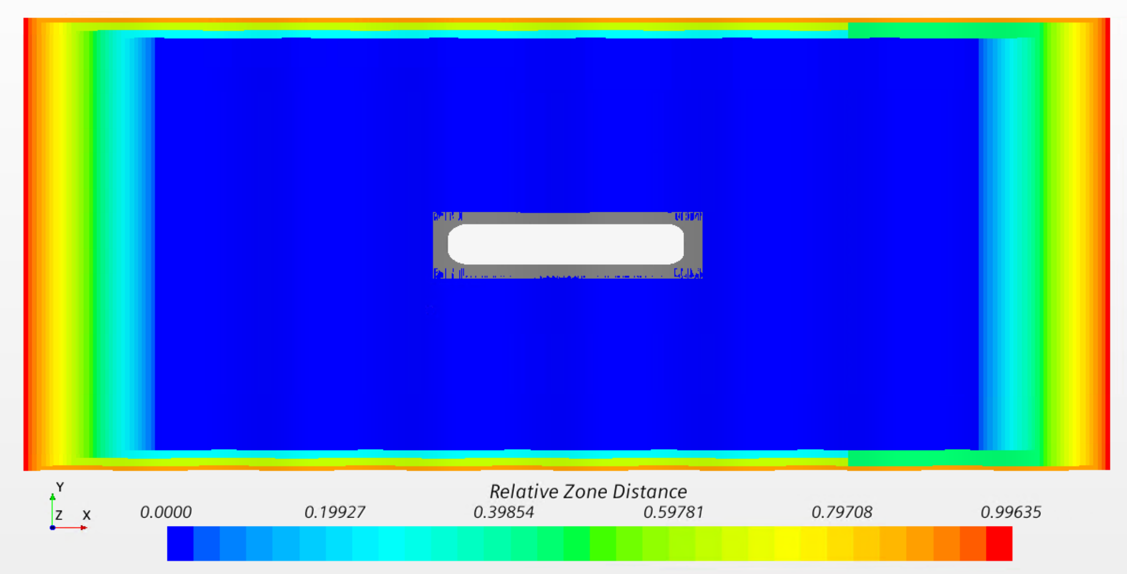

Figure 2.3 Depiction of the VOF wave forcing zones over the free surface

2.2 FEM Modelling

Throughout this thesis there are three Finite Element (FE) models are considered for different purposes of the study. There are one-dimensional (1D) beam model (Figure 2.4), three-dimensional (3D) backbone shell model (2.5), and 3D outer shell - backbone model (Figure 2.6). In case of 1D beam and 3D backbone shell model, sectional forces are applied (discussed further in the next subsection). For the 1D beam, sectional force is applied at every node along the length. For the 3D backbone shell model, sectional force is applied at the master node of each section, which is connecting the backbone shell elements through rigid beams in the same cross-sectional plane. A nodal rigid body system is shown in Figure 2.5 which consists of the defined nodes of the shell elements. This means, the motion of the connected part (i.e., slave nodes) is governed by the motion of the master node. For the 3D outer shell-backbone model, outer shell (i.e., hull of the subject ship) is connected to the backbone using the same rigid beams. The structural model is analyzed in a commercial FE solver LS-DYNA [31]. Only X-translation, Ztranslation, and Y-rotational movements are allowed at each node. However, to suppress the surge motion of the FE model, a node near the center of gravity (CG) is constrained in the X direction. The dynamic explicit solver is used for FE analysis. The time step size is automatically chosen by the LS-DYNA solver which is equal to 3.77E-06 s. It can be seen that the time-step size is far smaller than the CFD time-step size. In this section only, general modelling details of the structure domain is shown. The same modelling technique has been used for 6600 TEU containership (used in Chapter 5) and 5250 TEU containership (used in Chapter 6). Therefore, the mass distribution and other specific model properties are shown chapter wise.

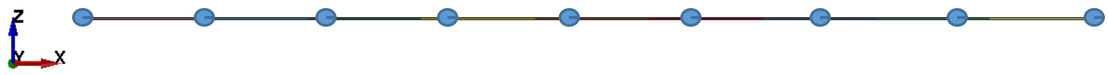

Figure 2.4 One-dimensional beam model

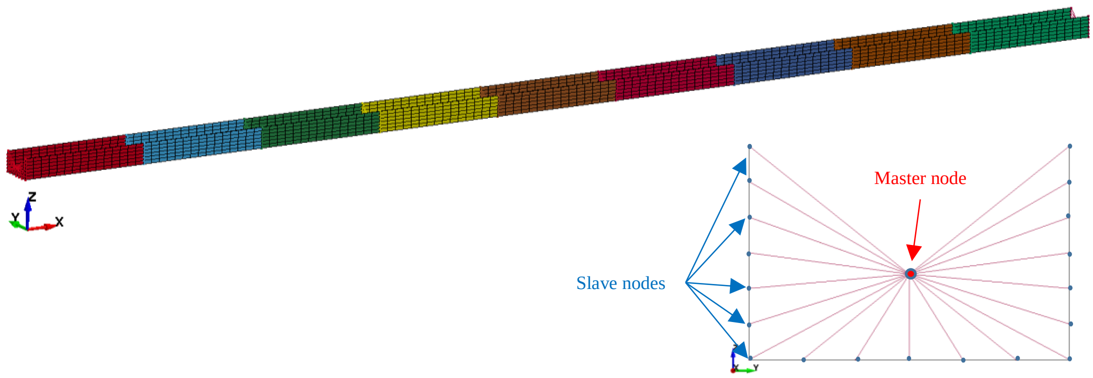

Figure 2.5 Three-dimensional backbone shell model

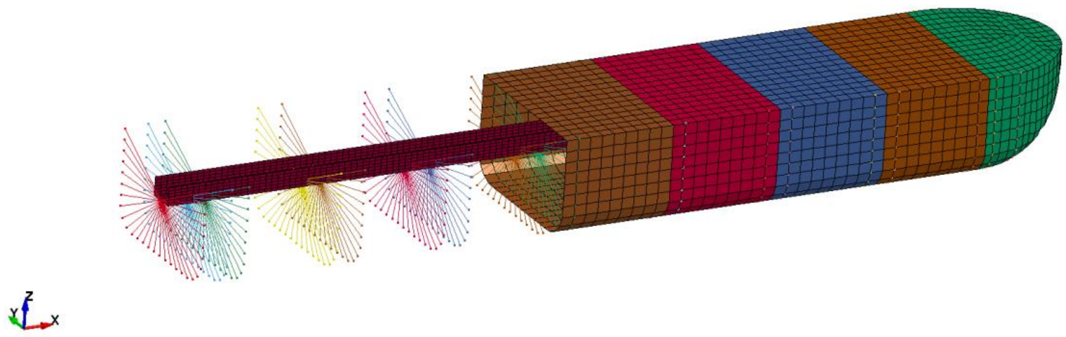

Figure 2.6 Three-dimensional outer-shell - backbone model

Rayleigh damping model has been chosen with mass proportionality co-efficient α determined from the 2-node vertical bending vibrational frequency (f_{2n}) of the experiment from equation (2.4). The logarithmic damping ratio, δ is calculated from the hammering test of the experimental model.

$$\alpha = 2\delta f_{2n} \tag{2.4}$$

2.3 One-way Coupling

The calculated pressures at CFD grids are converted to sectional loads at locations corresponds to FE nodes (Figure 2.4-2.5) to carry out the structural analysis. FE mesh and CFD grids are shown in Figure 2.7. First, the pressure at CFD grids is mapped into the FE model using Inverse Distance Weighting (IDW) method, which is shown in equation (2.5).

$$P(x, y, z, t) = \frac{\sum_{i=0}^{N} w_i P_i(x_i, y_i, z_i, t)}{\sum_{i=0}^{N} w_i} \tag{2.5}$$

where, $w_i = 1/((x - x_i)^2 + (y - y_i)^2 + (z - z_i)^2)$

In equation (2.5), $P(x, y, z, t)$ is the pressure at a FE node at time t, $P_i(x_i, y_i, z_i, t)$ is the pressure at i^{th} CFD grid, and w_i is the inverse of the distances between CFD grids and the target FE node. In this study, N is chosen as 4, which is the number of the nearest nodes used for mapping. The mapped pressure is then converted to force by multiplying the area and normal vector of each panel in the FE mesh. The obtained element forces are converted to nodal forces in the FE model using equation (2.6).

$$f_{ZFEA,i}(t) = \int_{L_i} f_{zCFD}\,(x, t)dx \tag{2.6}$$

Here, $f_{ZFEA,i}$is the vertical force acting on the i^{th} FE node, $f_{zCFD}$is the vertical force acting on the hull at coordinate x, and $L_i$is the length of the integral range.

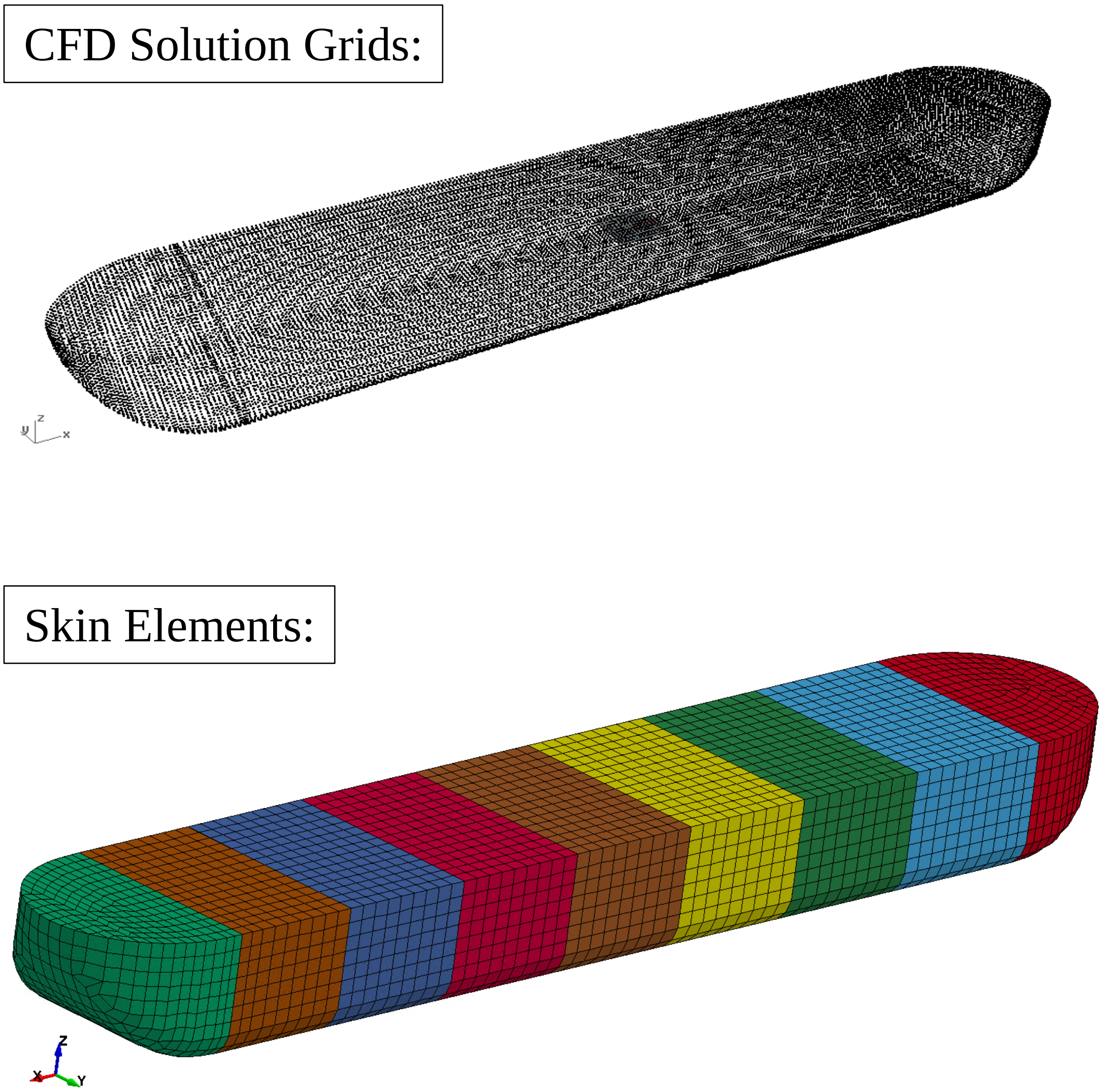

Figure 2.7 CFD grids and skin elements of the subject hull for mapping

The overview of the one-way coupling method is illustrated in a flowchart in Figure 2.8. In the flowchart, at $t = t_0$ the CFD solver starts the simulation and exports the pressure profile. Then pressures at discrete grids are mapped into center of each defined FE panel (Figure 2.6) using IDW method (Equation 2.5). Later, pressures are converted into forces at each shell elements, and then turned into sectional force by integrating it over the length. In this study, the sectional load is applied to the Figure 2.4-2.5 models and pressures are directly applied to the Figure 2.6 model. Therefore, one-way coupling can be executed by any of these models. From Figure 2.8 it can be seen that, at each timestep the inertia force is exported from the CFD solver. As the slightest difference in the total load after and before mapping can cause accumulation of the error and result in an imbalance system, inertia force at each timestep is imported to the mapping code from the CFD solver to balance out. It can also be noticed from the flowchart that the calculated deformation from the FEA solver is not further fed back into CFD. In other words, there is no effect of structural global or local deformation on the calculated pressure profiles in CFD solver. Hence it is named as one-way coupling method in this thesis.

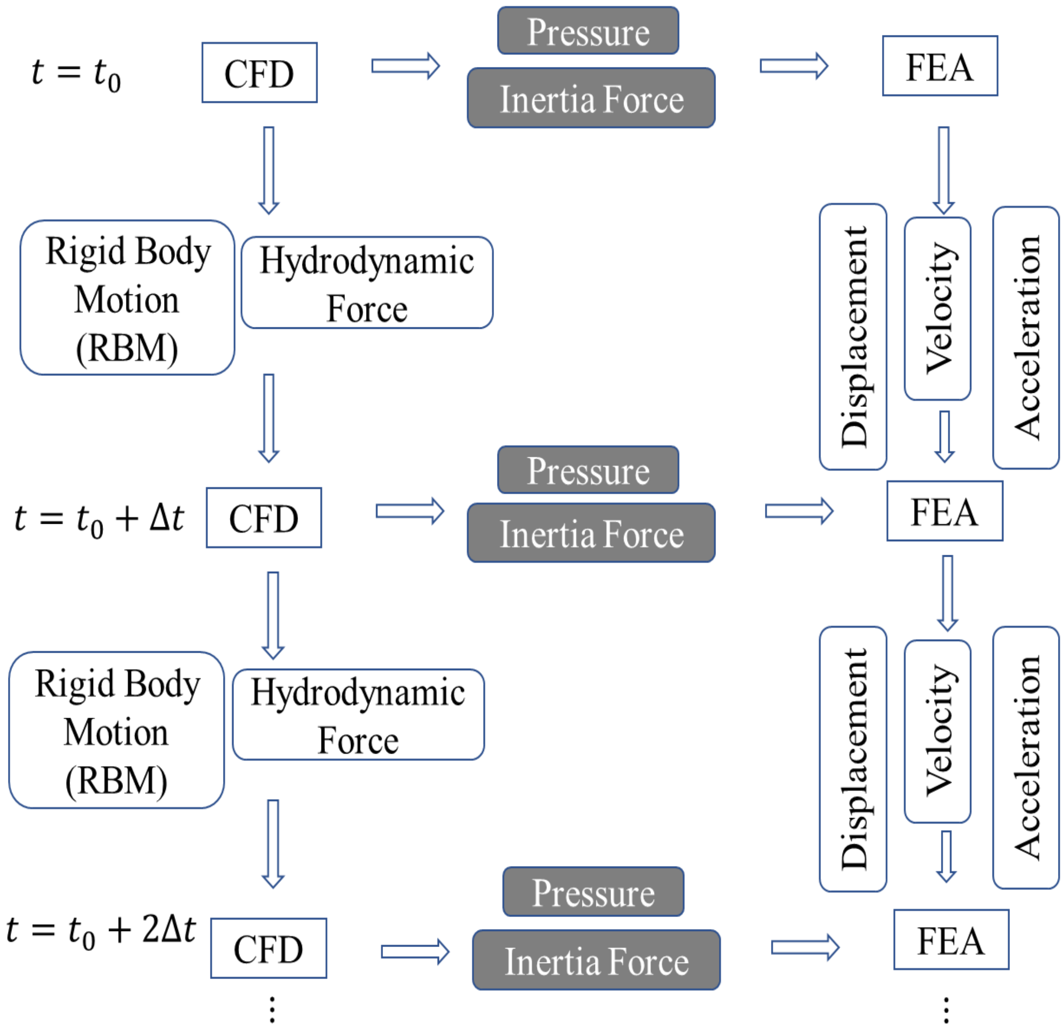

Figure 2.8 Flowchart of the one-way coupling method

2.4 Two-way Coupling

Two-way coupling procedure is explained in a flowchart in Figure 2.9. The whole procedure can be summarized as follows:

- At time $t = t_0$, the CFD solver is run and advanced to the next time step. In this step, the original shape of the structure is same and considered as rigid body.
  - At time $t = t_0 + \Delta t$, previously run CFD solver is further advanced to the next timestep considering zero deformation of the structure. At this timestep, pressure profile and as well as inertia force are transferred to the in-house mapping code.
  - The balance between total force and the inertia force is checked and using IDW method (equation 2.5) the pressure on discrete CFD grids are mapped on to centroid of defined panels on the FE mesh (Figure 2.7).
  - Displacement on the FE solver is calculated based on the current pressure profile on the hull surface. Due to the application of the pressure the hull experiences rigid body displacement and as well as deformation. As the outer shell is connected to the elastic backbone, the backbone also experiences the same.
  - As the STAR-CCM+ solver already contains the Rigid Body Motion (RBM), only the deformation of the structure is used as an input for the morphing solver. Therefore, to remove RBM from the displacement heave and pitch components are calculated separately. The heave motion (Δx_3) is calculated by tracking the translational displacement of the CG of the structure model. The

translational displacement is calculated by equation (2.7), where z_i, m_i are the displacement and mass of the i^{th} FE node. The pitch motion (Δx_5) is calculated by least square method of the vertical displacement of the FE nodes at the centre line of the backbone.

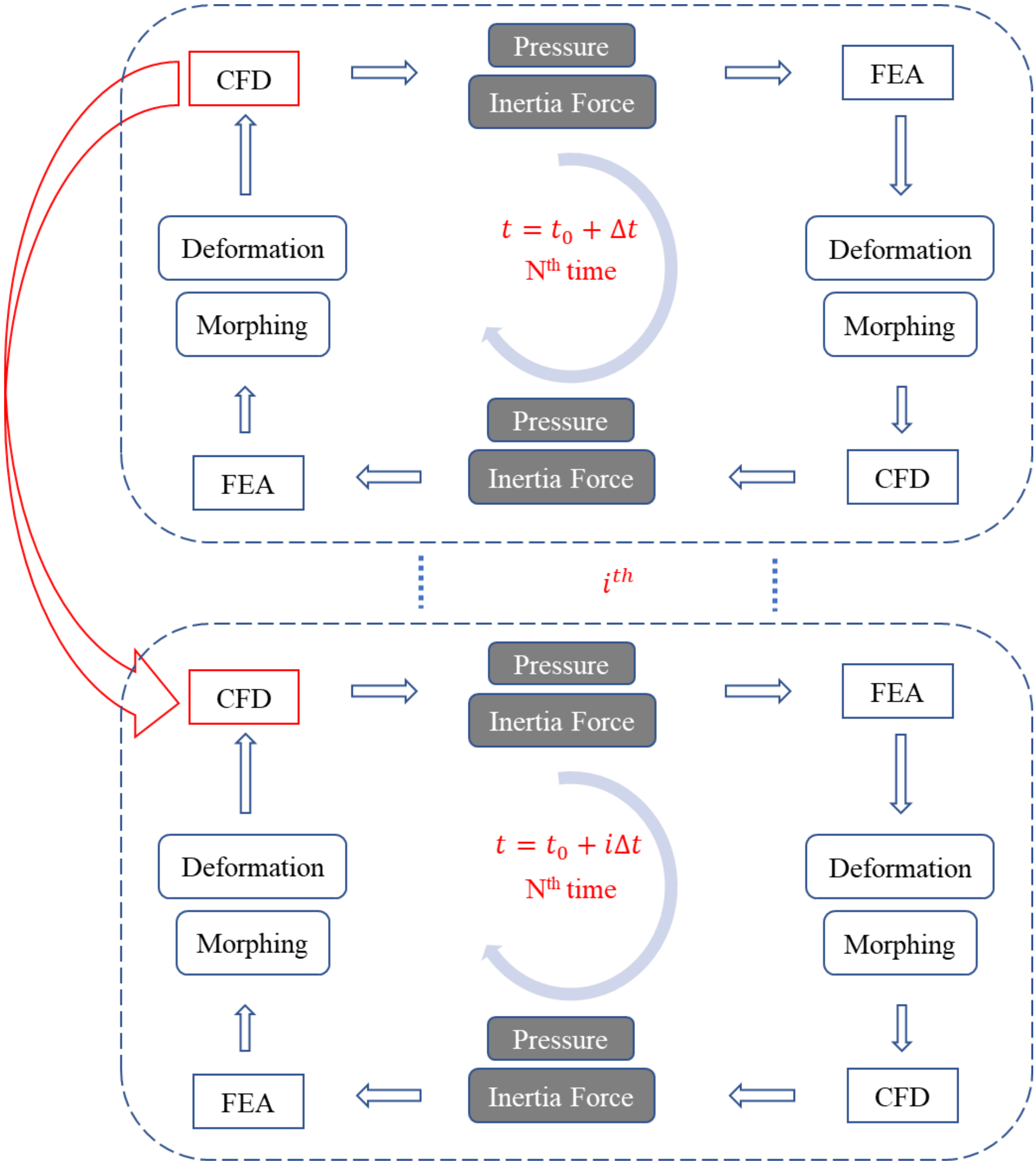

Figure 2.9 Flowchart of the two-way coupling method

$$x_3(t_0 + i\Delta t) - x_3(t_0 + \Delta t) = \frac{\sum_i^{Nnode} m_i\{z_i(t_0+i\Delta t)-z_i(t_0+\Delta t)\}}{\sum_i^{Nnode} m_i} \tag{2.7}$$

- After morphing the structure using calculated deformations, the updated pressure profile is calculated at the time $t = t_0 + \Delta t$ and continued the same procedure until there is convergence of pressure.

- After the convergence, the simulation is proceeded for the time $t = t_0 + 2\Delta t$ and so on.

The current two-way coupling method is based on exchanges of pressure and displacement profiles in the form of a file between two separate solvers, hence it is time consuming. Currently, for the two-way coupling simulation in model scale it takes around 1 day for 1s for 3 inner iterations. While increasing the number of iterations would be better it certainly going to take more time. Hence, Aitken's accelerator [32] is used to find approximate convergence to the solution after three inner iterations using the equation (2.8).

$$P(i\Delta t) = P_1(i\Delta t) - \frac{\left(P_2(i\Delta t)-P_1(i\Delta t)\right)^2}{P_3(i\Delta t)-2P_2(i\Delta t)+P_1(i\Delta t)} \tag{2.8}$$

Here, P_1, P_2, and P_3 are the pressure corresponding to 1st, 2nd, and 3rd iterations at time $i\Delta t$ at a particular point on the hull.

2.5 Summary

In this chapter, an in-house developed CFD-FEM coupling scheme is introduced. First, one-way coupling scheme between CFD and FEA is described with detailed discussion on CFD and FE models. The mapping of involved data between discrete CFD grids and defined FE panels is done using IDW method. The balance of the total force is checked at every time-step to avoid accumulation of the error over time. In case of the two-way coupling method, a predictor-corrector scheme is used between CFD and FEA to conduct the strong coupling.

3 Validation of the Coupled Model

In this chapter, the validation of the coupling method is shown by comparing with experimental results. First, heave and pitch Response Amplitude Operators (RAOs) and time series responses are compared with experimental results. Later, the time series of the vertical bending moment (VBM) including the springing effect are compared between the simulation and the experiment.

3.1 Experimental Details

The experiment was conducted using a backbone model. The length of the hull is 2.7 m, breadth 0.45 m, and depth 0.27 m. The hull structure is simple and symmetric about the X and Y axis (Figure 3.1). The principal characteristics of the model are listed in Table 3.1. The body plan of the hull is shown in figure 3.1. There were nine segments from bow to stern, rigidly connected to the backbone using bolts (Figure 3.2). The gaps between the segments were taped using waterproof elastic rubber to prevent the water to come inside while conducting the experiment. The material of the backbone is aluminum.

The backbone was modelled such that there is no unwanted generated force from other parts of the hull while moving. The height, width, and thickness of the backbone were 50 mm, 75 mm, and 5 mm (Figure 3.2). There were strain gauges attached to the backbone at the connection of each segment so that it can capture strains correctly due to elastic motion of the hull. The location and details of strain gauges can be seen in Figure 3.2 and 3.3. The motion of the hull is measured by attaching the gimbal to the mid-segment, which is depicted in Figure 3.2. The test model was a 1:100 scaled model of the original. The desired draft was achieved by putting external weight plates uniformly over the hull. The total weight of the model used is 1239.5 N.

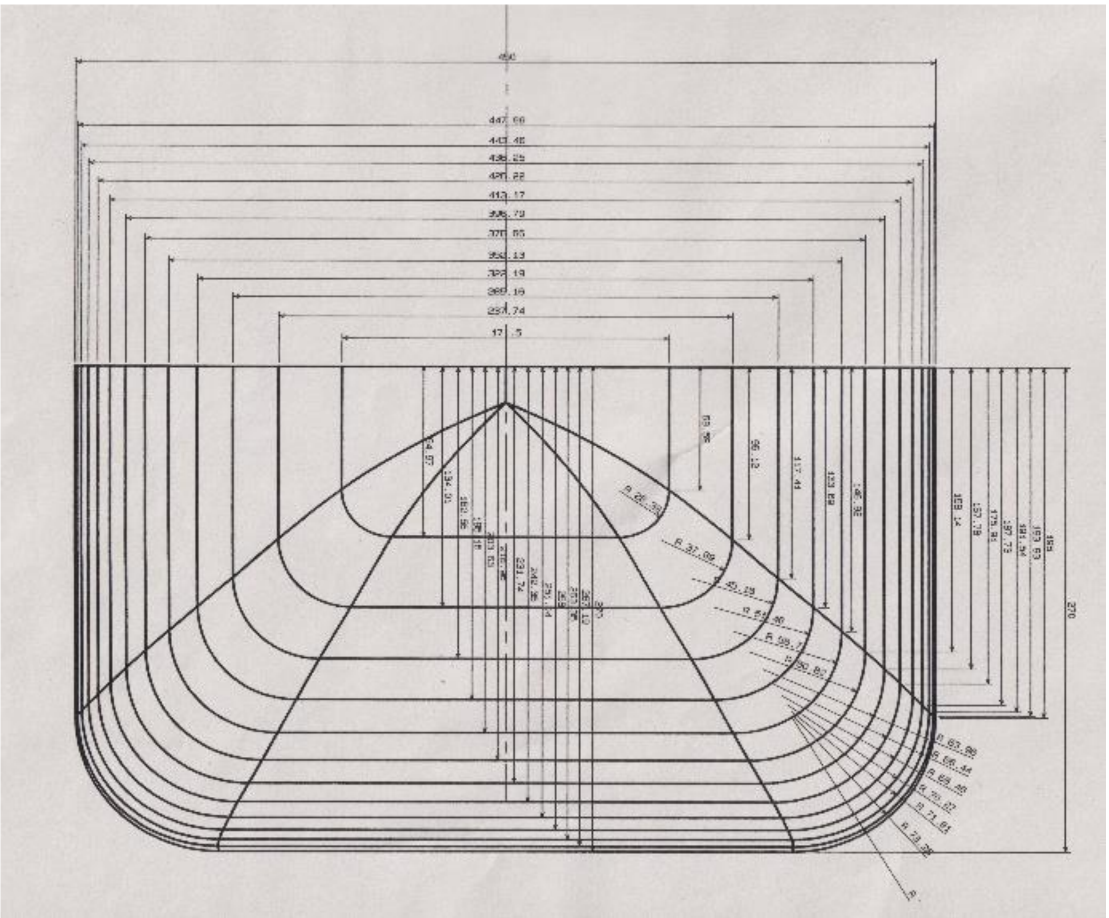

Figure 3.1 Body plan of the hull

Table 3.1 Details of the model used in the experiment and numerical analysis

Length (L)	2.7 m
Breadth (B)	0.45 m
Depth (D)	0.27 m
Draft (d)	0.12 m
Weight	1239.5 N
Center of Gravity (OG)	0.178 m
Radius of Gyration (Kyy)	0.676 m
Modulus of Elasticity of backbone(E)	60.8 GPa
Modulus of Elasticity of hull (E)	63.5 GPa

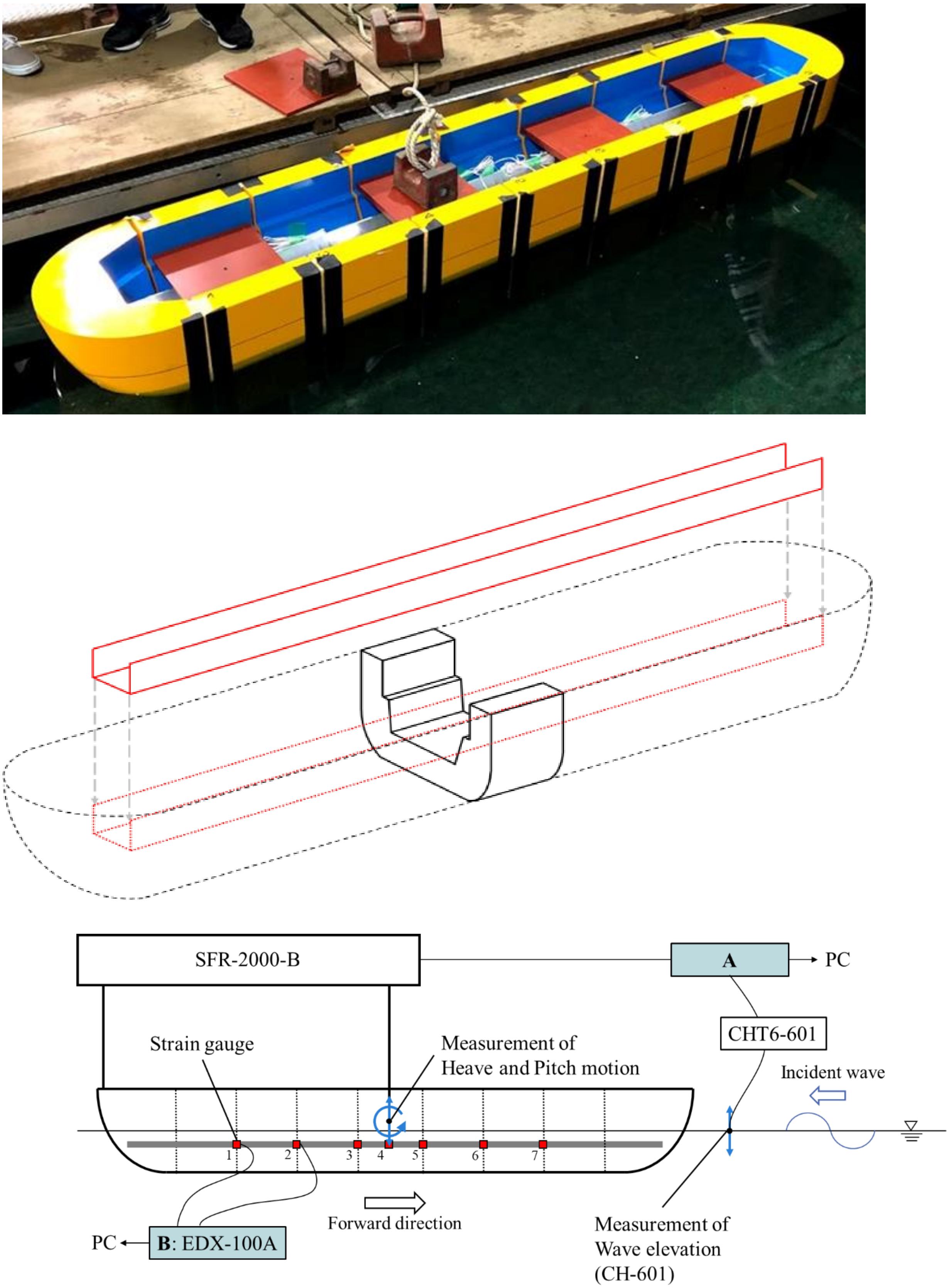

Figure 3.2 Backbone model with experimental setup, conducted at Osaka University

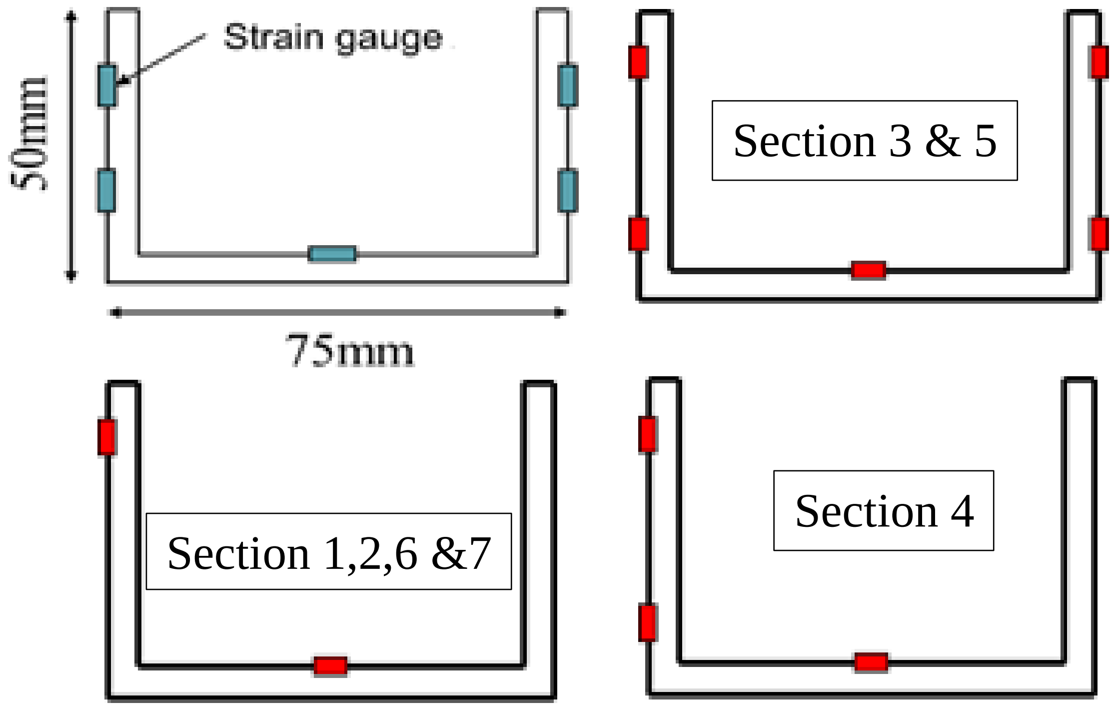

Figure 3.3 Location of strain gauges in backbone

The experimental tank is 100 m long, 7.8 m wide and 4.3 m in depth. The various wave conditions of the experimental tests are listed in table 3.2 In table 3.2 λ, L, A_w, F_n are wave length, hull length, wave amplitude and Froude number respectively. In this chapter mainly, regular head waves without forward speed are investigated. Wave dissipaters were used and a significant time was given to calm the tank water between tests.

Table 3.2 Experimental wave conditions used in this chapter

Test Conditions	λ/L	A_w (m)	F_n
I	0.6	0.025	0.0
II	0.8	0.025	0.0

III	1.0	0.025	0.0
IV	1.1	0.025	0.0
V	1.2	0.025	0.0
VI	1.5	0.025	0.0
VII	2.0	0.025	0.0
VIII	2.5	0.025	0.0

3.2 Numerical Modelling

The same CFD and FE model as shown in section 2.1 and 2.2, are used in this chapter to model the experimental backbone model (Figure 3.2). For the 1D beam and backbone model (Figure 2.4-2.5) a uniform distribution of the mass is used, whereas in case of the backbone-outer shell model the same mass distribution as of experimental model is used (Table 3.1).

3.3 Comparisons of Rigid Body Responses

First, the rigid-body motions of the hull are computed using CFD and then compared against experimental results. It can be seen from Figure 3.4 that CFD responses match within engineering accuracy with experimental results. In the case of heave in almost all the cases CFD matches exactly with the experimental result, however with little difference in 6.165 rad/s. That difference does not occur in the case of pitch RAO (Figure 3.4).

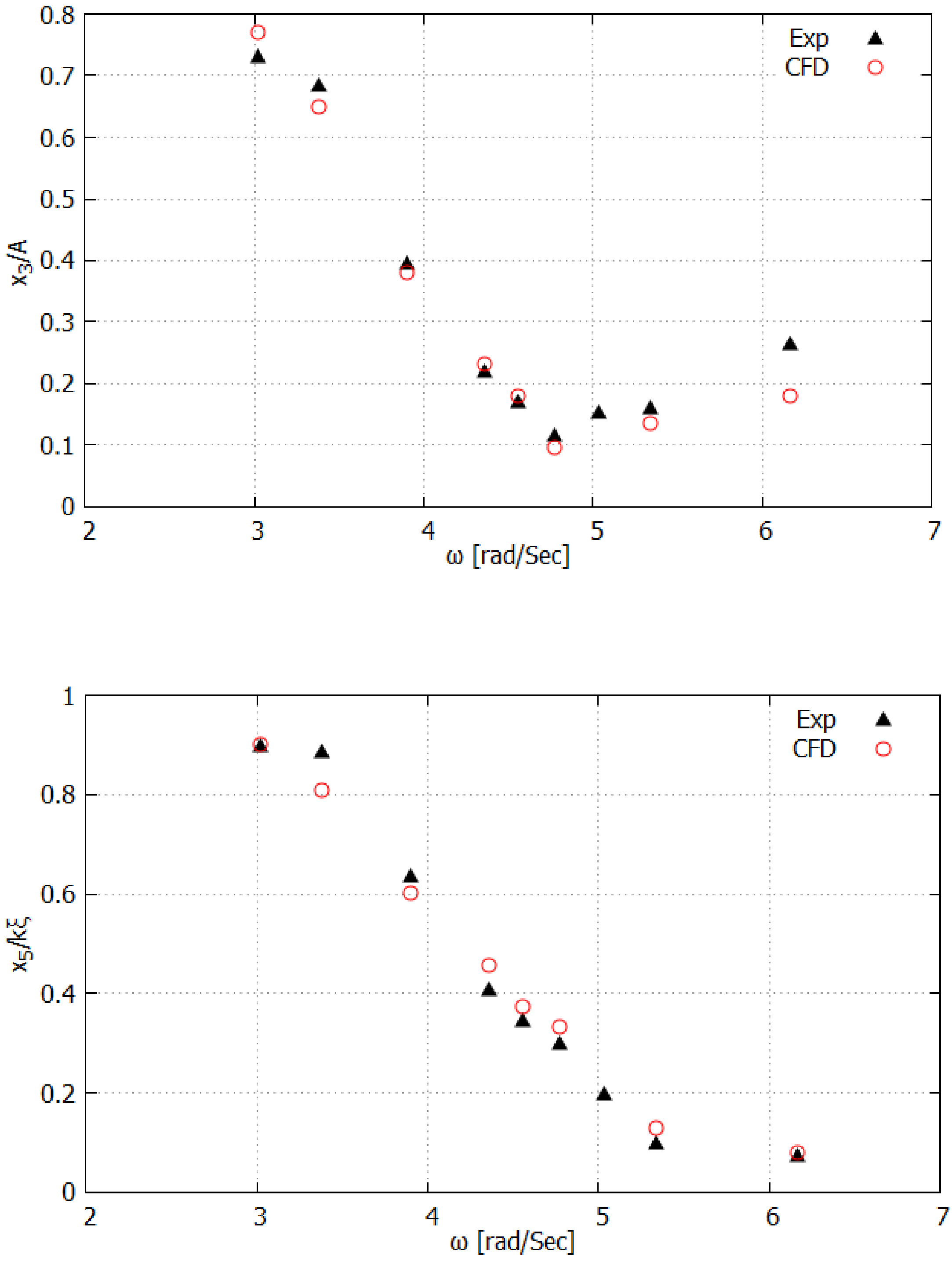

Figure 3.4 RAOs of heave, pitch compared with experiment for $F_n = 0.0$

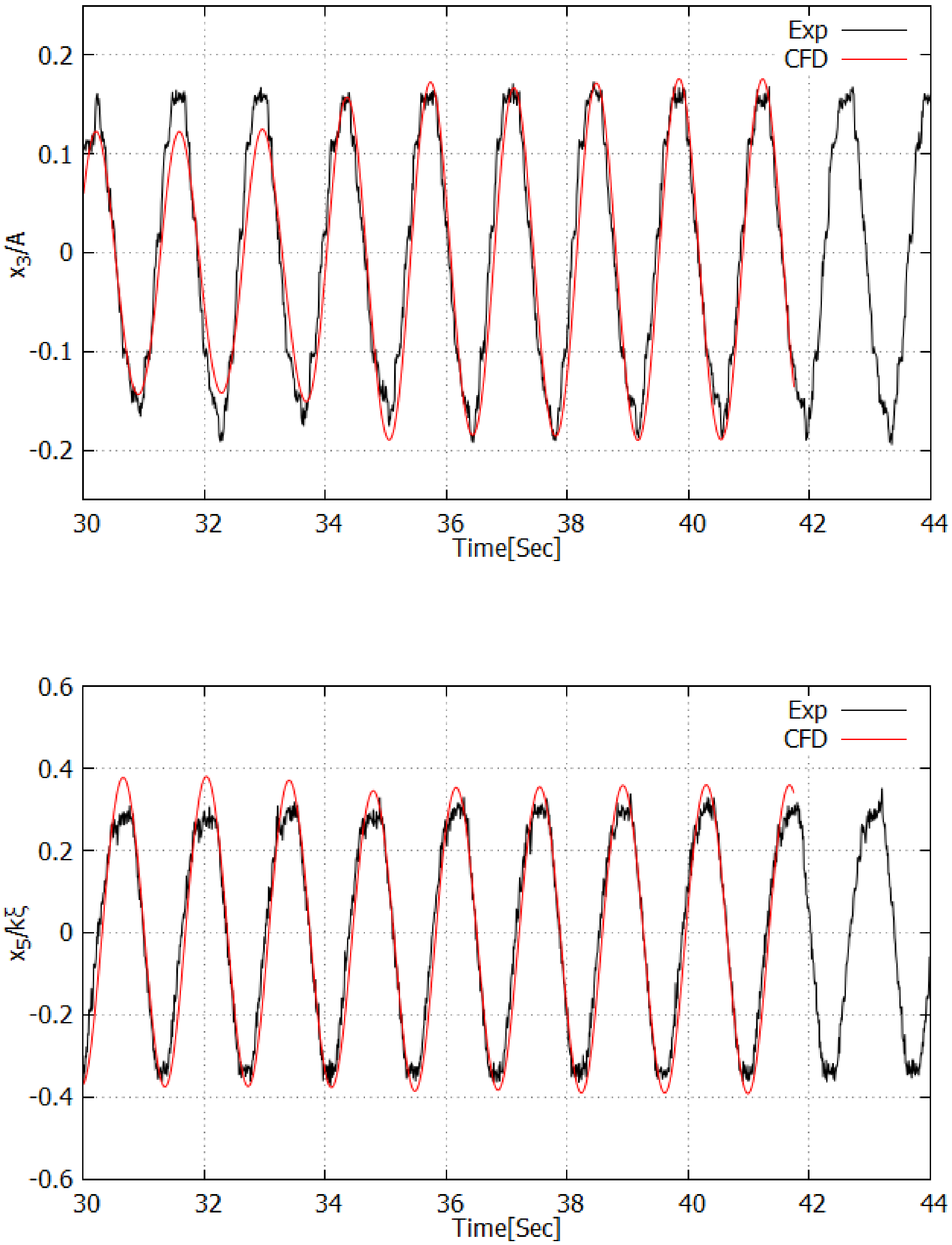

Figure 3.5 Heave, and pitch time series compared with experiment for test case IV.

To verify the robustness in the case of the time series reproduction from the experiment, in Figure 3.5 heave and pitch time series are compared with the experiment for λ/L = 1.1. It can be seen that both heave and pitch time series are converged in last four cycles and matched within the engineering accuracy.

3.4 Hammering Test and Added-mass Effect

First, a hammering test was performed using two-way coupling between CFD-FEA model. The objective was to confirm the wet natural frequency of the structure so that the vibrational responses can be imitated in the one-way coupling. The dry natural frequency of the structure is 9.2 Hz. After stabilizing the body in the calm water conditions, an impulse load was applied for 0.002s at the center of mass of the hull. Figure 3.6 and 3.7 shows the time series and frequency characteristics of VBM by the experiment and the two-way coupling simulation. From Figure 3.7 the wet natural frequency of the structure can be estimated around 6.8 Hz by both the experiment and the two-way coupling. Although the time series of VBM could match initial two cycles, differences occur slowly after that. From this observation it can be commented that, the damping of the current model still needed to be tuned further to match with experimental result. A possible reason due to variation in the impact load between experiment and numerical cases. Another possible cause of this issue is that the number of inner iterations is constantly set as 3, thus strict convergence of the pressure and deformation might not have attained. In performing two-way computations, it took 1 day/1s of the simulation by using 8 core CPU, and further increase of the number of inner iterations will require further computational time. Also, there is no significant difference in solution time if the number of cores is increased to 18. This is because 3 inner iterations are involved at each time step between LS-DYNA and STAR-CCM+, which cannot be parallelized.

An effective alternative to the two-way coupling is to use one-way coupling where the total mass of the body is artificially tuned by keeping the wet natural frequency same with two-way coupling and experiment. As the wet vibration of the hull is around 6.8 Hz, the same natural frequency can be achieved using equation (3.1) by tuning the mass of the model considered as added mass.

$$\omega = \sqrt{[K]/[M](1+\alpha)} \tag{3.1}$$

In equation (3.1), $[K]$ and $[M]$ are stiffness and mass matrix, and α is the factor to consider the added-mass effect. The wet natural frequency was achieved in one-way coupling by tuning the total mass of the body according to equation (3.1). The computational efficiency by the one-way coupling is apparent since it took 10mins/1s of the simulation with 8 core CPU.

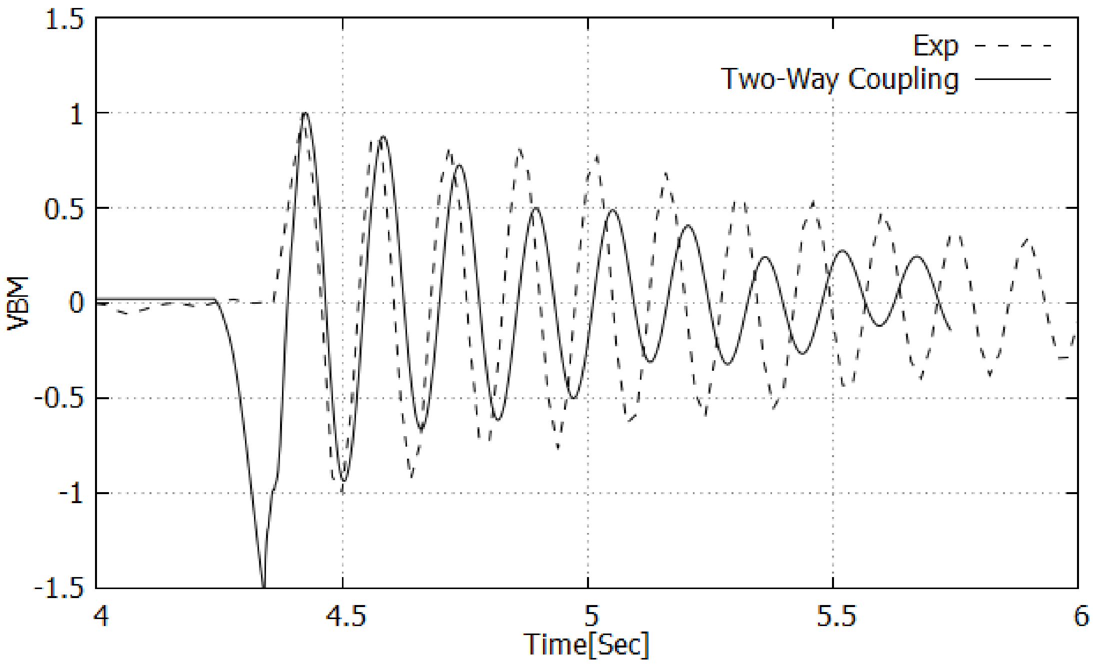

Figure 3.6 Normalized VBM time history due to an impulse at calm water condition

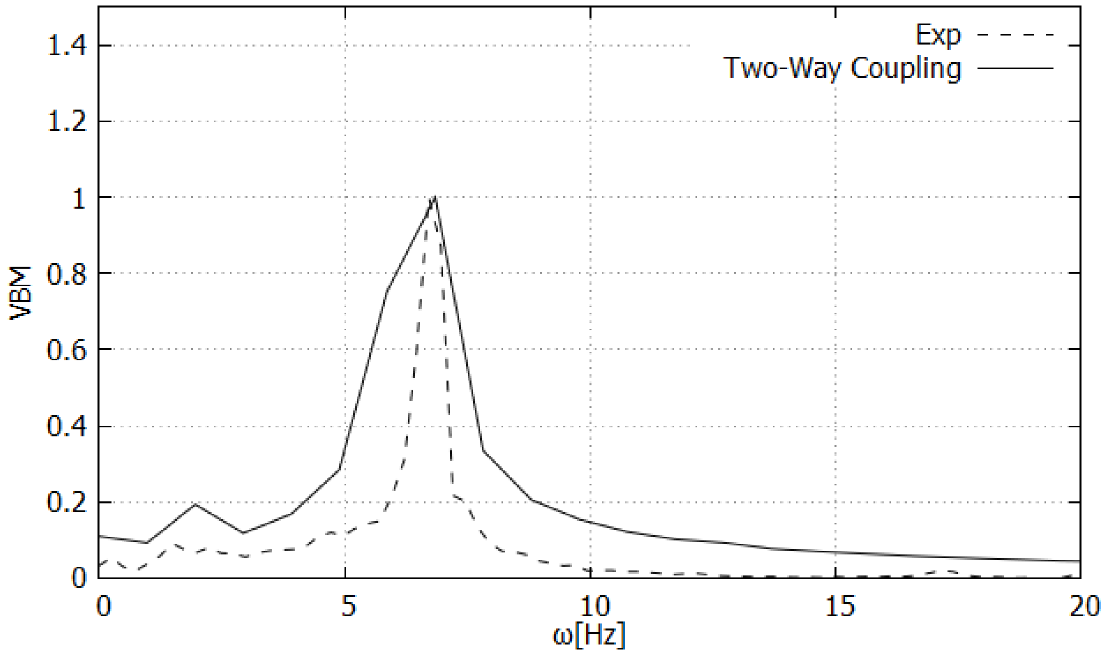

Figure 3.7 Normalized FFT of VBM time history due to an impulse at calm water condition

3.5 Comparison of Flexible Responses

In this section, the flexible vibrations seen in the all experimental cases (Table 3.2) are investigated and validated with mentioned numerical scheme in chapter 2. Figure 3.8, 3.10, and 3.12 shows time series of the VBM calculated using one-way coupling and validated against experimental time series for three different wave cases from Table 3.2. The corresponding FFT are shown in Figure 3.9, 3.11, and 3.13. After certain time window the experimental VBM responses have been compared with one-way coupling results, which is case dependent. Therefore, in Figure 3.8, 3.10, and 3.12 it can be seen different time windows are chosen for comparisons. For both cases, the VBM is calculated and measured at mid-ship section. It can be confirmed from Figure 3.10 that although the amplitude of the vibration is almost same, a little difference in excitation frequencies resulted in small phase difference between experimental and one-way coupling results (Table 3.3). For all the cases, the vibrational amplitude is different than that of the experiment (Table 3.3). In Table 3.3 a comparison of springing VBM amplitude between experiment and one-way coupling has shown for all the test cases. A little mismatch in the excitation frequency (i.e. wet natural frequency) can cause damping effect, hence, the springing amplitude might not have matched (Figure 3.8-3.13). A similar behavior can be noticed for almost all the test cases.

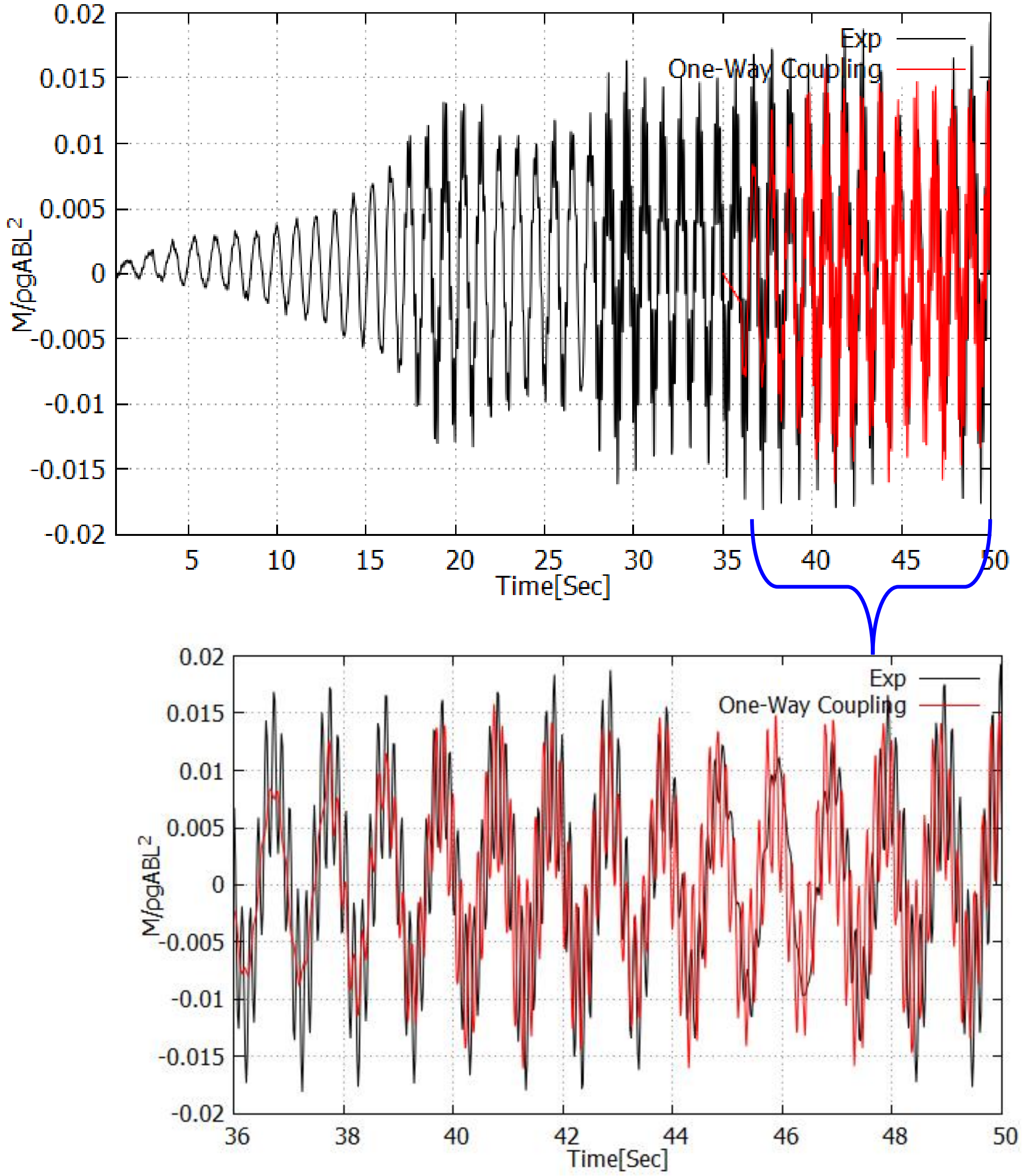

Figure 3.8 Flexible VBM time series computed by one-way coupling compared with experiment for test case I.

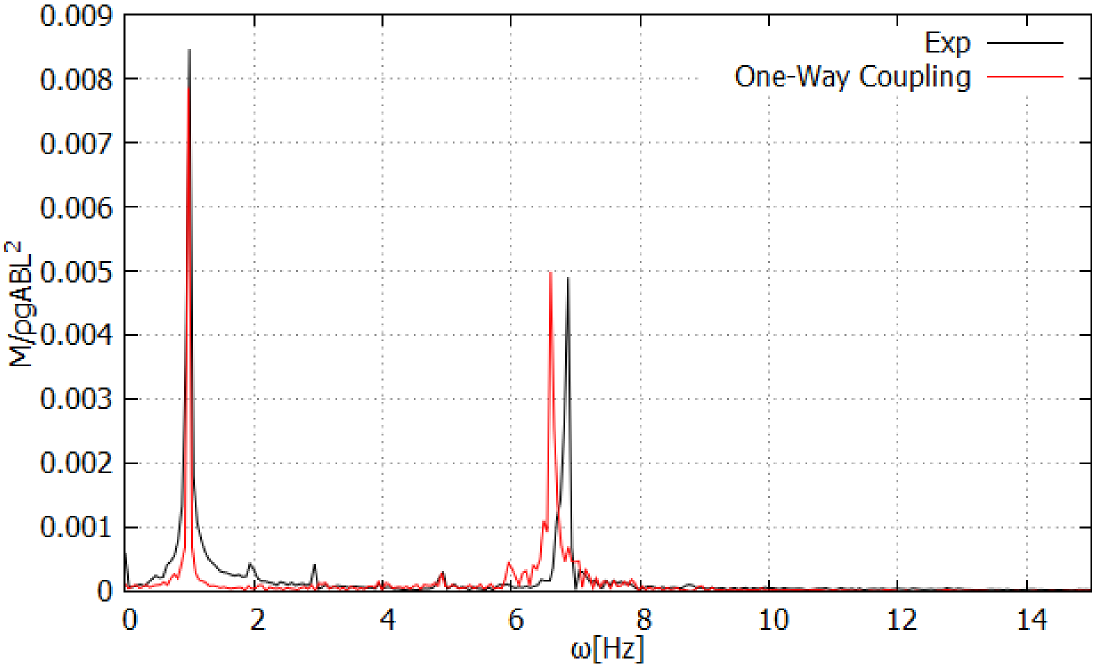

Figure 3.9 FFT analysis of flexible VBM time series computed by one-way coupling and experiment for the test case I.

The springing vibration initiates after a sufficient time elapsed in the experiment. In the Figure 3.8 for case I, for instance, the springing has started appearing fully after 30s as it might need to stabilize the hull to consider the added mass effect. In Figure 3.8, 3.10, and 3.12 a magnified time window has shown to have a better understanding of the comparison with one-way coupling result. First, the CFD calculations are performed to achieve steady solution, then the one-way coupling has performed. It can be seen although the added mass artificially tuned it takes 2-3s to fully excite the system. The slight phase differences of the springing vibration in the time series between the experiment and the one-way coupling may be caused by the difference of the initiation time of the springing. All in all, from the viewpoint to investigate the springing phenomenon with less computational expenses, one-way coupling results show quite good agreement with experiment.

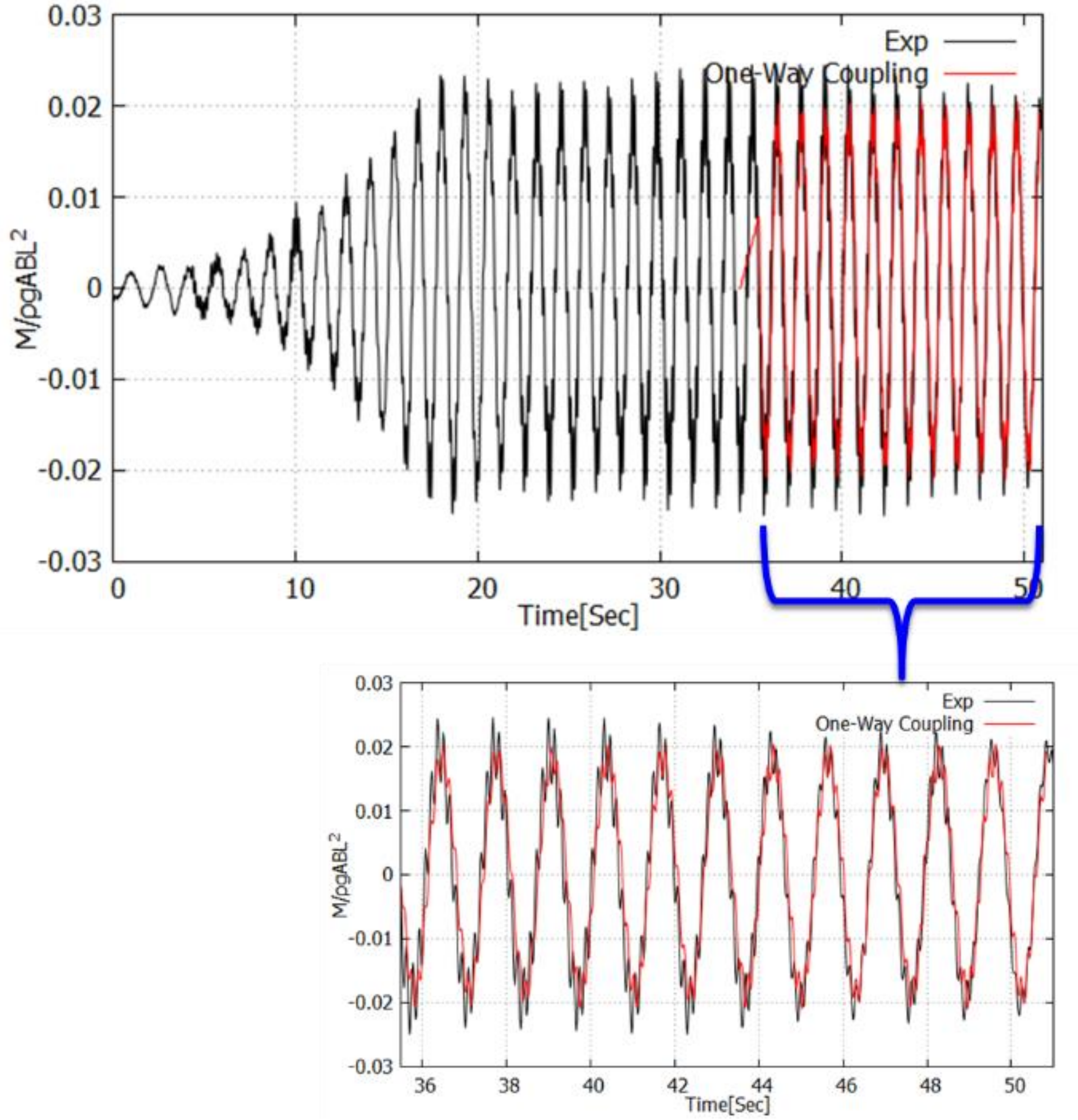

Figure 3.10 Flexible VBM time series computed by one-way coupling compared with experiment for test case III.

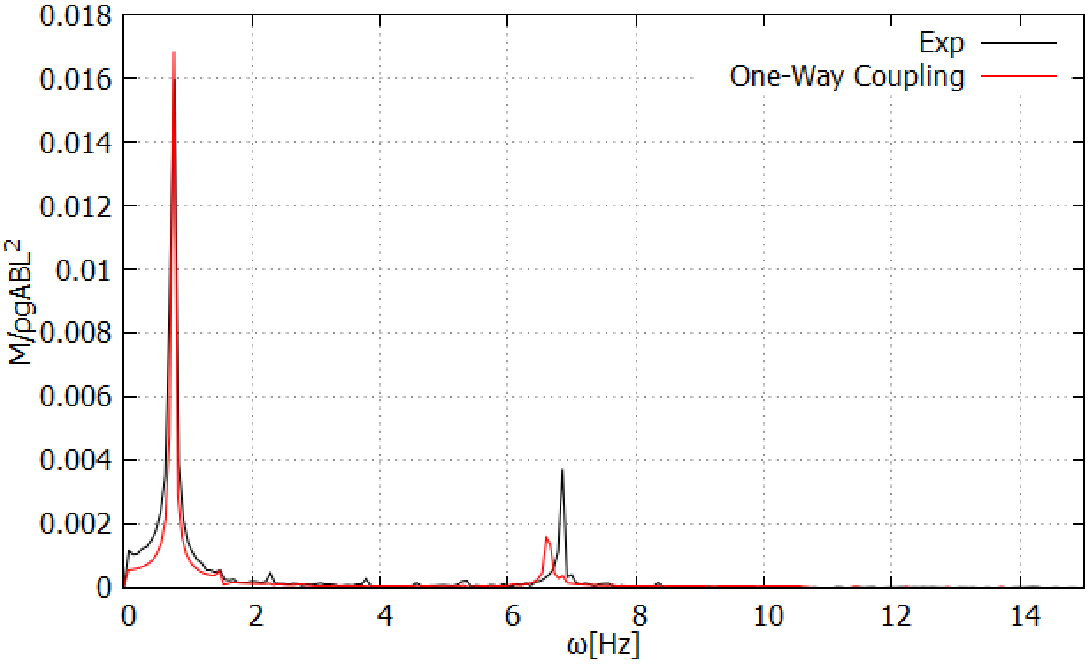

Figure 3.11 FFT analysis of flexible VBM time series computed by one-way coupling and experiment for the test case III.

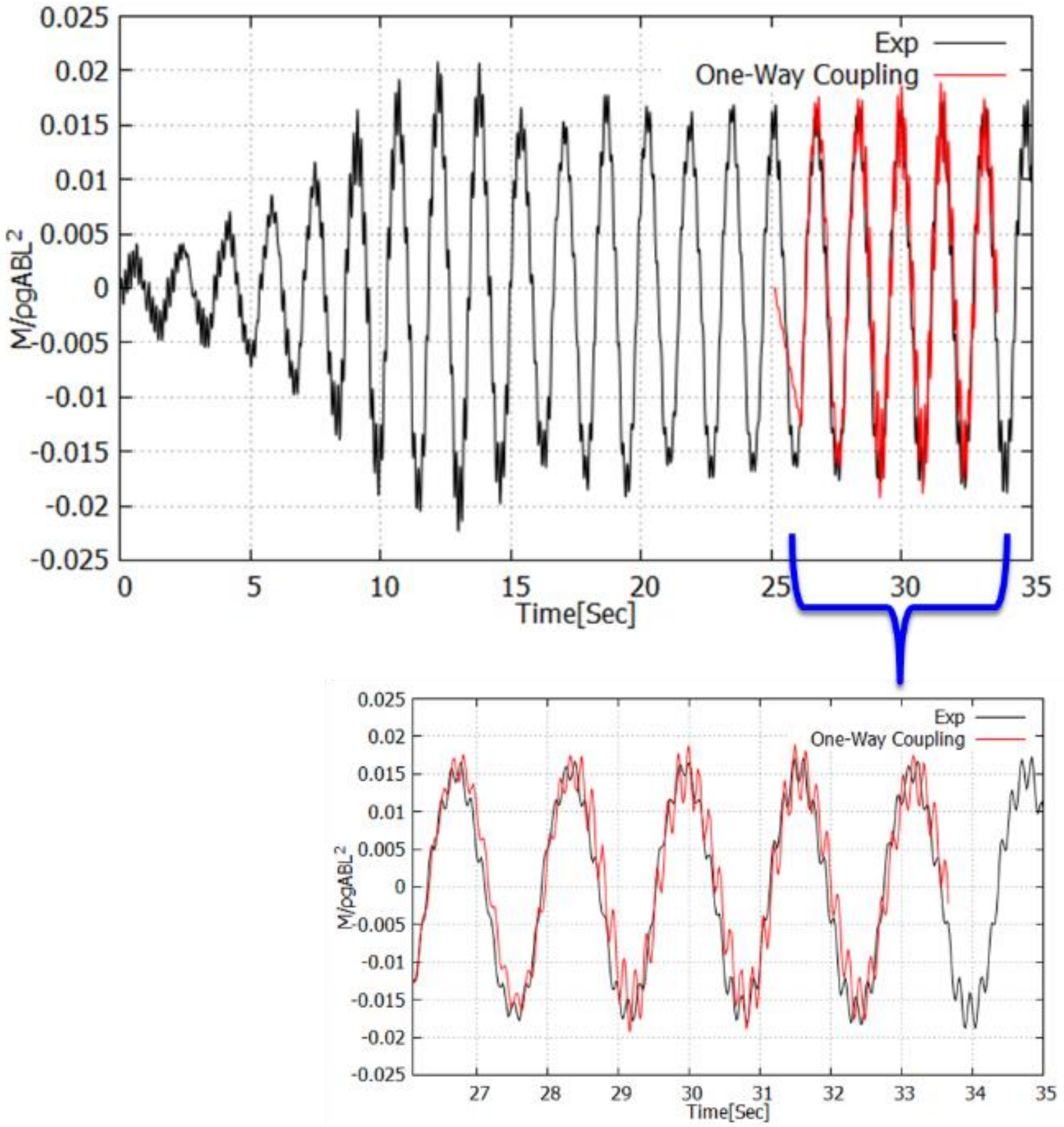

Figure 3.12 Flexible VBM time series computed by one-way coupling compared with experiment for test case VI.

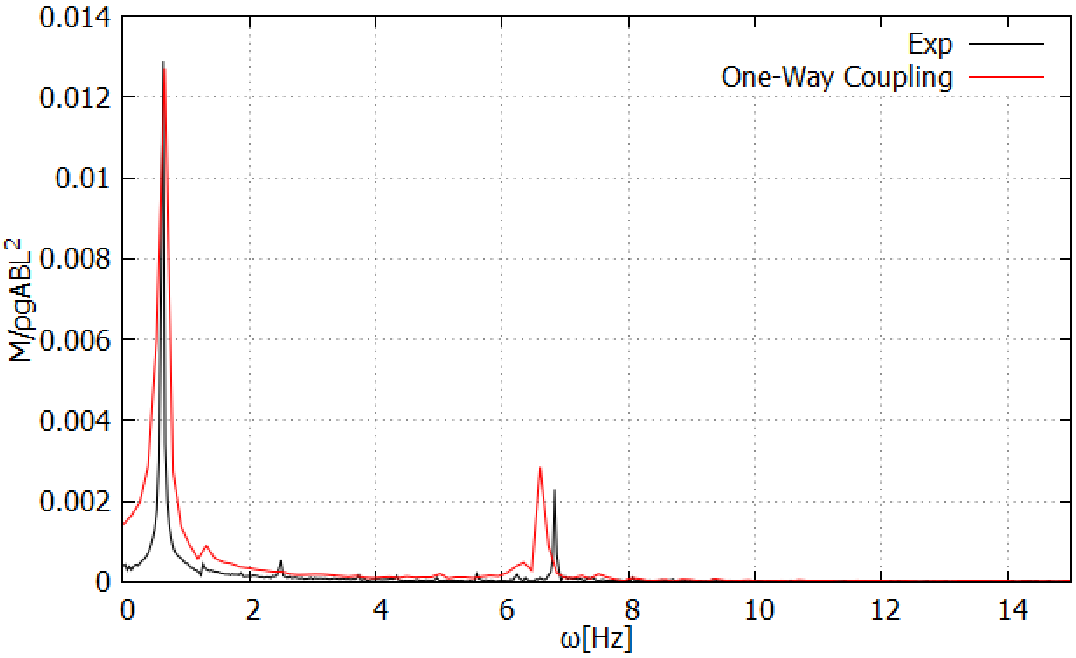

Figure 3.13 FFT analysis of flexible VBM time series computed by one-way coupling and experiment for the test case VI.

3.6 Comparison of Models

In this section, the backbone-outer shell model (Figure 2.6) is compared with a simple backbone shell model (Figure 2.5). In case of the backbone shell model, the total mass is distributed uniformly and the modulus of elasticity is kept constant with the experiment (Table 3.1). In case of the backbone model the CFD pressure is converted to sectional loads by integrating pressures over the hull surface and applied at each section. This approach is different from the backbone- outer shell model (Figure 2.6) as the direct pressure is applied in the hull surface in LS-DYNA.

In Figure 3.14 the VBM for the wave case I ($\lambda/L = 0.6$) is compared. It can be seen that although the springing frequency is matching, the amplitude is quite less for high frequency part. This can be due to a little mismatch between excitation frequency and natural frequency of the structure.

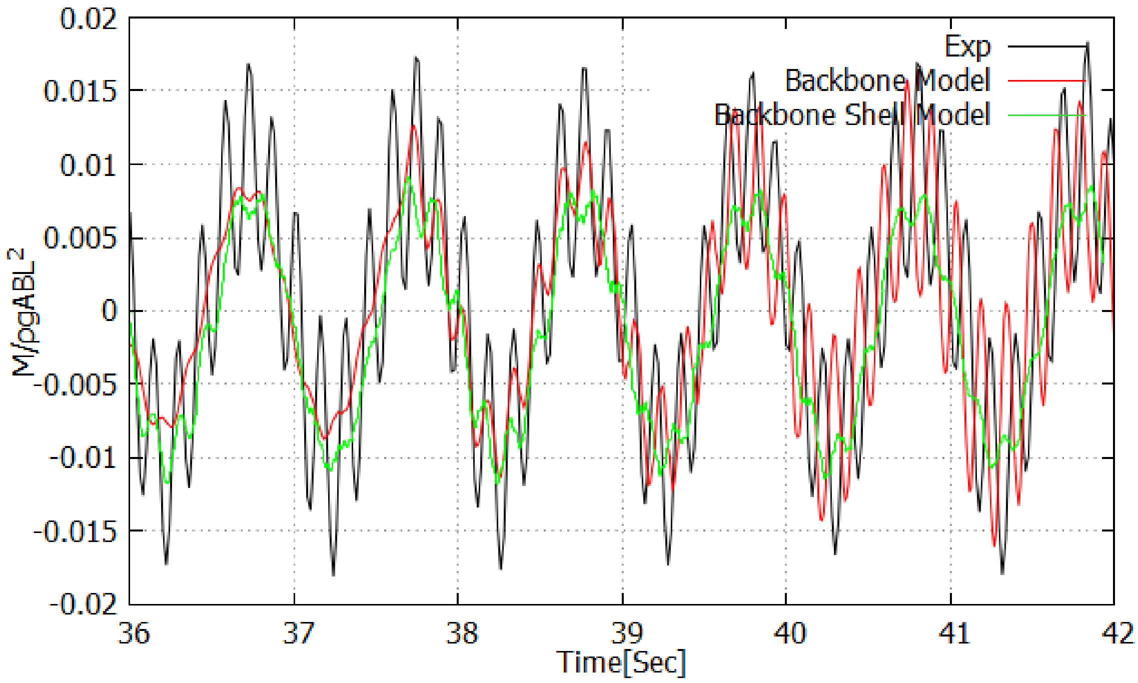

Figure 3.14 Backbone model without outer shell for the wave case I

3.7 High Frequency Vibrations

To investigate whether this is a springing or not, harmonic orders (N) are calculated for every wave case in Table 3.2 using equation (3.2). In equation (3.2), ω_e, and ω_n are encounter frequency, and excitation frequency respectively. It can be seen that N is an almost perfect integer in all of these cases, and corresponding to 7th to 14th order harmonics.

$$\omega_n = N\omega_e \tag{3.2}$$

Table 3.3 Comparisons between experimental and numerical high frequency vibrations

Test Conditions	Frequency (Hz)		Springing VBM Amp ($M/\rho gABL^2$)	
	Exp.	Num.	Exp.	Num.
I	6.89	6.56	0.005	0.005
II	6.79	6.68	0.002	0.004
III	6.86	6.59	0.0037	0.0016
IV	6.50	6.69	0.0012	0.0054
V	6.89	6.53	0.00035	0.0016
VI	6.79	6.59	0.0023	0.0028
VII	6.99	6.69	0.0015	0.0026
VIII	6.79	6.68	0.00155	0.0003

Table 3.4 Computation of the higher order harmonics

Test Conditions	Encounter Frequency	Experimental Frequency (Hz)	Harmonic Order (N)
I	0.98	6.89	7
II	0.85	6.79	8
III	0.76	6.86	9.02
IV	0.72	6.50	8.96
V	0.69	6.89	10
VI	0.62	6.79	11
VII	0.54	6.99	13

VIII	0.48	6.79	14

It is observed from the experiment and the one-way coupling that the springing vibration behave as the regular sinusoidal wave after its initiation in all the cases. Thus, the reduced-order modeling of the springing for the sake of extreme value prediction would be easily accomplished by adding regular sinusoidal wave terms to the VBM on top of the whipping component. If a Low Pass Filter (LPF) is applied (with cut-off frequency 2Hz) to all the sectional loads, the VBM time series should not contain any vibrations. Hence, can be proved that all the presented results in this chapter is noise free. In Figure 3.25-3.27, the VBM time series are calculated for the sectional loads with LPF and compared with experiment for test cases I, III, and VI.

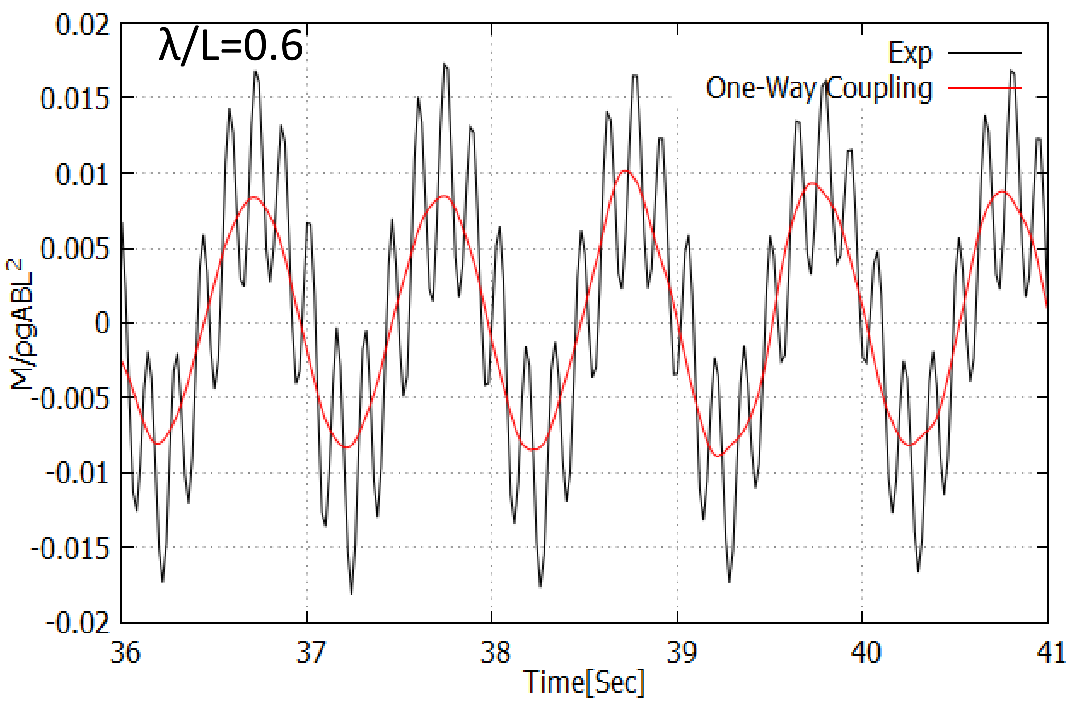

Figure 3.15 One-way coupling with LPF for the test case I.

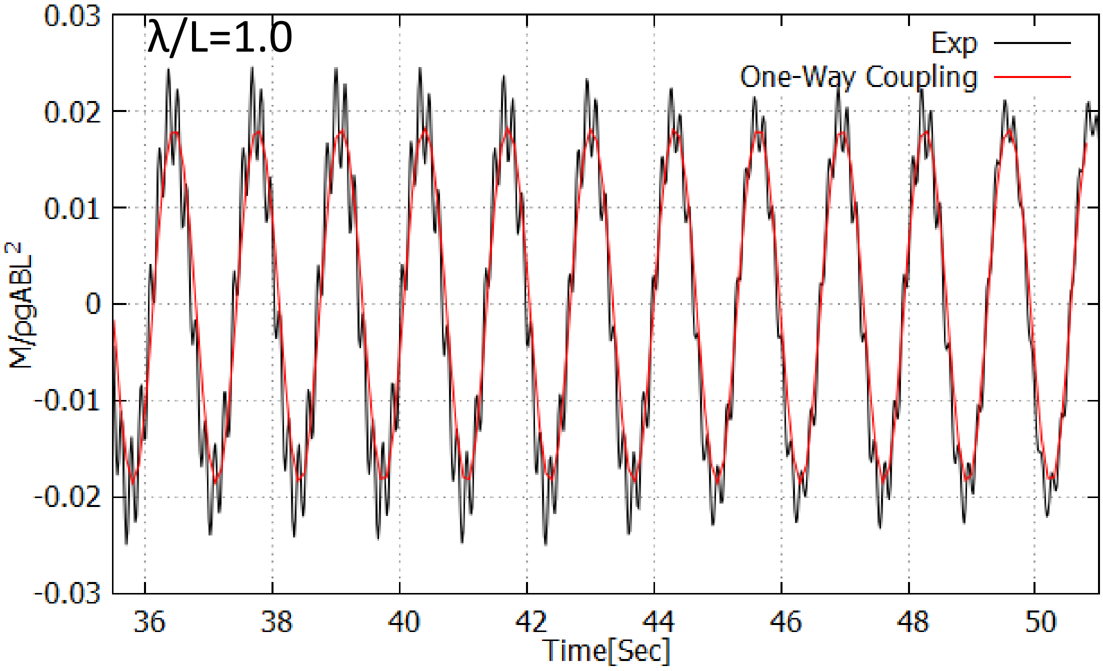

Figure 3.16 One-way coupling with LPF for the test case III.

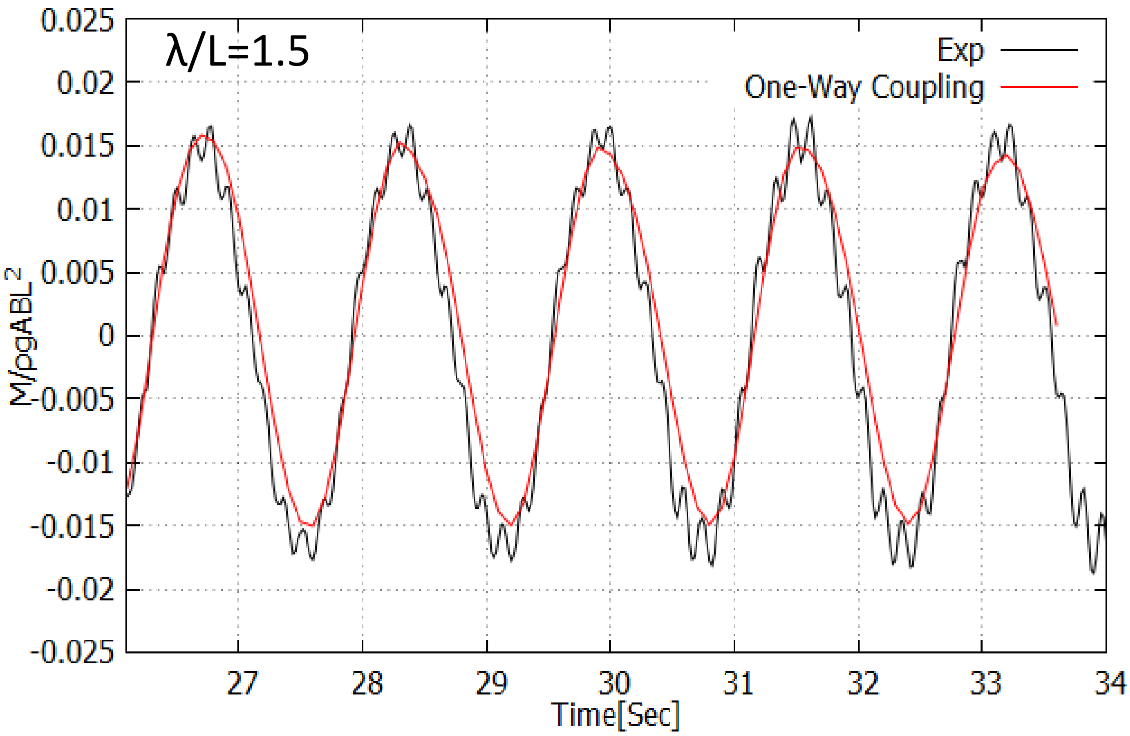

Figure 3.17 One-way coupling with LPF for the test case VI.

3.8 Summary

In this chapter, the investigation of the higher order springing phenomenon is done for a barge type backbone model. First, the rigid body motions are calculated and validated with the experiment. The two-way coupling is performed for calm water case with sudden hammering at the center of mass and the wet natural frequency calculated which is comparable to the experiment. In order to keep the same wet natural frequency as the experiment, the mass of the body is adjusted in performing the computationally efficient one-way coupling. By using the one-way coupling, the springing phenomena is observed after sufficiently long simulation time elapsed. The VBM time series by the present one-way coupling method are well validated with the experimental results keeping the focus of the study to investigate the higher order springing phenomenon. The harmonic orders are calculated, which confirmed in the current model harmonics up to 14^{th} order existed.

4 Maximum Probable Wave Episode and Reduced Order Model

In this chapter, the formulation of a Reduced Order Model (ROM) to calculate VBM of a ship is discussed. There are three VBM components, namely wave-induced, whipping-induced, and springing-induced. The idea is to develop a lower order model, which can replicate the extensive CFD-FEA coupled analysis. Such a tool can be useful in digital twin of the structure, or calculating extreme value analysis. The developed ROM is used with First Order Reliability Method (FORM) to design a Maximum Probable Wave Episode (MPWE), which is considered as an input wave field for the validation in the next chapter. Compared to the previous researches by Pal et al. [16], and Takami et al. [18] current reduced order model contains a springing component along with the wave-induced and whipping components. In the following section, the formulation of the ROM is discussed step by step.

4.1 Wave-induced Component in ROM

The wave-induced (WI) component of the VBM is calculated using equation (4.1) for the calculated wave episode using equation (4.2). In equation (4.1), $R(\omega_i)$ and $T(\omega_i)$ are amplitude and phase transfer functions. These can be evaluated either from the coupled CFD-FEM analysis or other conventional methods. In this study, a non-linear strip theory code is used. Here, in equations (4.1-4.2) u_i and $\bar{u}_i$ are independent and Gaussian distributed random variables, $S(\omega_i)$ is the wave spectrum which is ISSC here, ω_i is the discrete frequencies, and the number of discrete wave components, N is chosen 100 here. To avoid repetition of waves in equation (4.2) $d\omega$ is set non-equidistant.

$$M_{wave,strip}(t) = \left\{1 + \sum_{k=0}^{k=6} a_k \eta_p^k\right\} \sum_{i=1}^{N} R(\omega_i) \begin{bmatrix} u_i\sqrt{S(\omega_i)d\omega_i}\cos\big(\omega_i t + T(\omega_i)\big) \\ +\bar{u}_i\sqrt{S(\omega_i)d\omega_i}\sin\big(\omega_i t + T(\omega_i)\big) \end{bmatrix} \quad (4.1)$$

$$\eta(t) = \sum_{i=1}^{N} \left(u_i\sqrt{S(\omega_i)d\omega_i}\ \cos(\omega_i t) + \ \bar{u}_i\sqrt{S(\omega_i)d\omega_i}\ \sin(\omega_i t)\right) \quad (4.2)$$

In order to account for the nonlinearity in the reduced order model, the peak wave amplitude η_p is considered as a k^{th} degree polynomial in the form of $\sum_{k=0}^{k=6} a_k \eta_p^k$, where, a_k is the factor for accounting for nonlinear VBM in hogging. Further, a correction factor is introduced by multiplying $M_{wave,strip}$ with c_{cfd} to match with CFD-FEM coupling.

4.2 Whipping-induced Component in ROM

Further, in order to introduce the effect of bow slamming, von Karman's momentum theory is used in equation (4.3) assuming the 3D bow flare sections as a combination of various 2D sections of unit length. The impulse is calculated as the multiplication of relative velocity between the bow flare and wave surface and the change of added mass over the section. The relative velocity ($\dot{\eta}_{rel}$) between the wave surface and bow flare is calculated by converting the heave and pitch at CG of the hull to the individual 2D section's location (Figure 4.1). The amount of water mass around the bow section with deadrise angle δ is calculated using equation (4.4), where, ρ is the fluid density, $(\eta_{rel} - d)$ is the distance between the wedge corner and water surface (Figure 4.2).

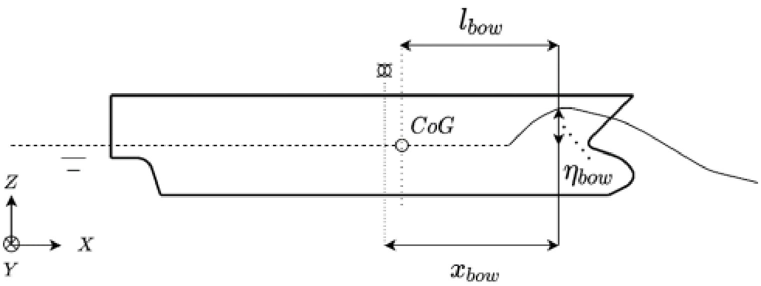

Figure 4.1 Schematic representation of the definition of relative distance between bow and wave surface

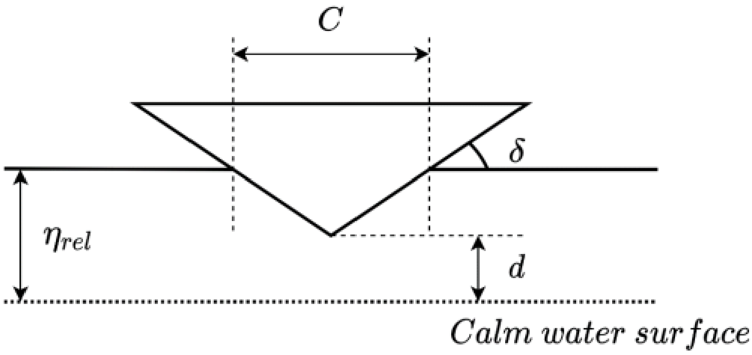

Figure 4.2 Illustration of parameters used for calculating slamming impact force

$$F_{imp}(t) = \dot{M}_a(t)\dot{\eta}_{rel}(t) \tag{4.3}$$

where, $M_a(t) = \frac{\pi\rho(\eta_{rel}-d)^2\cot^2\delta}{2}$ (4.4)

$$\eta_{bow}(t) = \sum_{i=1}^{N}\left(u_i\sqrt{S(\omega_i)d\omega}\cos(\omega_i t + k_i x_{bow}) + \bar{u}_i\sqrt{S(\omega_i)d\omega}\sin(\omega_i t + k_i x_{bow})\right)$$

(4.5)

To calculate the whipping VBM and its contribution over time, the use of convolution integral in equation (4.6) is made. In equation (4.6), I is the impulse response function, c_{imp} and τ_{imp} is the correction factors for amplitude and phase. Due to main contribution of the whipping going to 2-node vertical bending, the impulse response function is calculated based on an oscillatory single degree of freedom structure in equation (4.7). In equation (4.7), ζ and ω_0 are the damping ratio and natural angular frequency of the 2-node vibration. Initial conditions of I and $\dot{I}$ are taken as 0 and -1 respectively.

$$M_{whip}(t) = \int_0^\infty I(t-\tau)\, c_{imp} F_{imp}\left(\tau - \tau_{imp}\right) d\tau \tag{4.6}$$

$$I(t) \approx exp(-\zeta\omega_0 t)\left(I(0)\cos(\omega_d t) + \frac{\zeta\omega_0 I(0) + \dot{I}(0)}{\omega_d}\sin(\omega_d t)\right) \tag{4.7}$$

where, $\omega_d = \omega_0\sqrt{1-\zeta^2}$

4.3 Springing-induced Component in ROM

In the case of modeling a ROM, which can capture the springing phenomenon, the amplitude, and frequency of the vibration has to be known in advance. As discussed in Chapter 3, the springing phenomenon usually follows the relationship in equation (4.8), where vibrational frequency, ω_{ni}, can be found by multiplying the wave encounter frequency (ω_e) with an integer (N) (Oberhagemann, [33]). The amplitude of vibration (A_{spr}) is difficult to model theoretically, however it can be modeled statistically from the experimental data (see the Chapter 5). So, the VBM component of the springing can be written as in equation (4.9).

$$\omega_{ni} = N\omega_e \tag{4.8}$$

$$M_{spr}(t) = A_{spr}\{\cos(\omega_{ni}t + \varepsilon_{ni})\} \tag{4.9}$$

However, before calculating the probability of exceedance of VBM the proposed method should be validated. In this study, an in-house CFD-FEM one-way coupling scheme and as well as experimental analysis is used to validate the proposed ROM.

4.4 Generation of MPWE

The Maximum Probable Wave Episode (MPWE) is created using First Order Reliability Method (FORM), with the help of ROM to create the limit state function (LSF). Since this method is not primary focus of the current study it is explained briefly. The implementation of the FORM for numerical analysis is described through some series of points below:

I. First, normally distributed random variables (u_i, $\bar{u}_i$) are generated and used in equation 4.2 to generate wave profile η.

II. Then, for the target extreme VBM M_R, the limit state function g is calculated through equation 4.10. Where, $r_t(.)$ is the VBM calculated using the ROM which is precise around the design point (u_i^*, u_j^*).

$$g(.) = g(t_0|u_1, u_2, \dots, u_N, \bar{u}_1, \bar{u}_2\ , \dots, \bar{u}_N)$$
$$= 1 - \frac{r_t(t_0|u_1, u_2, \dots, u_N, \bar{u}_1, \bar{u}_2\ , \dots, \bar{u}_N)}{M_R}$$
(4.10)

III. Thereafter, the reliability index β is calculated through equation (4.11) and updated the design point.

$$\beta^2 = min\left(\sum_{i=1}^{N} u_i^2 + \sum_{i=1}^{N} \bar{u}_i^2\right) \quad subject\ to\ g(.) = 0 \qquad (4.11)$$

These steps are iterated until the convergence is achieved. Once the convergence is achieved, the extreme VBM, M_e is calculated through the time domain analysis and final design point is confirmed through the convergence of $\left|1 - {M_e}/{M_R}\right| \leq \varepsilon$. A schematic representation of the failure surface, g and design point corresponds to MPWE is shown in Fig. 3.

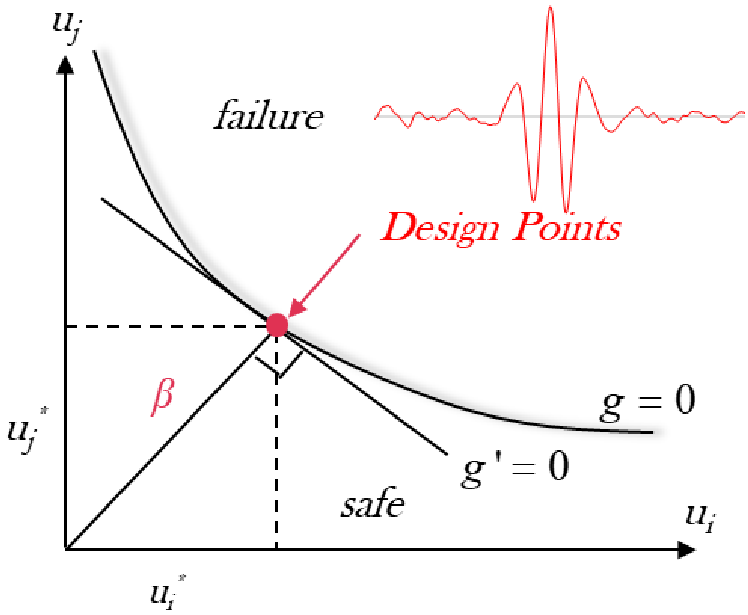

Figure 4.3 Schematic representation of the failure surface and design point detection by FORM.

Once the reliability index β is calculated by equation 4.11, the PoE of M_R peaks may be given analytically as in equation (4.12) on condition that peaks of M_R and its time derivative are uncorrelated (Jensen and Capul, [34]).

$$F(M_R) = exp\left(-\frac{\beta^2}{2}\right) \tag{4.12}$$

4.5 Prediction Extreme Value by Monte Carlo Methods

The failure probability may also be given by equation (4.13)

$$p_f = \int \dots \int_{g<0} f(u_1, u_2, \dots, u_N, \bar{u}_1, \bar{u}_2, \dots, \bar{u}_N) d\boldsymbol{u}\, \boldsymbol{d\bar{u}}$$

(4.13)

where $f(.)$ denotes the joint probability function of the variables u_i and $\bar{u}_i$ which are uncorrelated and follow standard normal distributions. By introducing a step function $I(.)$ which returns one for $g < 0$ and zero for $g \geq 0$, equation (4.13) may also be expressed to an integration in the whole domain D,

$$p_f = \int \dots \int_D I(.) f(.) d\boldsymbol{u}\, \boldsymbol{d\bar{u}}$$

(4.14)

The integration in equation (4.14) may be evaluated by using random variable ensembles generated from the joint probability function by using MCs. Over the past few decades the MC methods have been proved as one of the relying methods, as in MCs, the law of large number provides, with the N considering the number of random variable increases, the confidence increases in the estimate.

The advantages of MCs are, it is simple and easy to implement, and exploration does not get stuck on local optima so quickly as with dependent sampling. However, crude MC method is really time consuming since it also samples the non-importance regions. When the importance region is focused, equation (4.14) may be replaced by,

$$p_f = \int \dots \int_D \ I(.)\frac{f(.)}{h(.)}h(.)d\boldsymbol{u}\ \boldsymbol{d\bar{u}}$$

(4.15)

where, $h(.)$ is a function of variables u_i and $\bar{u}_i$ that has a high joint probability in the importance region.

$$p_f = \int \dots \int_D \ w(.)h(.)d\boldsymbol{u}\ \boldsymbol{d\bar{u}}$$

(4.16)

where, $w(.) = I(.)\frac{f(.)}{h(.)}$ and it is regarded as a weighting function. One has only to sample around the importance region as per the function $h(.)$ and sum up with the weighting function.

In the present study, we already know the importance region is a region around the design point. For using the importance sampling technique, the random variables whose mean coincides with the design point and with the variance 1.0 are sampled.

4.6 Summary

In this chapter, a reduced order model (ROM) is developed based on the CFD-FEA analysis. Wave-induced component of the VBM is calculated using transfer functions form non-linear strip theory. To introduce the effect of slamming on the hull girder vibrations (i.e., whipping) von Karman's momentum theory is used to calculate the impulse force. Later it is used with analytical formulation of impulse on a single degree of freedom mass-spring damper system to calculate the whipping vibrations. Formulation of the springing ROM is introduced based on the previous experimental observations. The derivation of the MPWE is also discussed here in this chapter, which will be used later for creating design wave. Lastly, a brief discussion on the prediction of the extreme value distributions by Monte Carlo methods is included.

5 Effect of Wave Induced Vibrations on Loads

In this chapter, the proposed ROM is first validated using CFD-FEM coupling results for an MPWE case. As the ROM parameters are updated from the previous study for better match between CFD-FEM analysis, comparisons are made between the old and new ROM. The proposed ROM also used for an arbitrary irregular wave for the same wave state to check to robustness of the method. Later, the ROM is used for an extreme value distribution of the midship VBM of a flexible ship and compared with experimental result. The effect of the inclusion of springing ROM in extreme value distribution is also discussed herein.

5.1 Subject Model

The experimental model is a model scale of the 6600TEU containership. The principal particulars of the model are shown in Table 5.1. The experimental test was conducted at National Maritime Research Institute (NMRI - Tokyo, Japan) in a 150m length towing facility. The experimental model is shown in Figure 5.1. The details of the experiment can be found in Takami et al. [18]. The 2-node wet natural frequency of the model is 5.47 Hz.

Table 5.1 Principal particulars of the model used in the experiment and numerical analysis

Properties	Full Scale	Model Scale

L_{pp}	283.3 m	2.838 m
B	42.8 m	0.428 m
D	24.0 m	0.240 m
Draft (Full Loading)	14.0 m	0.14 m
Displacement	109480 tons	122.16 kg
Scale	-	1/100
2-mode wet natural frequency	-	5.47 Hz

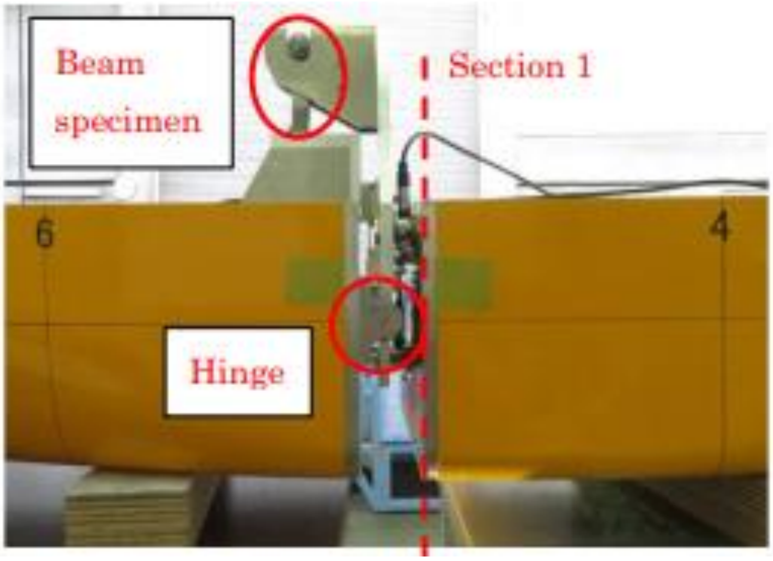

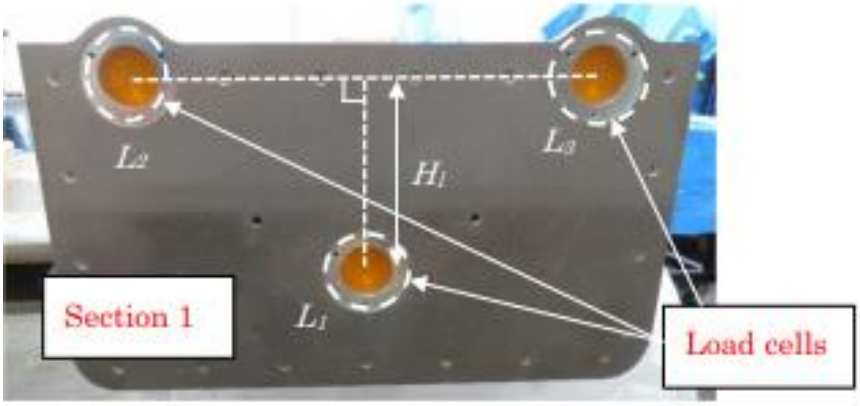

Figure 5.1 Scaled model of the containership used in Tank Test [18]

First regular wave cases for $\lambda/L = 1.3 - 0.4$ with or without forward speed are investigated. Then a short-term sea state is conducted, which is shown in Table 5.2. The speed of the vessel is kept the same between regular and irregular wave cases.

Table 5.2 Short-term sea states for towing tank test of the experimental model

H_s	T_z	F_n	Measurement Period (Full Scale)	Target VBM
11.5 m	15.0 s	0.078	46.7 hours	(Wave-Induced + Whipping Induced)

After recording the VBM time series from a short-term sea state, the extreme value distribution is calculated using the zero-up-crossing method. An example of counting peaks based on the zero-up-crossing method is demonstrated in Figure 5.2. In the case of an irregular wave, such as in Table 5.2, the wave frequency component is generally superimposed with lower and higher order elastic vibrations. In this figure, the wave component is calculated using a low-pass filter (LPF) with a cutoff frequency set as 3.0 Hz in the scaled model. The cutoff frequency has been chosen in such a way that it is sufficiently below the natural frequency of the structure and can omit the higher frequency part from the time series. To verify the cutoff frequency, an FFT analysis is performed for the targeted time series. In Figure 5.2 WF and HF represent wave frequency and high-frequency components of the time series.

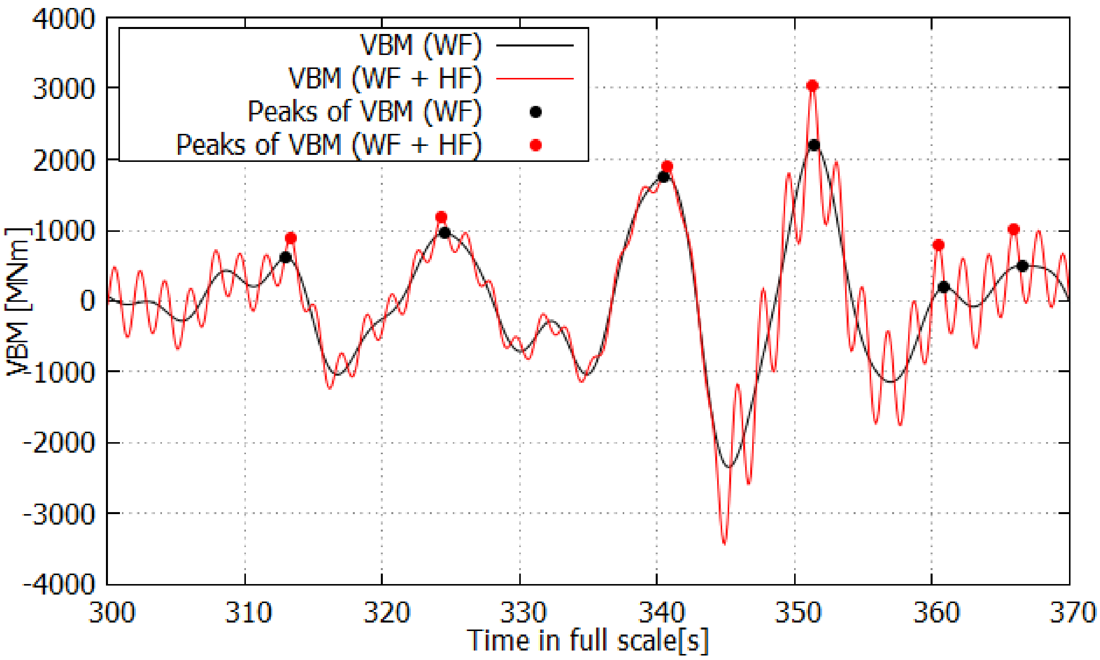

Figure 5.2 An example of counting individual peaks using zero-up-crossing method.

5.2 Numerical Model

A one-dimensional Euler beam model with 21 elements is chosen as to represent the 6600 TEU containership (Table 5.1) in the FE solver LS-DYNA. The FE model properties are given in the Table 5.3. The FE model has the material properties of

Aluminum alloy, which is same as the experimental backbone. Also, the 2-node natural frequency of the FE and experimental model is also the same. The weight distribution of the model is also mentioned in the Figure 5.3. The same boundary condition as well as the solver is chosen as mentioned in section 2.2.

For the fluid domain modeling, the same CFD specifications are used in this case as mention previously in section 2.1.

Table 5.3 Model properties of the FE model

Young's modulus	70,000 [MPa]
Poisson ration	0.3
Cross-sectional area	1.297E+07 [mm^2]
Area moment of inertia	7.318E+14 [mm^4]

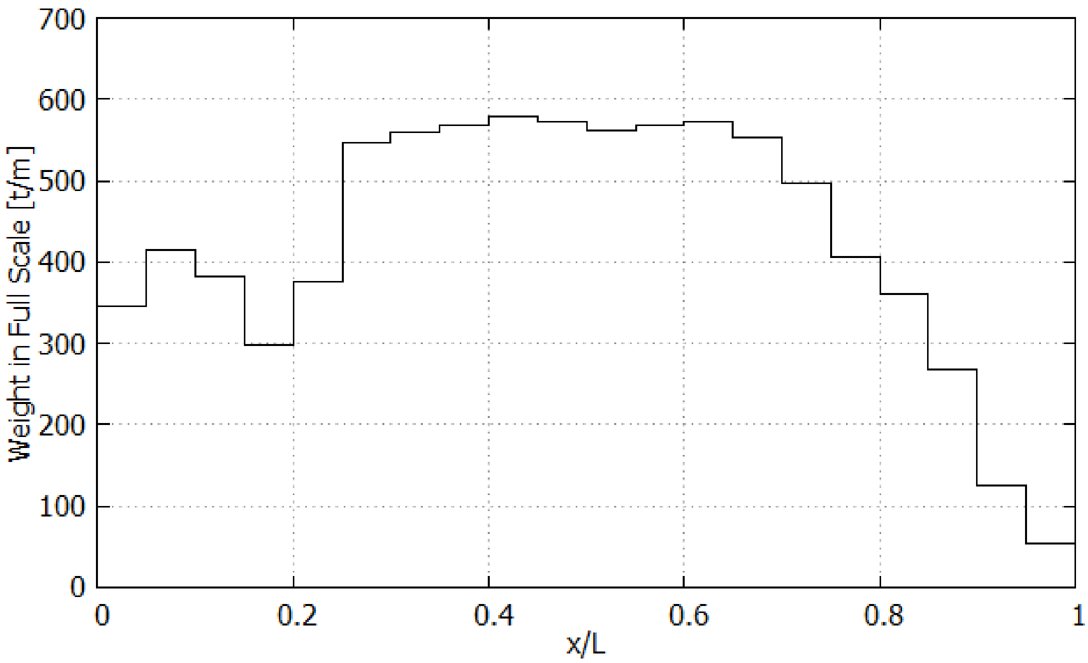

Figure 5.3 Weight distribution of the FE model

5.3 Comparison of Wave-induced and Whipping-induced Component

The current ROM is an improvement of the previous model proposed by Takami et al. [18]. The previous ROM of the VBM by whipping does not sufficiently reproduce the results of the coupled CFD-FEM analysis, which is thought to have caused the discrepancy in the exceedance accuracy. Therefore, the ROM of the whipping-induced VBM is further tuned and further development is done after that. Therefore, first, the wave and whipping-induced components of the reduced order model are discussed here with the possible scope of improvement.

First, the CFD-FEA one-way coupling analysis is performed for the wave episode shown in Figure 5.4. Then corresponding calculated VBMs from ROM and one-way coupling are compared in Figure 5.5-5.6. From the Figure 5.5 it can be seen that the ROM generally reproduces the results of the CFD-FEM coupled analysis before the onset of the whipping vibration. However, there is a discrepancy between the two-time series after the whipping elastic vibration appears. In Figure 5.6, only the wave-induced component is plotted. The wave components of the FEM coupled analysis were extracted using a low-pass filter and subtracted from the original time series data. The cutoff frequency for LPF is set to 0.4 Hz on the full scale. The elastic vibration component is separately plotted in Figure 5.7. It can be seen from Figure 5.7 that around t=155s a large vibration with an amplitude of about 1000 MNm appears, and then it decays. It can be seen that the whipping vibration of the ROM is much larger than that of the coupled CFD-FEM analysis and needs to be corrected.

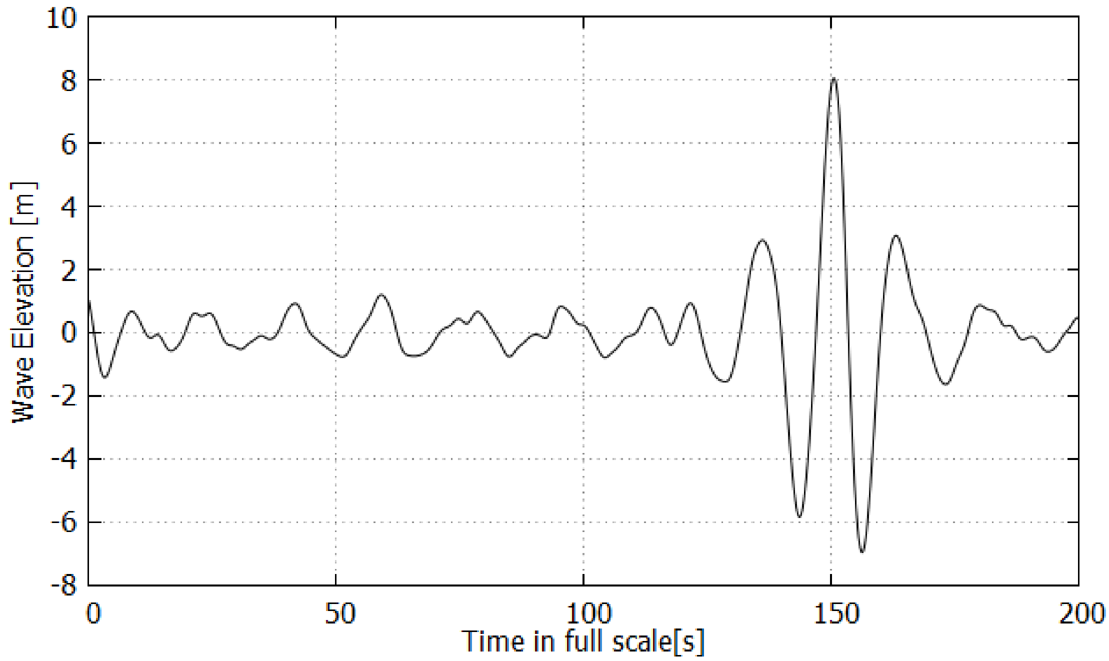

Figure 5.4 Wave episode for target response: 4000 MNm

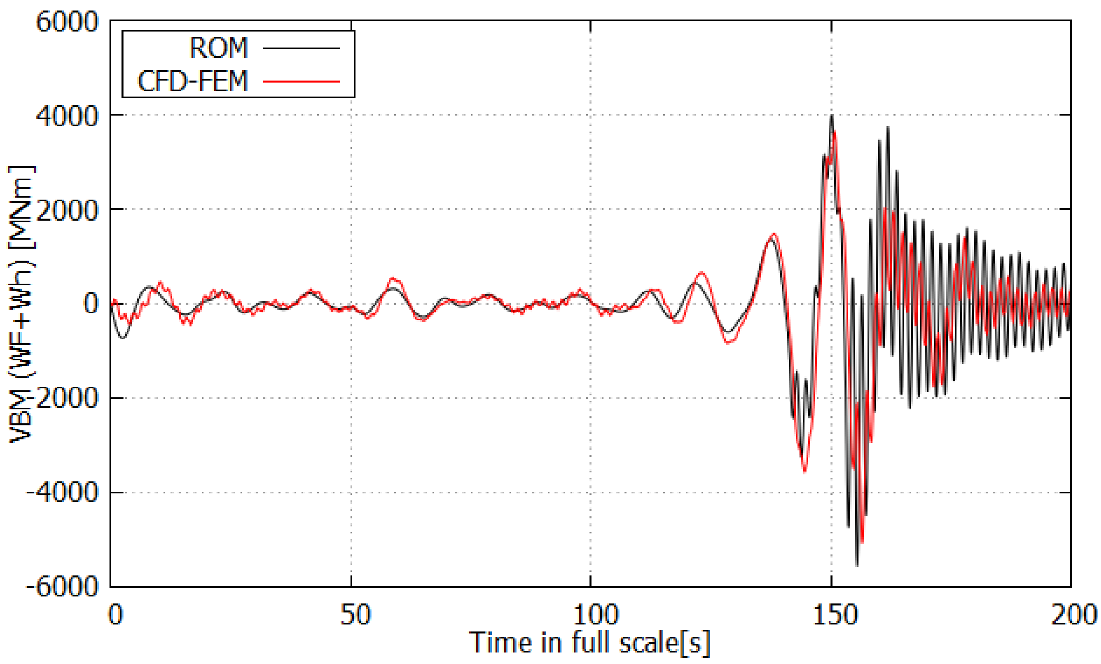

Figure 5.5 Comparison of VBM time series obtained from ROM and coupled CFD-FEM method under wave episode for target response: 4000 MNm

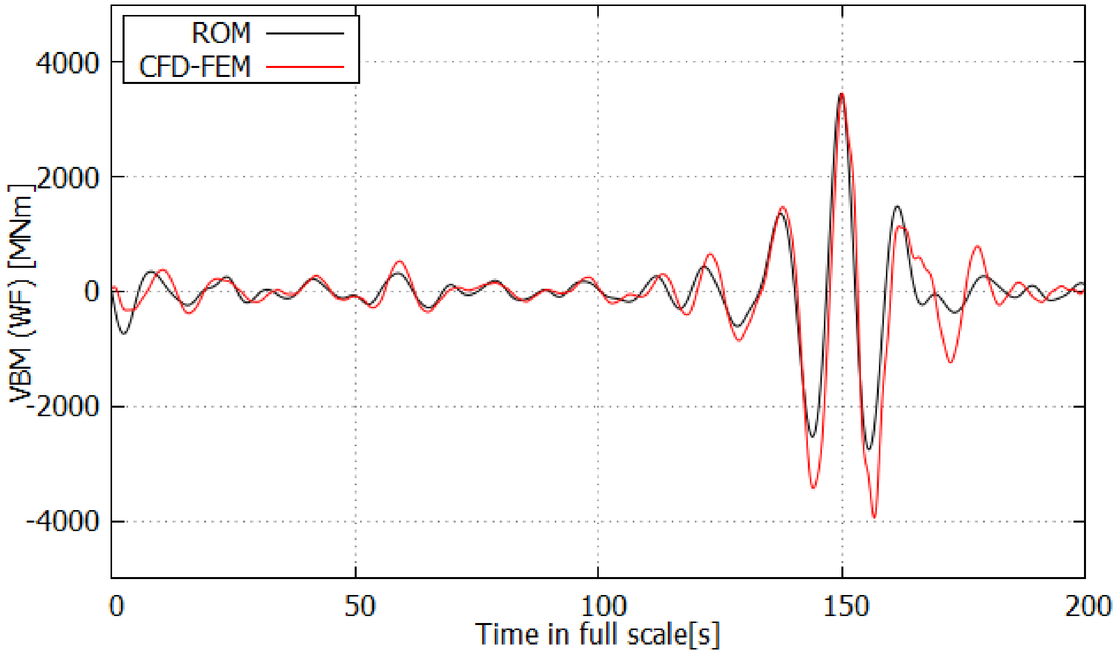

Figure 5.6 Comparison of wave induced VBM between results from ROM and coupled CFD-FEM method under wave episode for target response: 4000 MNm

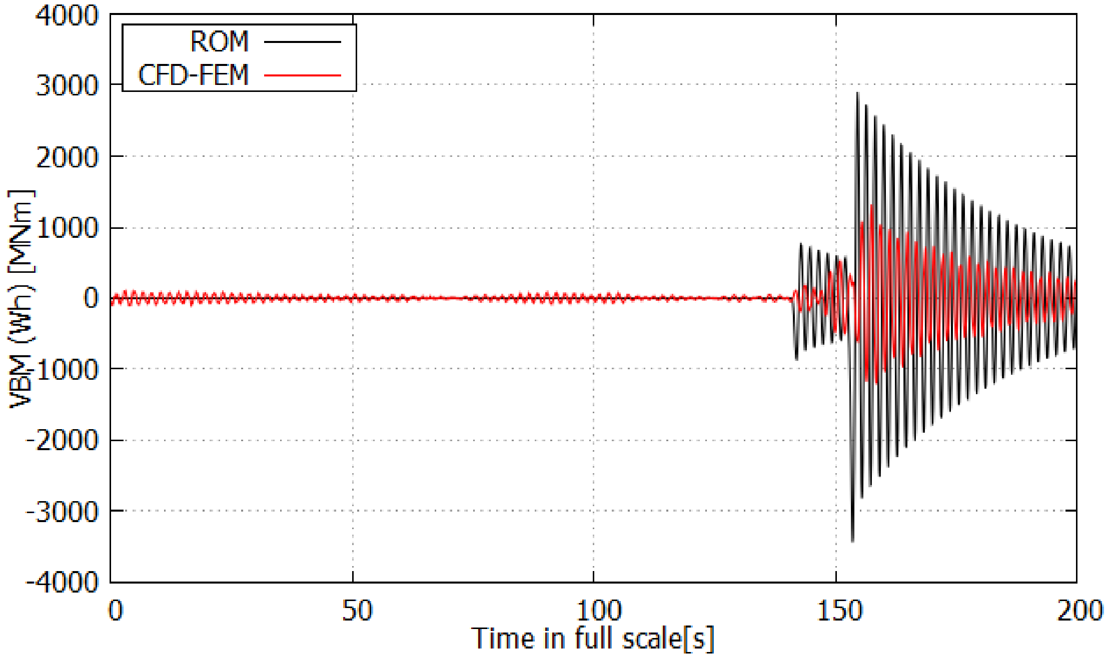

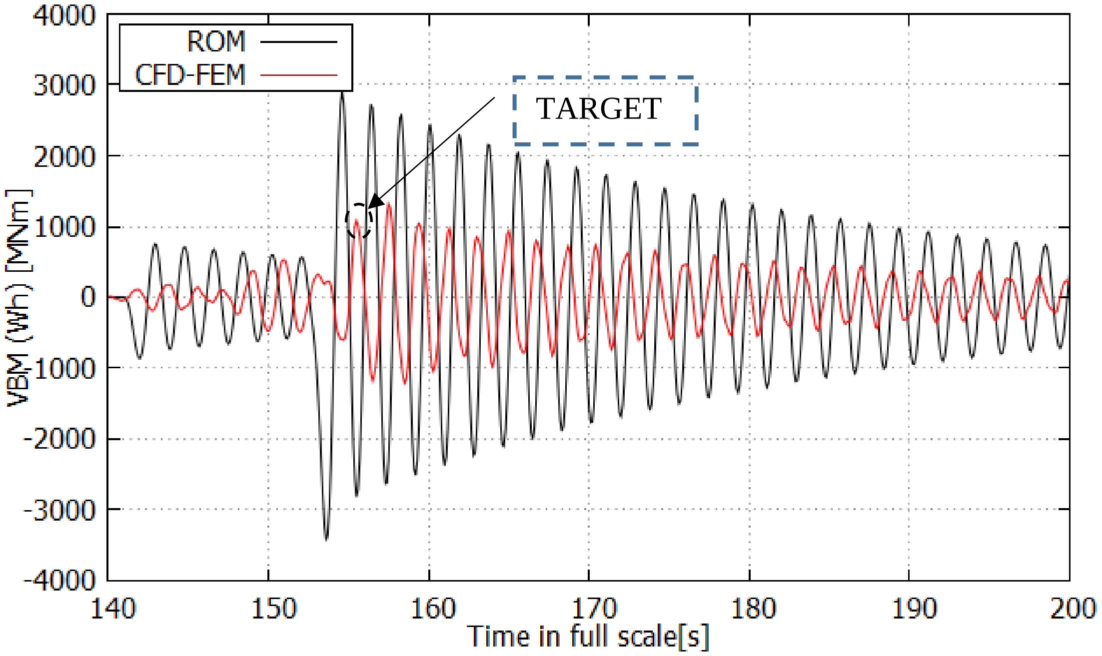

Figure 5.7 Comparison of whipping VBM between results from ROM and coupled CFD-FEM method under wave episode for target response: 4000 MNm

In Figure 5.8 water entry and exit of the bow corresponding to the wave episode mentioned in Figure 5.4 are shown. The time pointed out in the image is in model scale which is 158-158.3s in full scale. On the left figure, the volume of fluid in each cell is plotted and on the right figure the intensity of pressure using a color map. Similarly, due to significant pitch motion, the stern of the vessel also experiences the water entry and exit phenomenon, which induces slamming. In the left of Figure 5.9 volume of fluid at the free surface near the stern is shown and the right figure shows the pressure intensity due to the water entry-exit problem. It can be visualized from the color bar of the pressure intensity plot in Figure 5.8-5.9 that the bow slamming is severe compared to the stern in this particular wave case scenario.

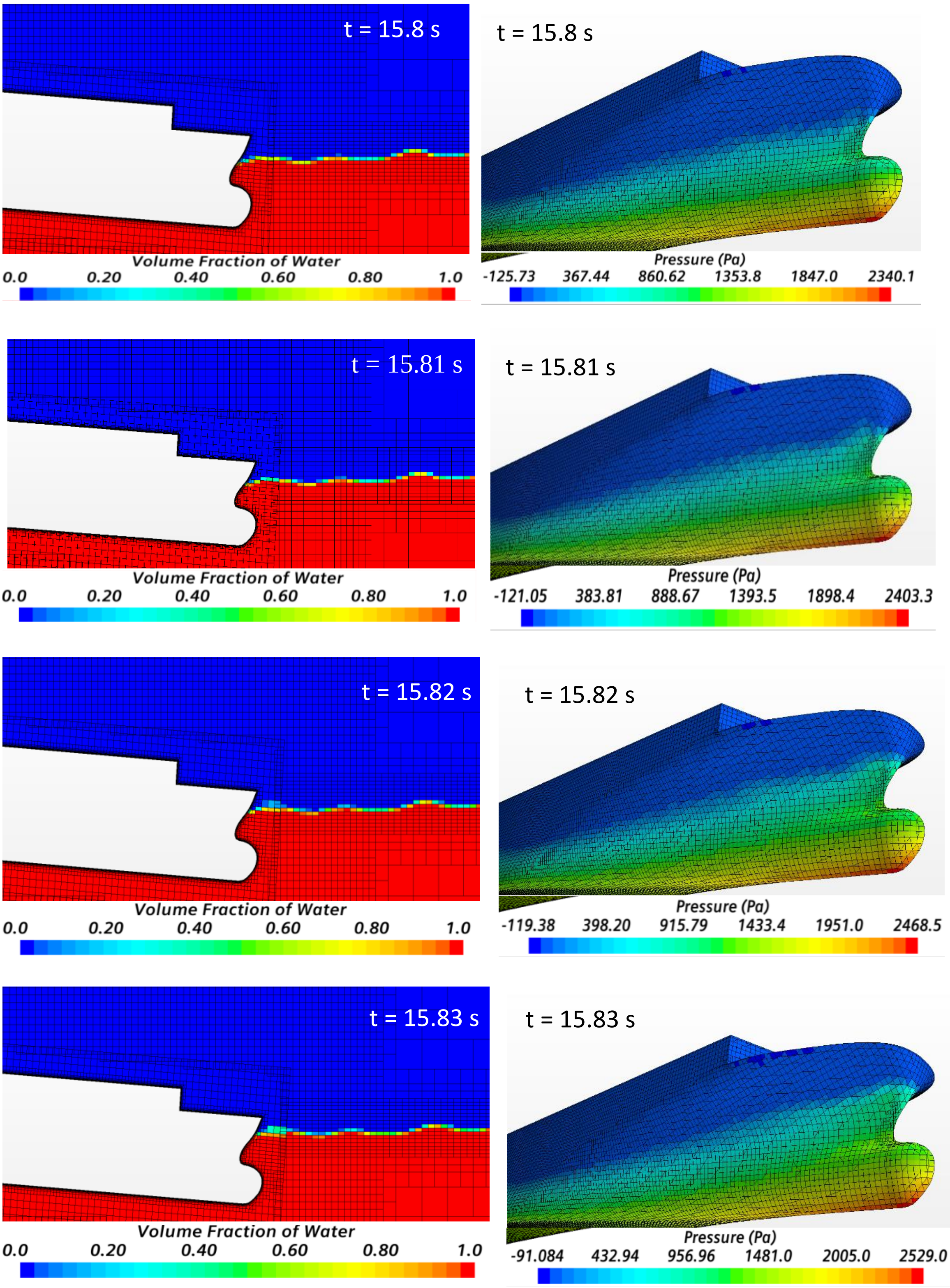

Figure 5.8 Snapshots of volume of fluid of CFD model's bow section at t=158~158.3 s in full scale

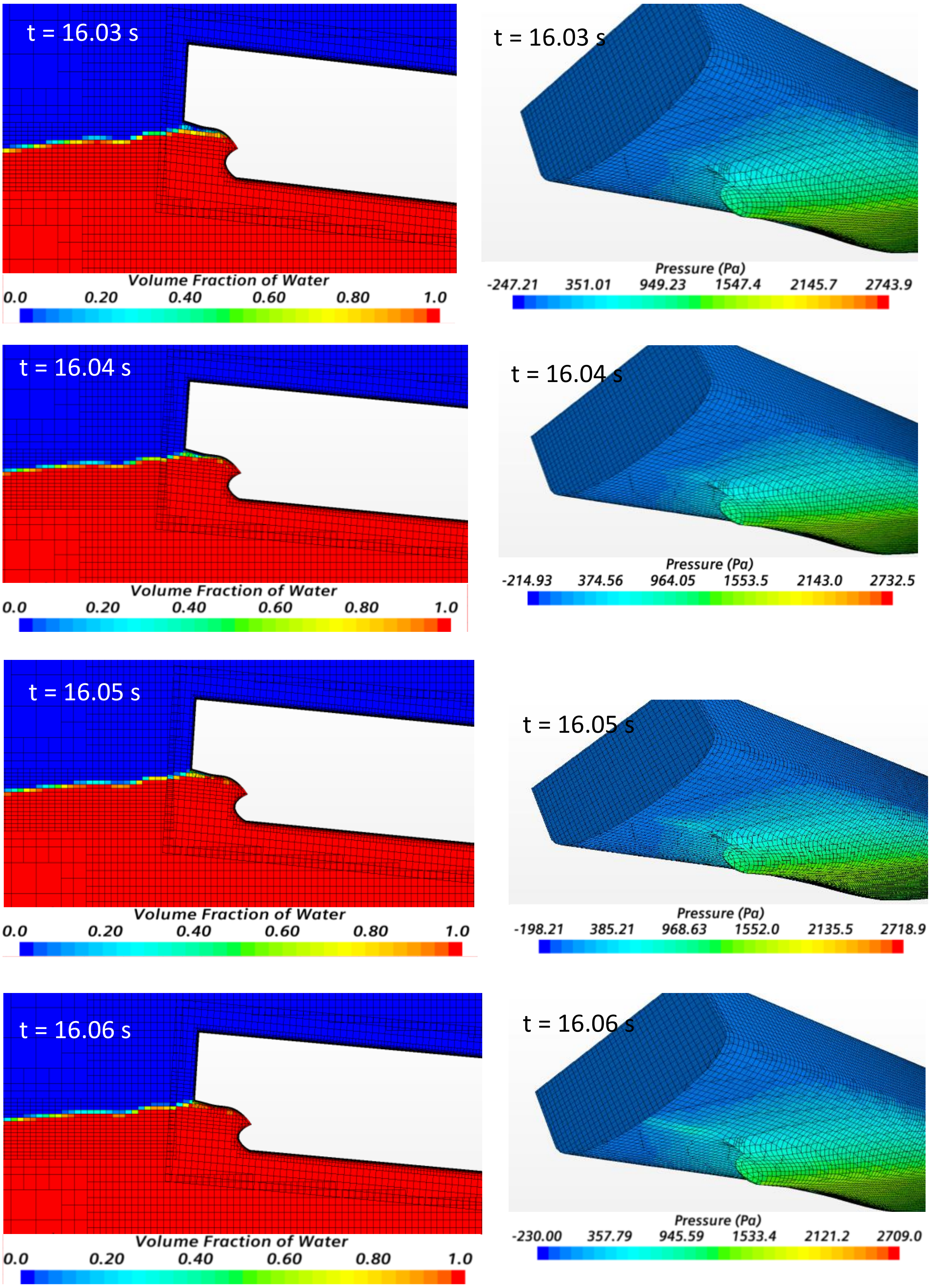

Figure 5.9 Snapshots of volume of fluid CFD model's stern section at t=160.3~160.6 s in full scale

To understand the extent of stern slamming in this case the impulse load is tried to plot separately by mapping the pressure to the specific portion of the hull decided from the VOF image in Figure 5.8-5.9. In Figure 5.10 the corresponding meshes are shown for the bow and stern sections. In Figure 5.11 the impact load is plotted for bow and stern regions. Although Figure 5.11 also has wave component, especially in the stern region, the impulse load is visible in both cases. Therefore, we can surely comment that bow slamming impact is significantly higher than that of the stern. However, the whipping vibration component caused by stern slamming may also be with the VBM time series. This can be done by analyzing the ROM model under several design irregular wave episodes or irregular waves, comparing the mechanism and magnitude of stern slamming from the coupled CFD-FEM analysis. However, for this wave episode, the stern slamming component in ROM was not used.

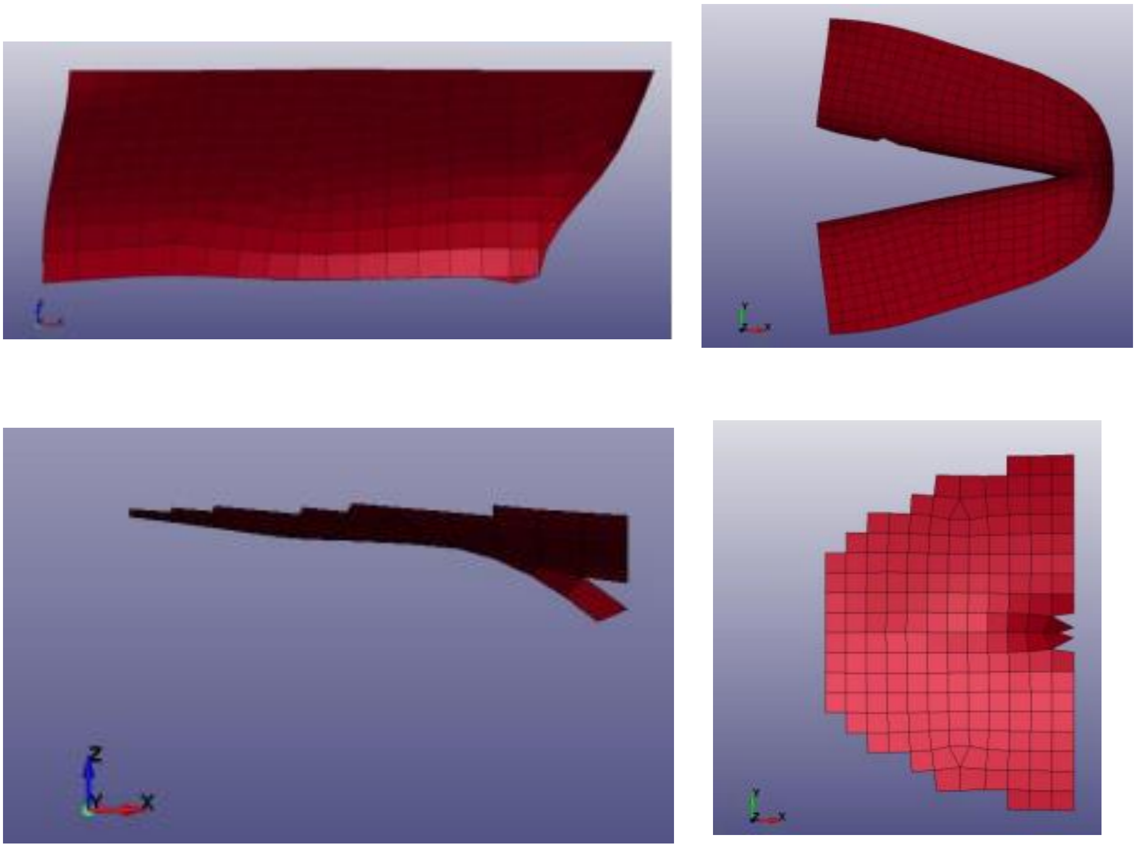

Figure 5.10 Areas of bow and stern where slamming impact loads are expected to occur (upper denote bow and lower denote stern)

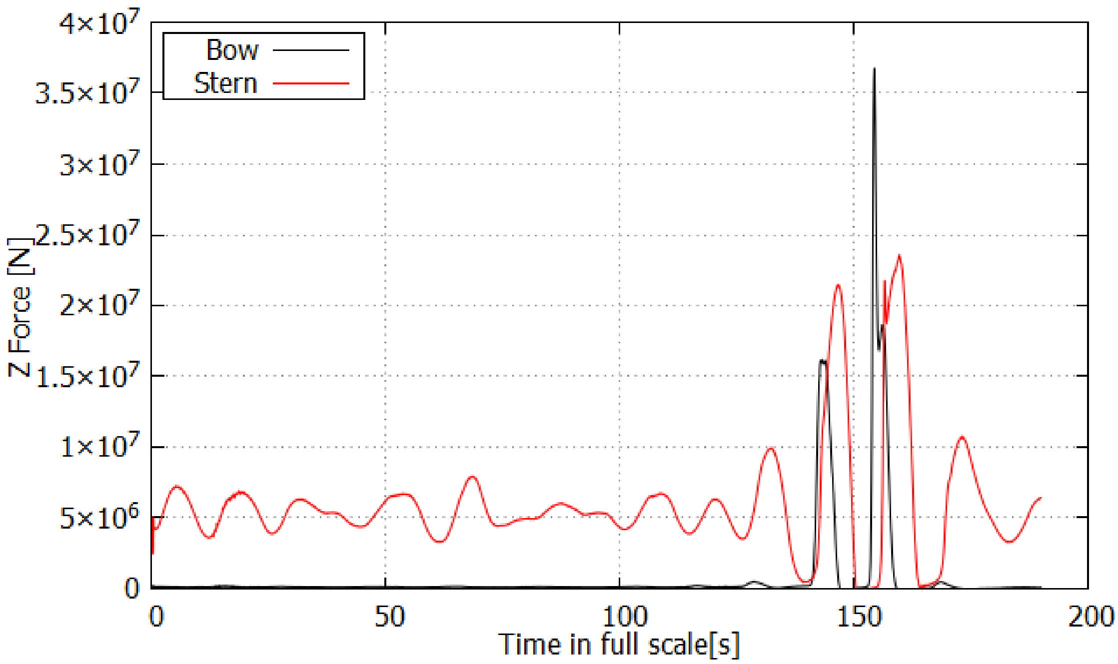

Figure 5.11 Comparison of the vertical force time series acted on bow and stern

First, the frequency and damping of the ROM are checked whether it matches the frequency and damping of the elastic vibration component of the CFD-FEM coupled analysis. If they are different, they can be adjusted by changing ζ and ω_0 in equation (4.7). The frequency and decay of the elastic vibration were consistent with the results of the CFD-FEM coupled analysis, so no change was made. Next, the coefficients d, δ, c_{imp}, and τ_{imp} described in section 4.2 were optimized to fit the results of the CFD-FEM coupled analysis. In this study, by changing c_{imp} and τ_{imp}, the amplitude and phase at the start of the whipping vibration (Target in Figure 5.7) were adjusted to match. The vertical bending moment elastic vibration components obtained from the modified ROM are compared and shown in Figure 5.12. It can be seen that the results are much more consistent than before the modification. The flowchart of the whole procedure is given in Figure 5.13.

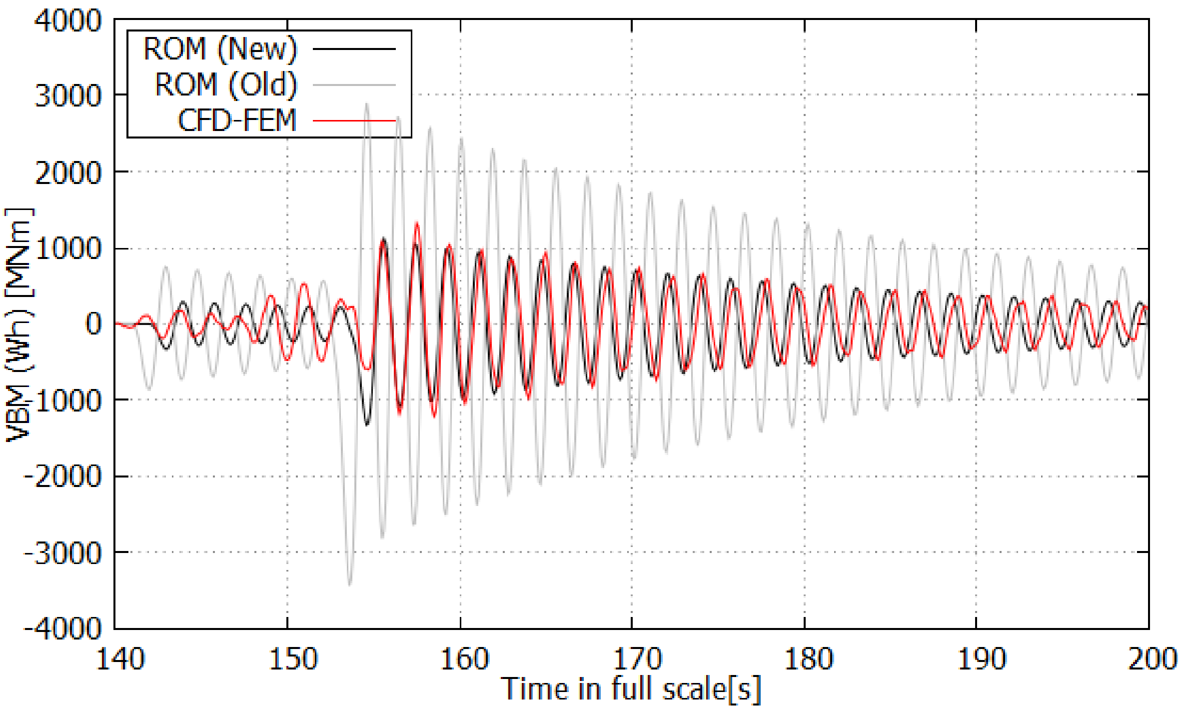

Figure 5.12 Comparison of whipping VBM between before (old) and after (new) adjusting ROM model

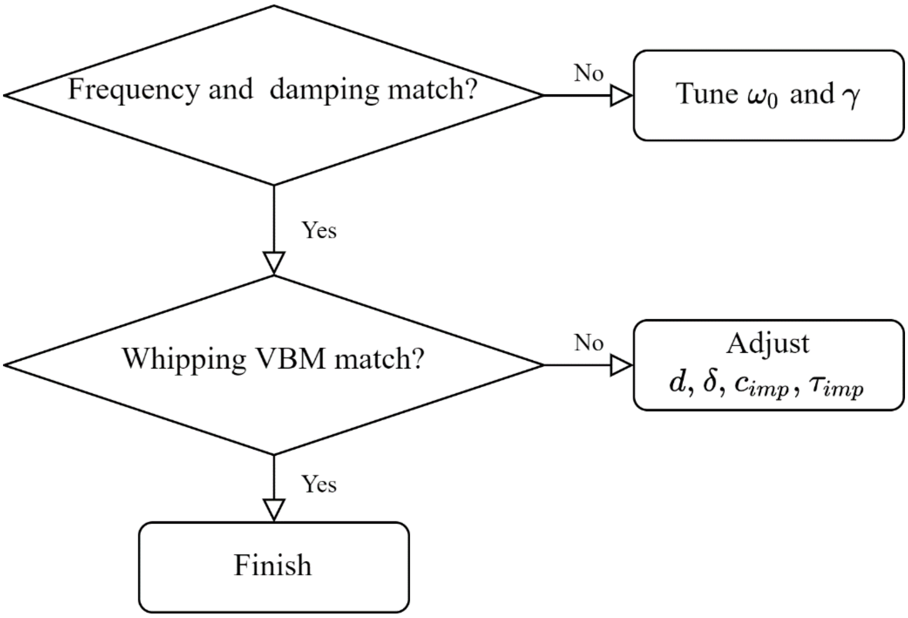

Figure 5.13 The flowchart for adjusting ROM for whipping VBM

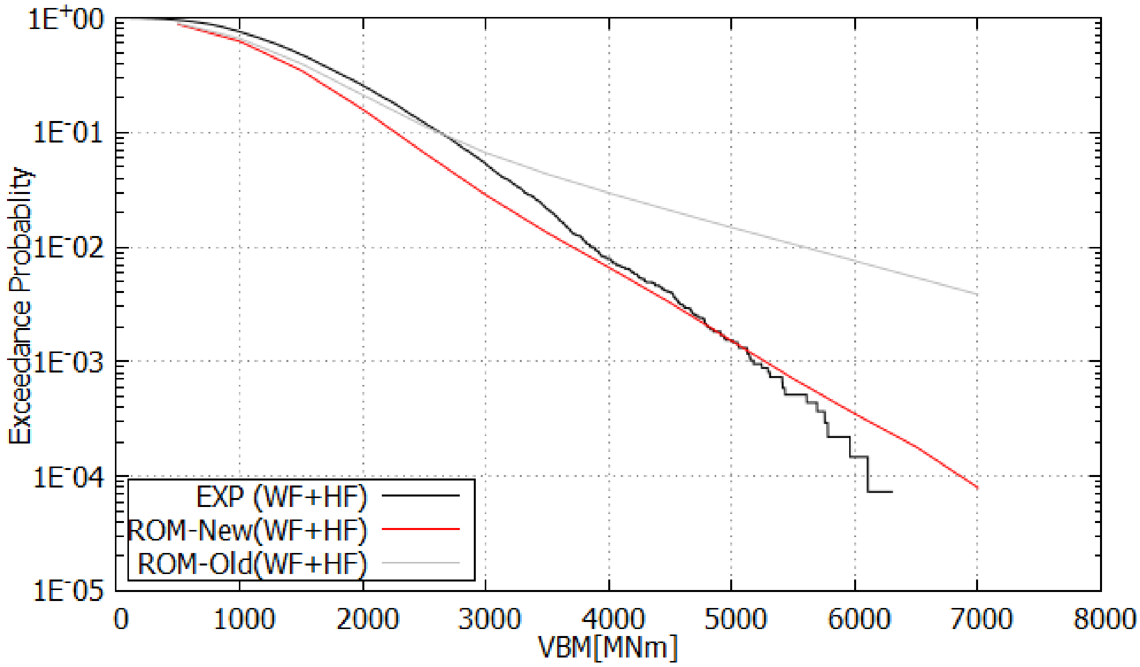

Figure 5.14 Exceedance probabilities of vertical bending moment calculated from old and new ROMs and experiment

Figure 5.14 shows the exceedance probability of the vertical bending moment derived using the modified ROM and compared with the previous setup. As a result of the modification, the whipping vibration became smaller and the overall accuracy increased. In particular, the accuracy level of 1.0×10^{-3} was very close to the experimental value. On the other hand, at the higher probability levels of 1.0×10^{-1} to 1.0×10^{-2}, the deviation from the experimental value was larger than that before the correction. The cause of the discrepancy is some components that cannot be expressed in the current ROM. Therefore, it affects the extreme value distribution.

5.4 Comparison of Springing Behavior

The experimental VBM time series corresponding to the wave in Figure 5.16 is plotted in Figure 5.15. The dynamic and wave components of VBM in Figure 5.15 are separately plotted in Figure 5.17 using BPF with a cutoff frequency of 0.3 Hz in full scale. It can be noticed from the wave profile that, although slamming does not happen between 90-100s, there are still high-frequency components in the VBM time series. Although it might seem like this is small vibration, however, accumulation of these over a large sample period may significantly affect the extreme value distribution curve.

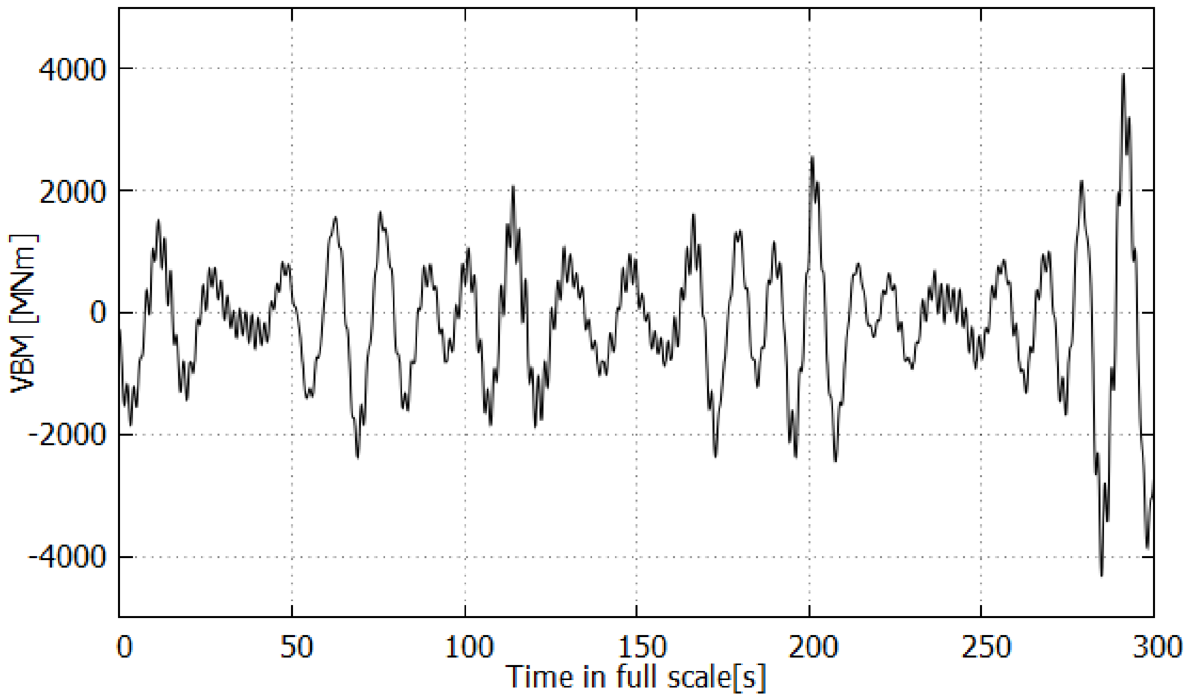

Figure 5.15 An example of vertical bending moment time series derived from the past experiment by Takami et al. [18]

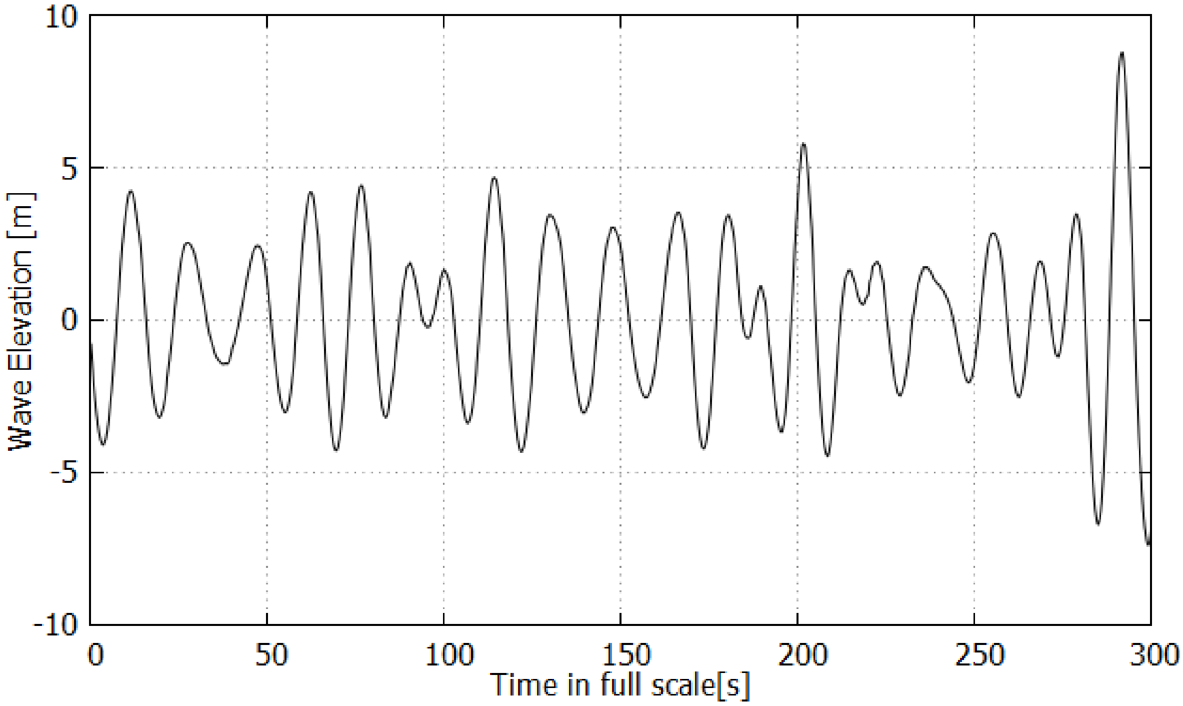

Figure 5.16 Wave time series at amidships obtained from the past experiment by Takami et al. [18]

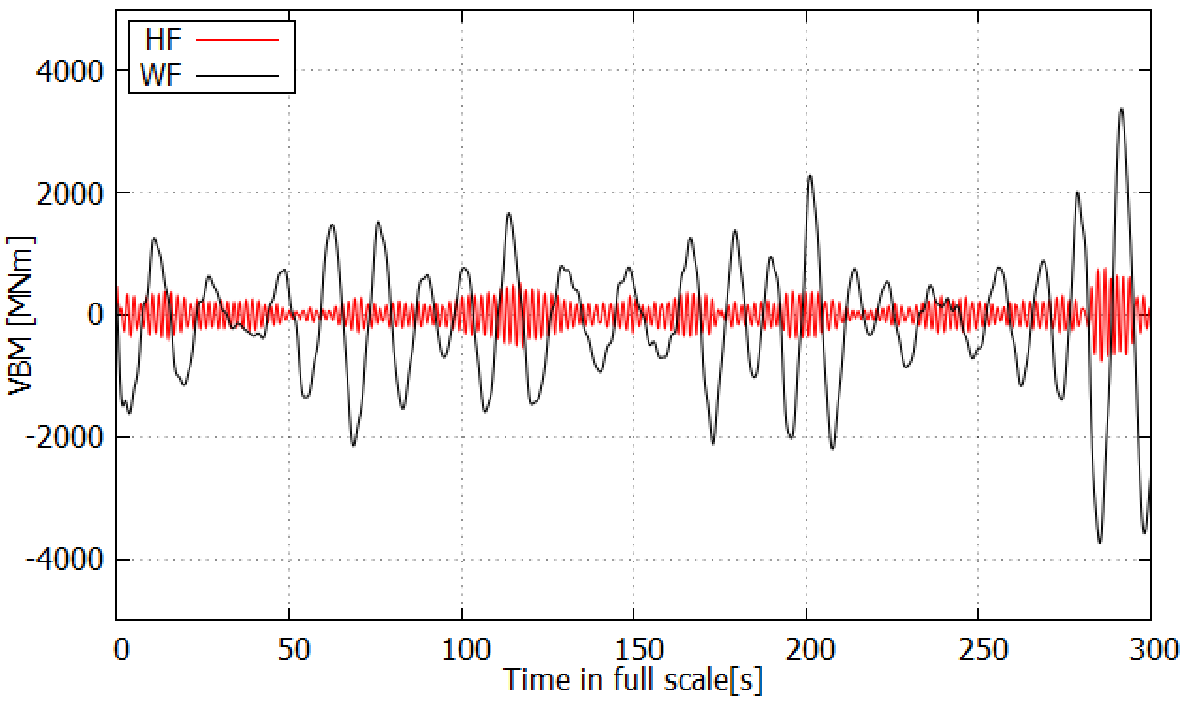

Figure 5.17 VBM time series of wave induced component and high frequency component obtained from Figure 5.15

In order to account for the contribution of springing in the ROM, the amplitude of vibration should be specified as mentioned in equation (4.9) section 4.3. First, the distribution of extreme values of elastic vibrations observed in the experiment is confirmed using Quantile-Quantile (QQ) plot and Percentile-Percentile (PP) plot. For this, the high-frequency component is separated using a low-pass filter with a cutoff frequency a little above the range of wave frequencies (WF) which is shown in the black line in Figure 5.18. Thereafter, the peaks are identified, which is shown in red marks in Figure 5.18. This data is measured for 6.4 h on an actual scale. It was observed that both springing and whipping were present in this experimental data. Therefore, to remove the whipping component of VBM from the distribution, VBM larger than 700 MNm is not considered (Figure 5.19). This is decided upon observing the experimental data, which confirms slamming-induced vibrations tend to have higher peaks than the decided cutoff. This assumption is confirmed further by checking the fitting range of the best-fitted statistical distribution. For checking which statistical distribution fits well, QQ and PP plots were considered for Rayleigh, Weibull, and Log-normal distributions (Figure 5.20-5.21).

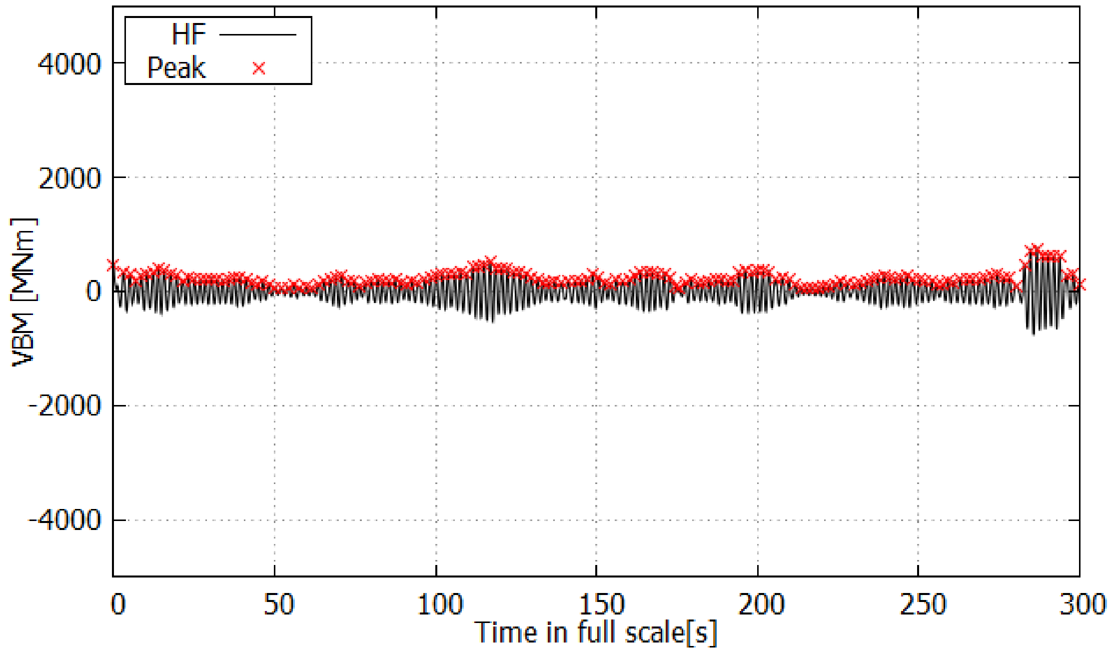

Figure 5.18 An example of counting peaks of high frequency component of VBM.

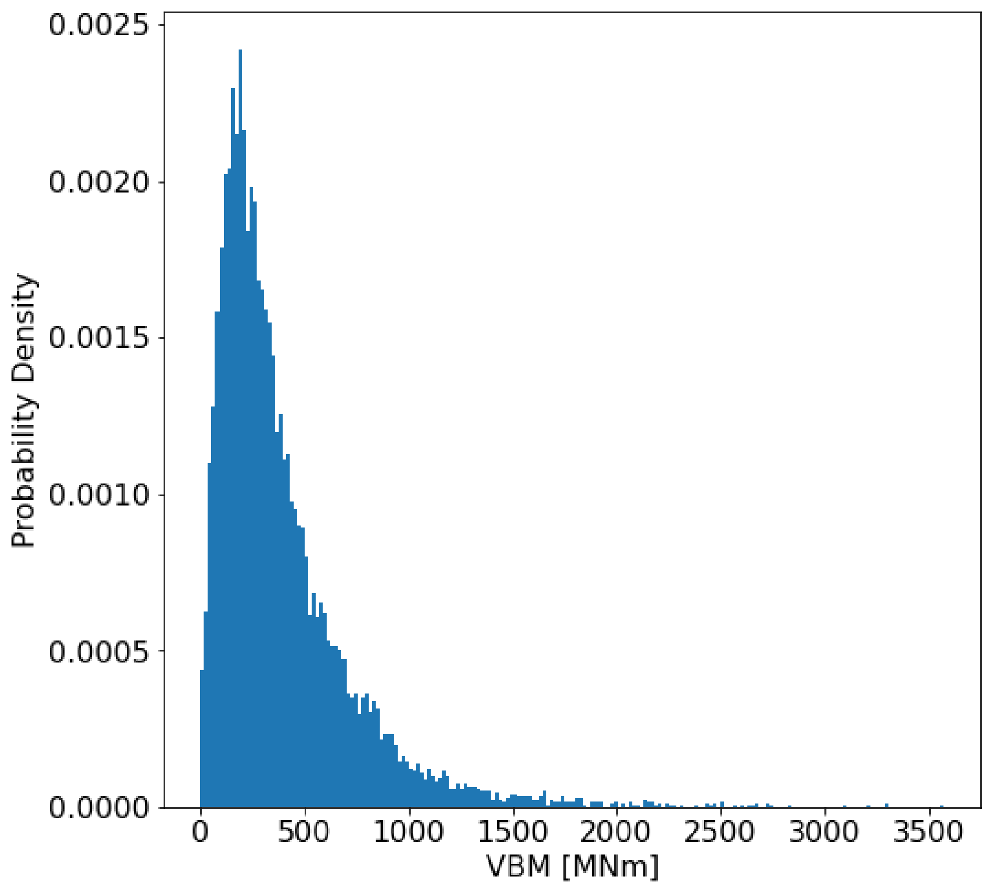

Figure 5.19 Distribution of high frequency peaks observed in Figure 5.18

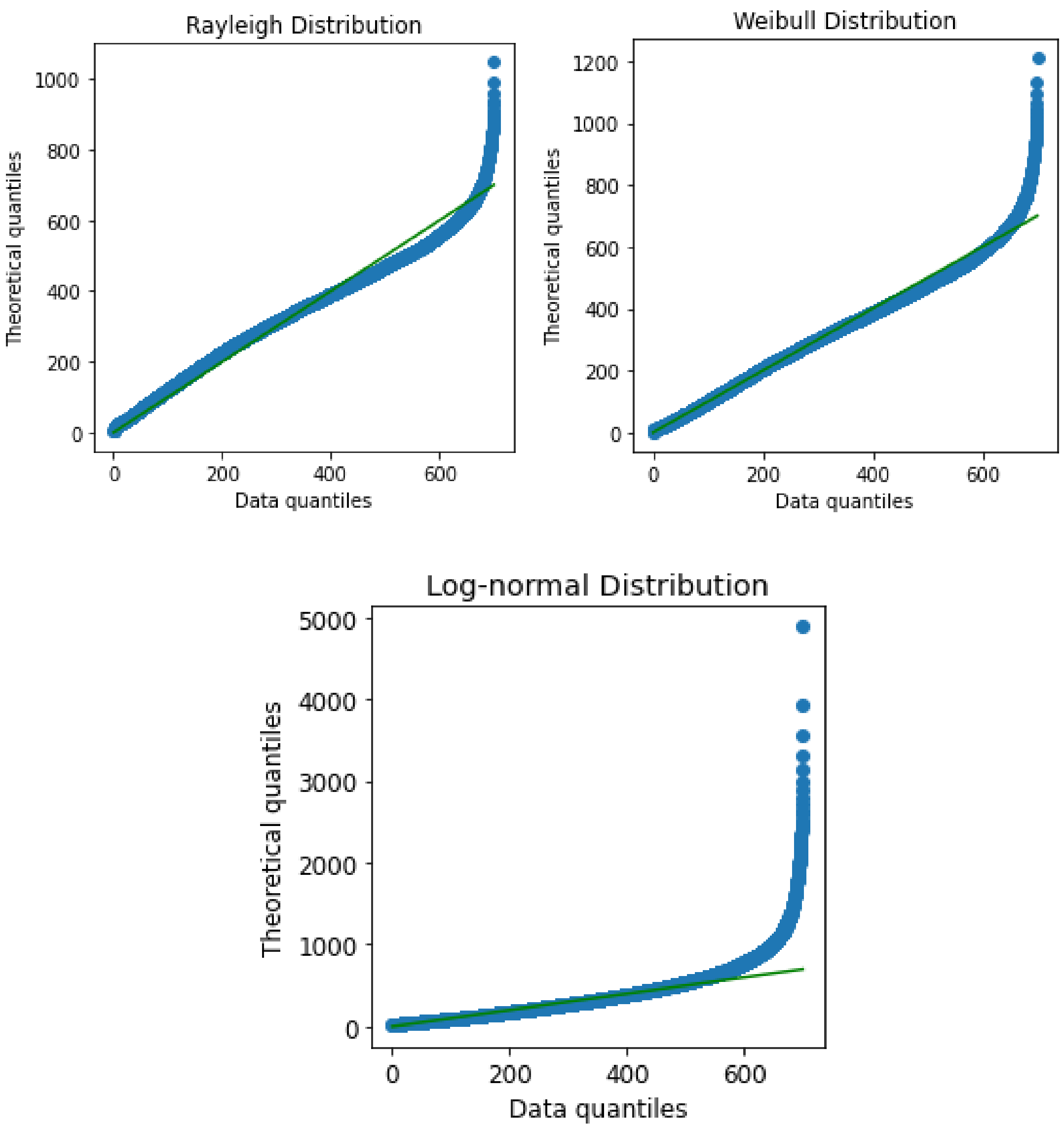

Figure 5.20 QQ plots using Rayleigh, Weibull, and Log-Normal distributions

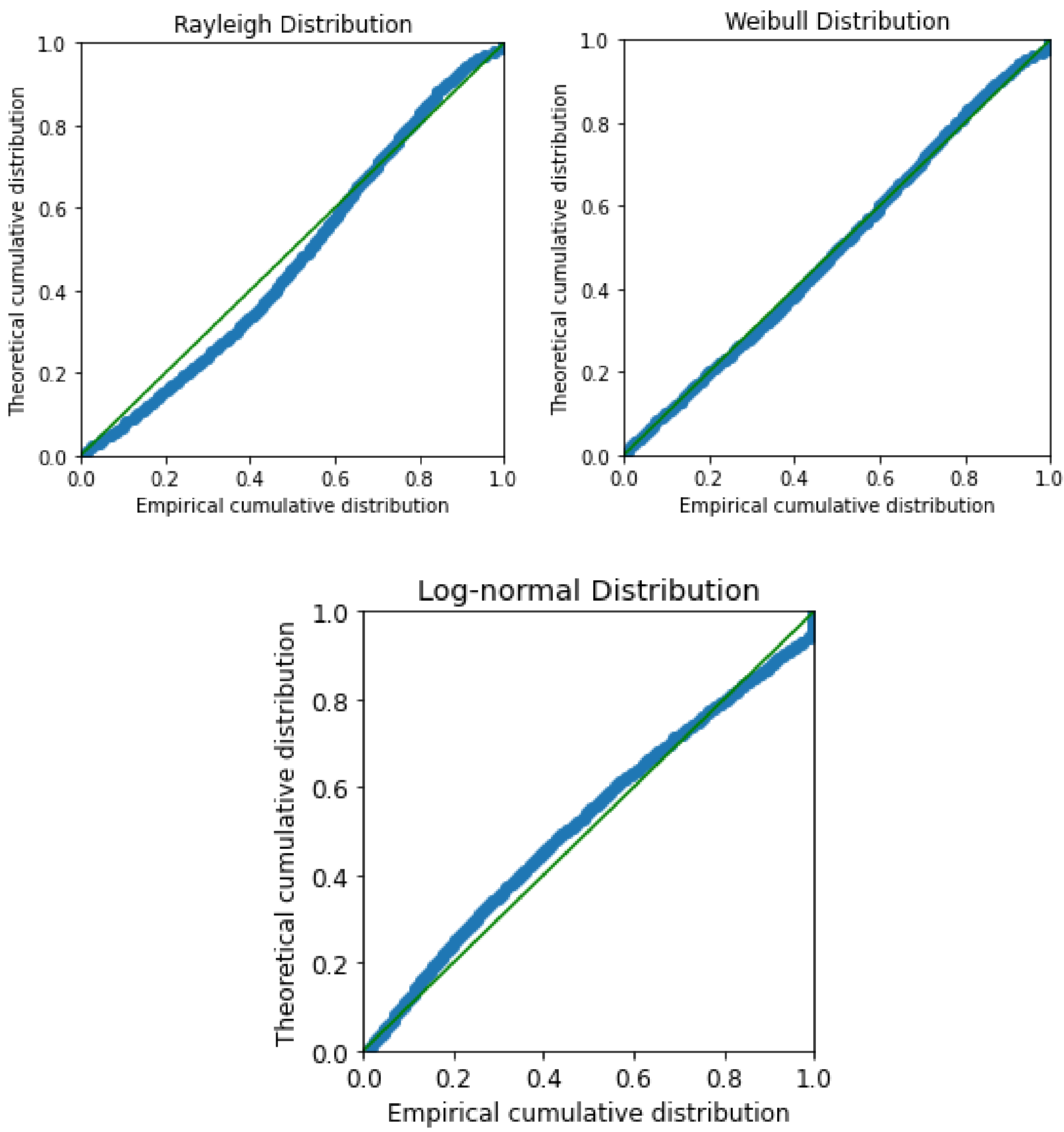

Figure 5.21 PP plots using Rayleigh, Weibull, and Log-Normal distributions

From the QQ plot in Figure 5.20, it can be observed that the below 700 MNm distribution matches well with Rayleigh and Weibull distributions. However, from the PP plot in Figure 5.21, it can be confirmed that the distribution well matches the Weibull distribution. Therefore, the A_{spr} is calculated using the Weibull distribution with shape parameter m equal to 1.97 and scale parameter η equal to 320.5. The phase (ε_{ni}) in equation (4.9), is calculated by adjusting the springing component of ROM VBM with CFD-FEM coupling.

In Figure 5.26 FFTs of the VBM time series from the experimental regular wave cases are shown. It was observed that every regular wave case has higher order springing phenomenon by following a direct multiplication of the integer with the wave frequency. Therefore, it follows the proposed springing model in equation (4.8). In Figure 5.26 it can be noticed that the springing component near 2-node natural frequency is much greater than that of other ranges. This is because the springing component excites the 2-node vibration. In this research, therefore, only the springing frequency near the 2-node vertical vibration is considered in this analysis. The validation of the proposed CFD-FEA one-way coupling method for the springing calculation is given in reference (Pal et al., [20]; Pal and Iijima, [21]).

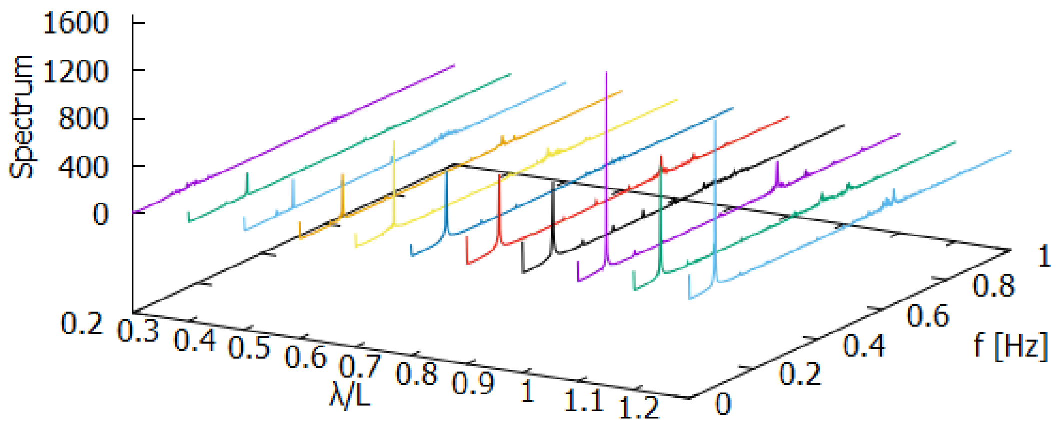

Figure 5.22 Spectrum of VBM under regular wave experiments

Next, CFD-FEM coupled analysis is performed in irregular waves to compare the analysis results and confirm whether the proposed springing vibration is appropriate. As an irregular wave episode, the wave episode shown in Figure 5.27 is used. Figure 5.24

compares the vertical bending moment time sequences obtained from the CFD-FEM coupled analysis and the ROM, respectively. The extremely high vertical bending moment of CFD-FEM between 0 and 20s is thought to be due to the sudden loading of FEM. From the 20s onward, the vertical bending moments of the two are close to each other. Although the results seem to generally mimic those of the CFD-FEM coupled analysis, the results of the CFD-FEM coupled analysis after the 210s show elastic vibration that is not exactly in the ROM. To investigate the cause of the deviation in detail, the time series is compared by dividing it into wave and high-frequency components. Figure 5.29 shows a comparison of the vertical bending moment's wave component, and Figure 5.30 shows a comparison of the high-frequency component. In Figure 5.30 the high-frequency components of the ROM are also compared with the time series with and without the addition of the springing vibration (i.e., only the whipping vibration component). The high-frequency components in Figure 5.31 show that they differ greatly from the results of the CFD-FEM coupled analysis, especially at t=200~250 s.

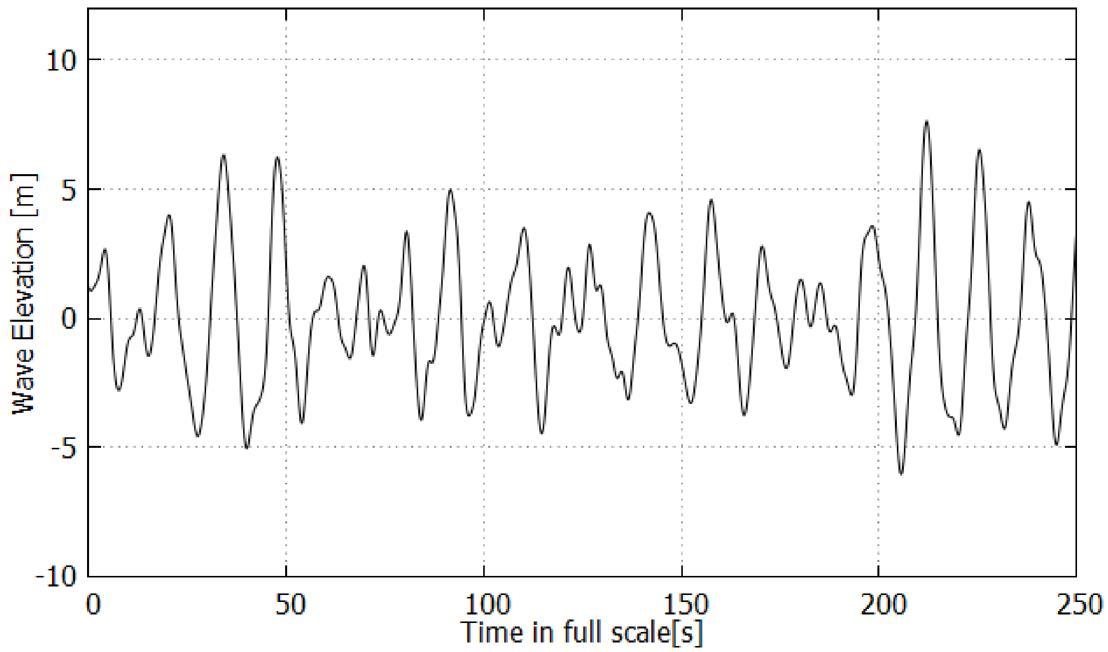

Figure 5.23 The irregular wave time series adopted for CFD-FEM coupled analysis

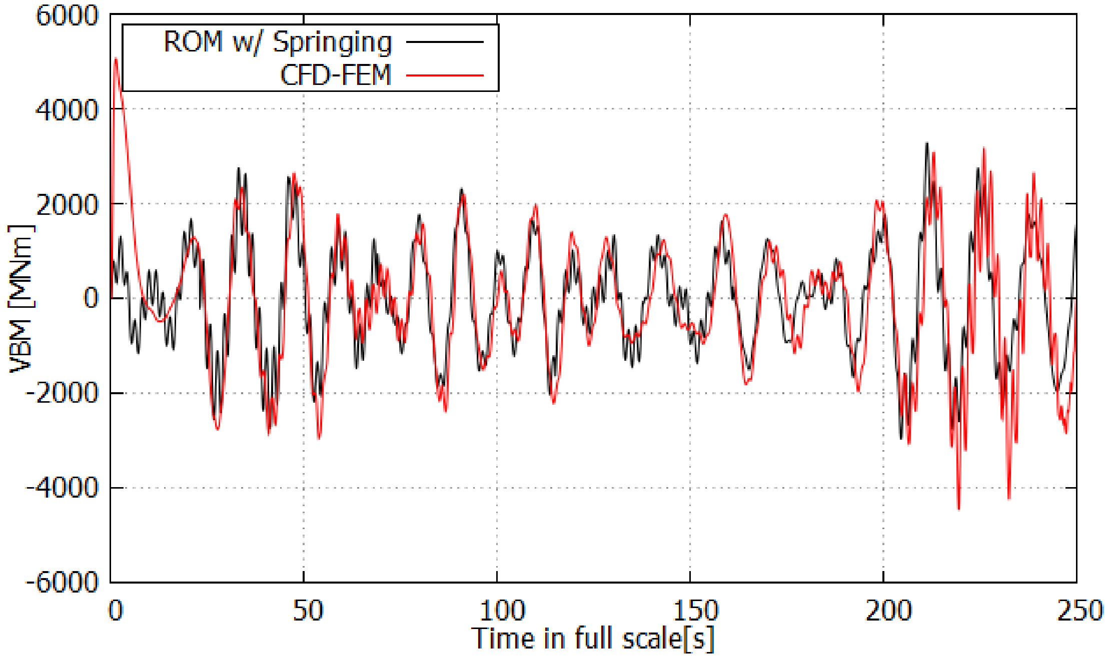

Figure 5.24 Comparison of VBM time series under irregular wave derived from CFD - FEM coupled analysis and ROM

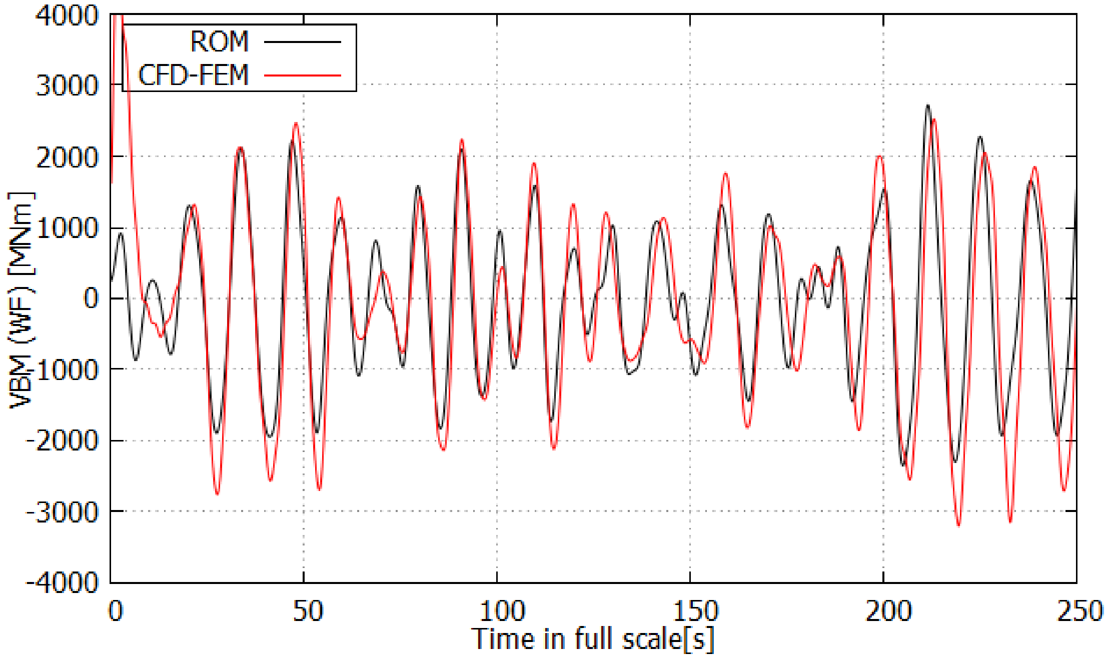

Figure 5.25 Comparison of wave induced component of VBM time series under irregular wave derived from CFD-FEM coupled analysis and ROM

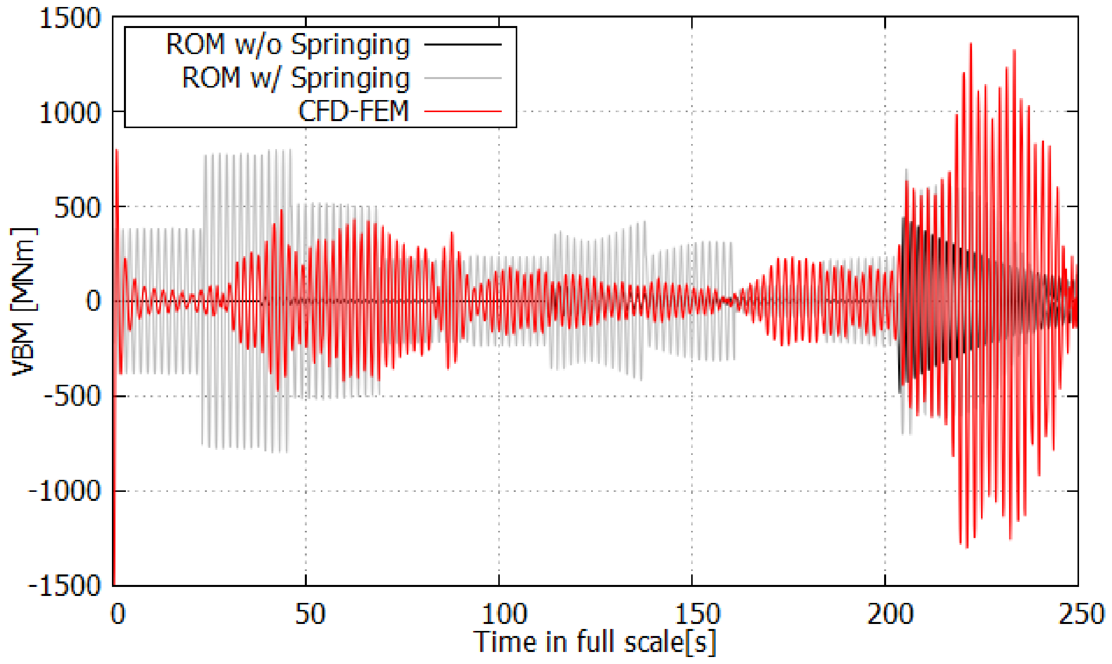

Figure 5.26 Comparison of high frequency component of VBM time series under irregular wave derived from CFD-FEM coupled analysis and ROM

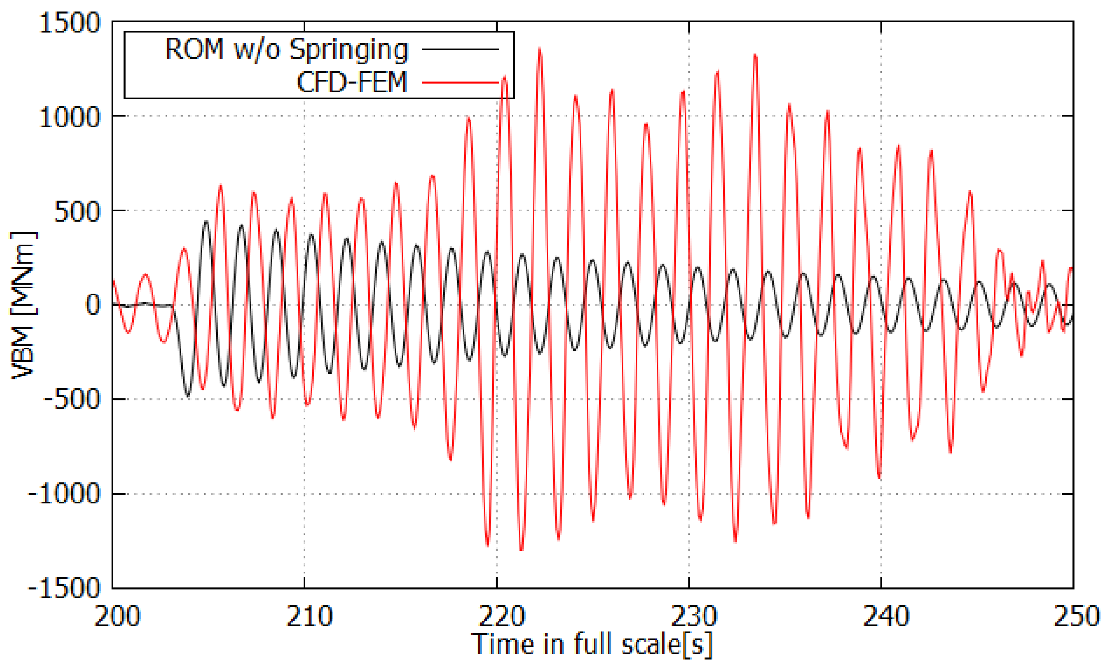

Figure 5.27 Magnified view of Figure 5.30 around 200-250s

5.5 Limitations of the Method

In Figure 5.26 the elastic vibration component exceeding 1000 MNm is dominated by whipping vibration. In magnified view of Figure 5.30 shows a comparison between the whipping vibration component of the ROM and the CFD-FEM coupled analysis. In the coupled CFD-FEM analysis, the elastic vibration becomes large around t=220s and exceeds 1000 MNm. In contrast, the ROM shows no such oscillation, and it decays constantly. In order to investigate the cause of this discrepancy, in Figure 5.28 the vertical section loads of the bow and stern is shown. It can be noticed that the stern slamming is more prominent than the bow slamming several times. It was found that the slamming impact load occurred consecutively after 200s. It was understood that the discrepancy after the 200s was mainly caused by the superposition of consecutive slamming phenomena. However, present ROM has not considered stern slamming, it could easily be included in the same way as bow slamming.

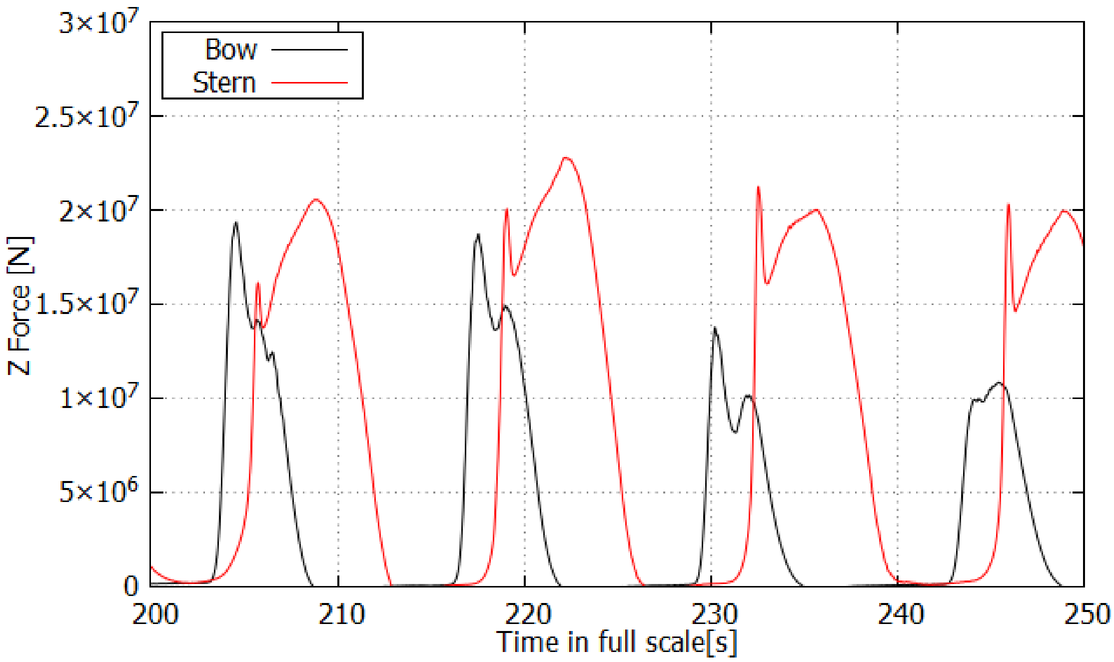

Figure 5.28 Vertical force time series acted on bow and stern under the irregular wave

5.6 Probability of Exceedance of VBM

Figure 5.29 shows the peak value distributions obtained from the experimental data. By superimposing the springing, the exceedance probability increased at a high probability level of 1.0×10^{-1} to 1.0×10^{-2}, approaching the probability obtained from the experiment. On the other hand, at the lower accuracy level of 1.0×10^{-3} ~ 1.0×10^{-4}, there is almost no change due to the springing, and the whipping vibration and wave components dominate. This means that whipping and springing are independent phenomena and therefore can be superimposed. The whipping component is much larger than the springing component in the range of low probability level. It can be seen that at the accuracy level of 1.0×10^{-4}, the simulation underestimates the experimental value by about 500 MNm. This difference can be partly explained by the statistical data uncertainty. It is observed that the tail of the probability distribution obtained from the experiment has a stepped shape. Note also that the normal wave VBM predicted by transfer functions and corrected, should have the deviations from the experiment or reality at the tail due to the limit of modeling. It is to be noted that, the VBM calculated by the IACS rule [35], is slightly smaller than the experimental and predicted VBM at the probability range of 1E-03.

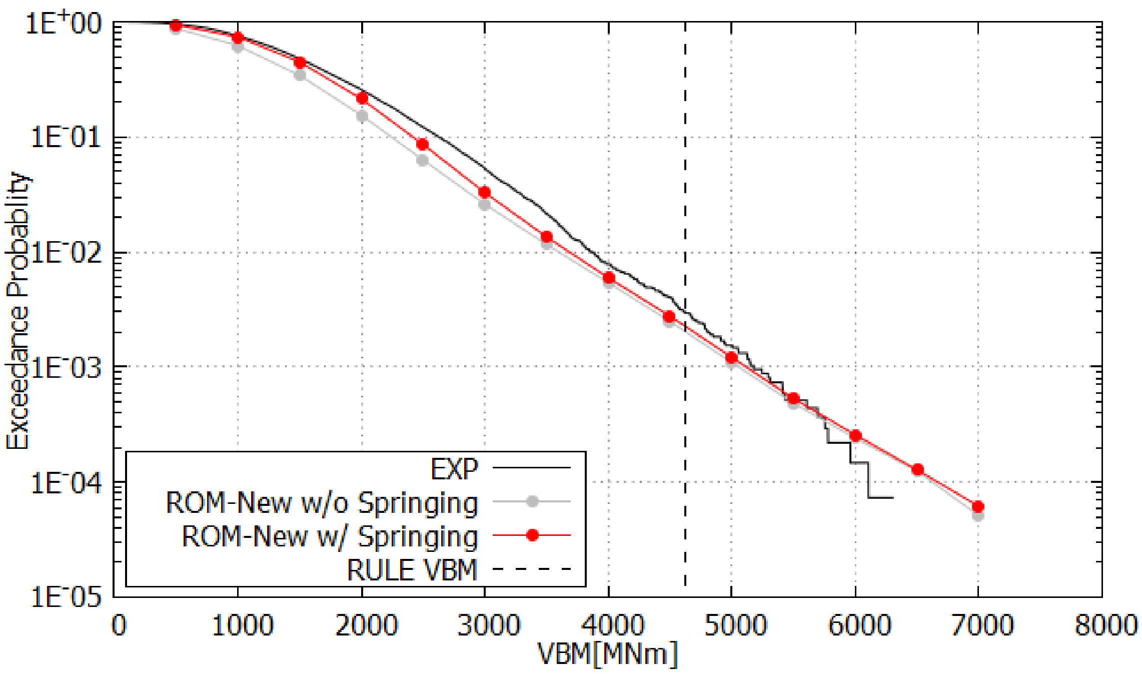

Figure 5.29 Exceedance probabilities obtained from the experiment and ROM with and without springing

5.7 Summary

In this chapter, a method for efficiently estimating the extreme value distribution of VBM based on the coupled CFD-FEM analysis was developed and the validity was confirmed for a post-Panamax containership. First, a ROM is developed based on a physical model to represent the vertical bending moment under the wave and whipping-induced loadings. The CFD-FEM one-way coupling method is considered to be a realistic physical model, which can closely represent the experimental result. The extreme value distributions of the vertical bending moment derived by each ROM were compared against the tank test results. The CFD-FEM coupled analysis was performed under a short-term irregular wave episode, and the obtained vertical bending moment time series were compared with those obtained by the ROM. A comparison of the obtained extreme value distribution from the ROM and that of the experiment shows the extreme values at the high probability were well predicted. However, the extreme values at the low probability level are slightly underestimated.

It was confirmed that the vertical bending moment obtained from the experiment has a springing elastic vibration component superimposed with the wave-induced and whipping-induced elastic vibration components. Then, the springing component was introduced into the ROM. With the new ROM, the extreme values of the vertical bending moment increased at a probability level of 1/10 of the distribution in comparison to the experiment. On the other hand, at the probability level of 1/1000 or 1/10000, there was almost no change in the extreme value distribution due to the effect of springing, indicating that the wave component and the whipping elastic vibration component were dominant. It is necessary to point out that in this case, the springing vibrational amplitude is smaller than the whipping, however, the scenario may change due to the different sea states, with smaller wave heights, where the springing can be more relevant. Although, the current ROM does not need to be tuned again for different wave episodes in the same sea states, the change in the significant wave height and mean wave period may need a slight adjustment. Also, in this work, only a constant low forward speed has been chosen to analyze the current ROM, since the experimental data was not available for the sudden changes in speed. Such parameterization is necessary for developing robust ROM in the future.

6 Collapse Analysis of Hull Girder

In this final chapter, the hull girder collapse behavior is investigated in the case of a 5250 TEU containership using coupling between Computational Fluid Dynamics (CFD) and Finite Element Method (FEM) (section 2.3 & 2.4). The target collapse part is modeled using elasto-plastic material with sufficient fine mesh and the remaining part with an elastic material. Still water load (SWL) has been applied first, which results the containership to bend in hogging direction in calm water condition. Thereafter, a design wave load (DWL) has been applied using CFD, which pushes the structure further towards the ultimate hogging strength. The obtained collapse behaviors from one-way and two-way couplings are discussed in comparison to a pure bending static test.

6.1 Subject Model

The subject ship is a 5250 TEU containership, whose principal particulars are detailed in Table 6.1. This is the same model used by Han et al. [29]. The longitudinal mass distribution of the full-scale model is shown in Figure 6.1. As it is well known that the containership usually stays in the hogging condition in still water, end moments are applied at bow and stern of the hull to achieve the required still water hogging vertical bending moment.

Table 6.1 Details of the model used in the numerical analysis

Properties	Full Scale	Model Scale
Length (L)	280 m	2.8 m
Breadth (B)	39.8 m	0.398 m

Depth (D)	23.6 m	0.236 m
Draft (d)	13 m	0.13 m
Displacement	8.8E7 t	88 kg
Scale		100

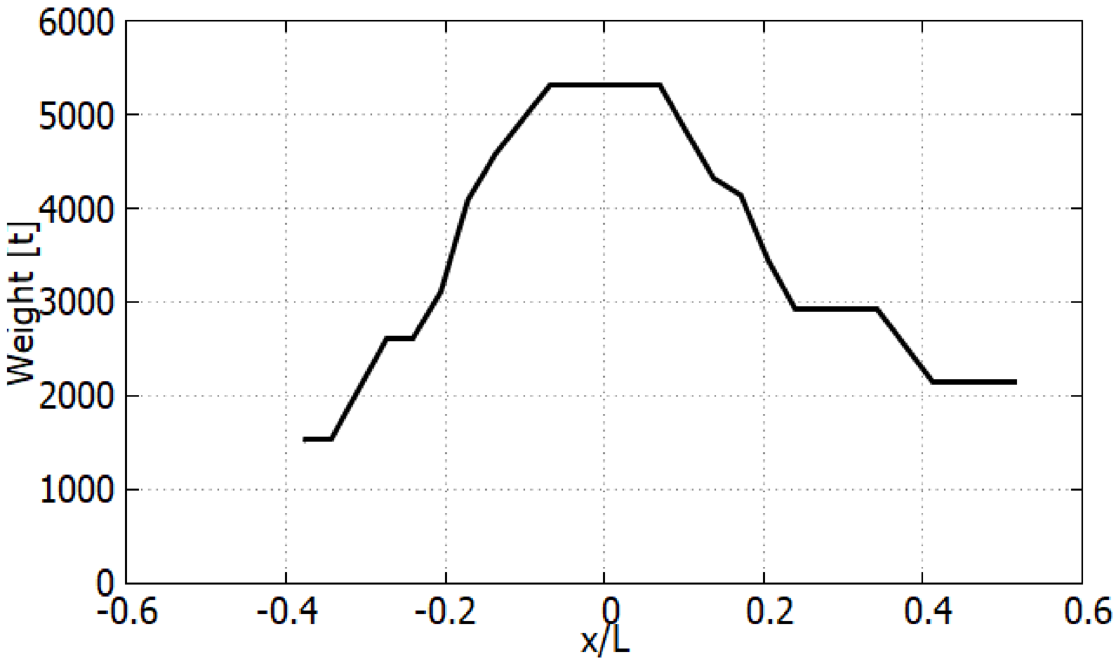

Figure 6.1 Mass distribution of the subject model in full scale

6.2 Design Wave Generator

A maximum probable wave episode (MPWE shown in Figure 6.2) is created using First Order Reliability Method (FORM) with a Reduced Order Model (ROM) (see Section 4.4). The generated design points are used in the CFD solver to create the same wave in model scale. The corresponding CFD meshes at different planes around the free surface are shown in Figure 6.3.

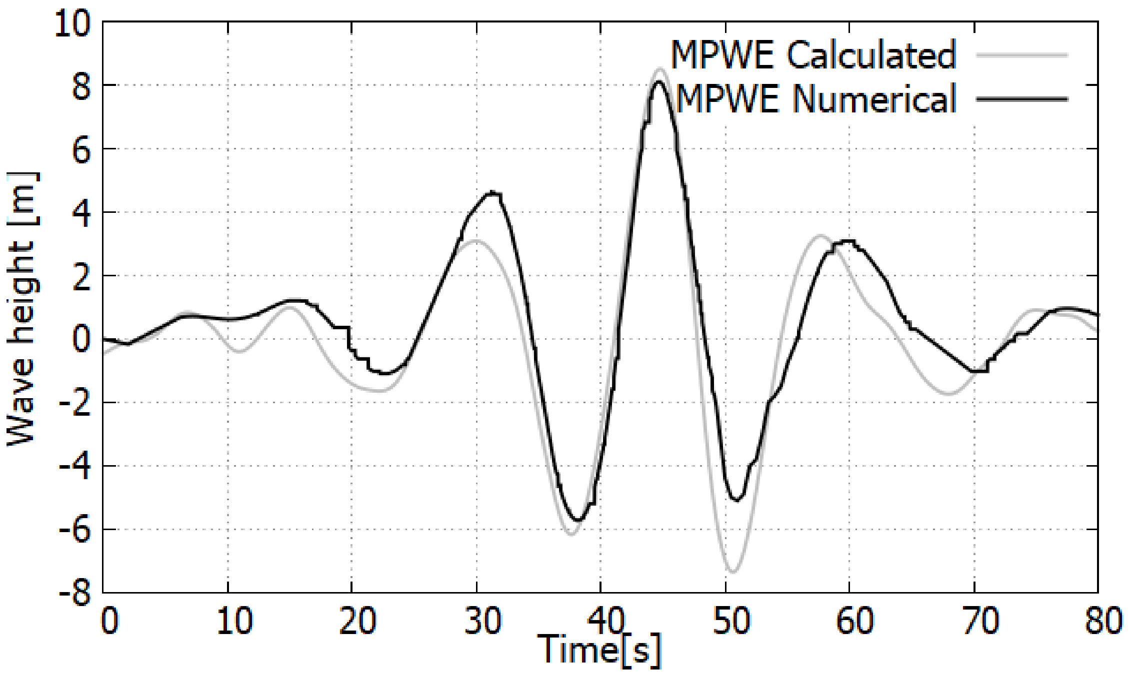

Figure 6.2 Maximum Probable Wave Episode in full scale

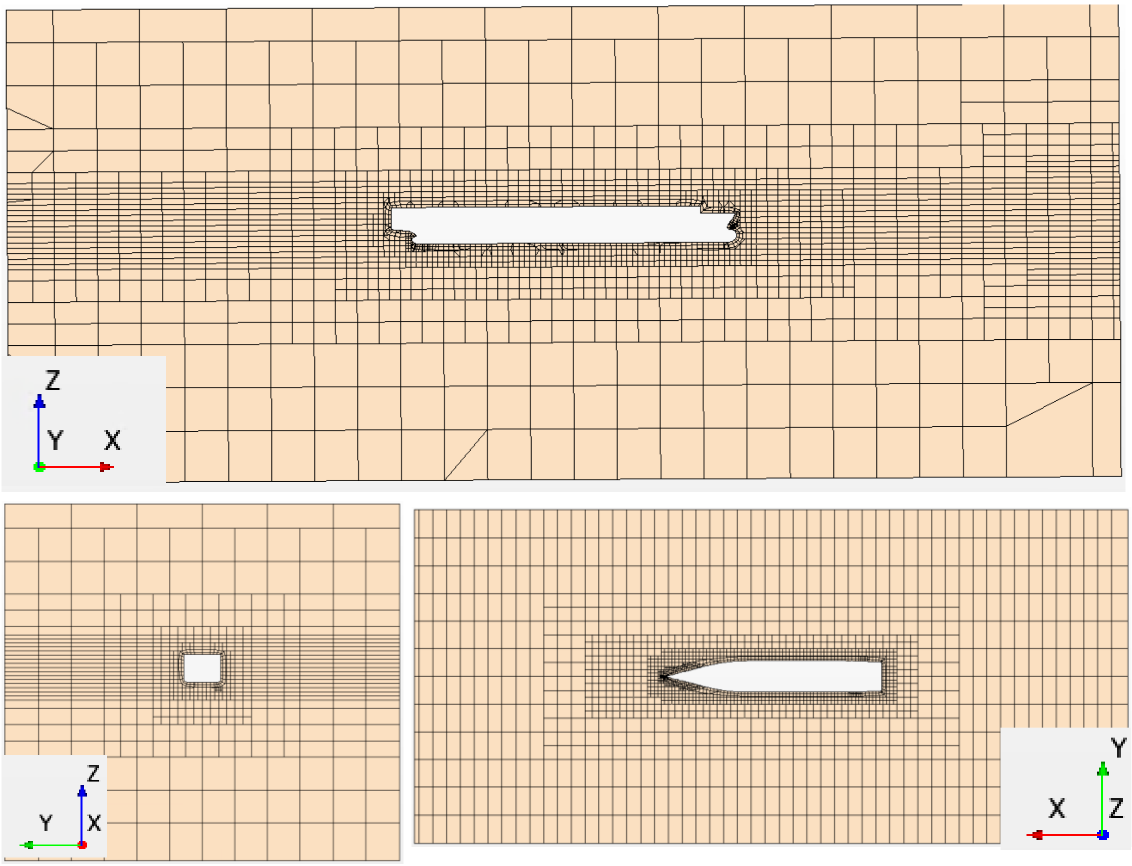

Figure 6.3 Free surface meshes used to capture the MPWE

In the Figure 6.2, *MPWE Calculated* is the wave created using FORM+ROM and *MPWE Numerical* is the same wave generated in CFD numerical tank. Difference maybe because of the free surface mesh quality used in the simulation. However, the combination of still water moment and wave induced moment is adjusted so that the structure collapses in the generated wave. Since this discussion is out of scope of this work, detailed discussion on the usage of FORM and ROM can be found in Pal et al. [16].

6.3 Structural Detailing

The structural domain is modeled in FE software LS-DYNA and shown in Figure 6.4. There are total 9 outer shell segments and a backbone beam. Outer shell segments are connected to the backbone rigidly using rigid beams. To reduce the computational time, only midship is modeled using elasto-plastic shell elements and only half width model is considered for analysis. In Figure 6.4 the target collapse section is identified at midship, whose details are shown in Figure 6.5. There is discontinuation of backbone beam in the targeted collapse part and two ends are connected using rigid beam to the beam node. The symmetric boundary condition is applied at the center cross-section. Surge, heave, and pitch motions are allowed on every node on the hull, except one node is constrained in X direction in backbone to maintain continuity with the fluid model.

Full scale model is considered here for collapse analysis. The material properties of the LS-DYNA model are summarized in Table 6.2. Due to difficulty in convergence in dynamic collapse analysis by implicit method, only explicit method chosen for all the analysis with time step size is equal to 3.77E-06 s. In Figure 6.6, two-node vertical bending mode is shown whose natural frequency is calculated to be 1 Hz.

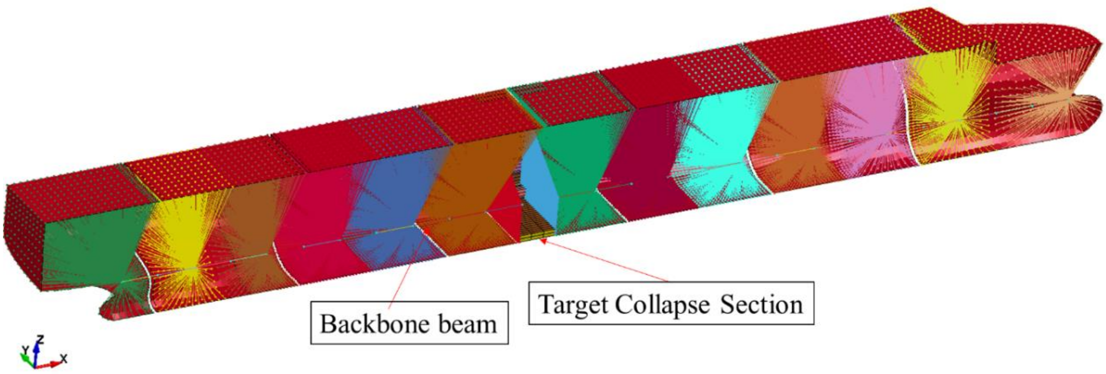

Figure 6.4 Beam-Shell model used in CFD-FEM coupling

Table 6.2 Model properties of the FE model

Young's modulus	2.06E+05 [MPa]
Poisson ration	0.3
Cross-sectional area	1.23E+06 [mm4]
Area moment of inertia	5.948E+14 [mm4]
Shell elements	Highues-Liu type
Beam Elements	Belytschko-Schwer
Structural damping	Rayleigh type (α = 0.3, β =0.01)
*MATERIAL (Shell)	Plastic Kinematic
*MATERIAL (Beam)	Elastic

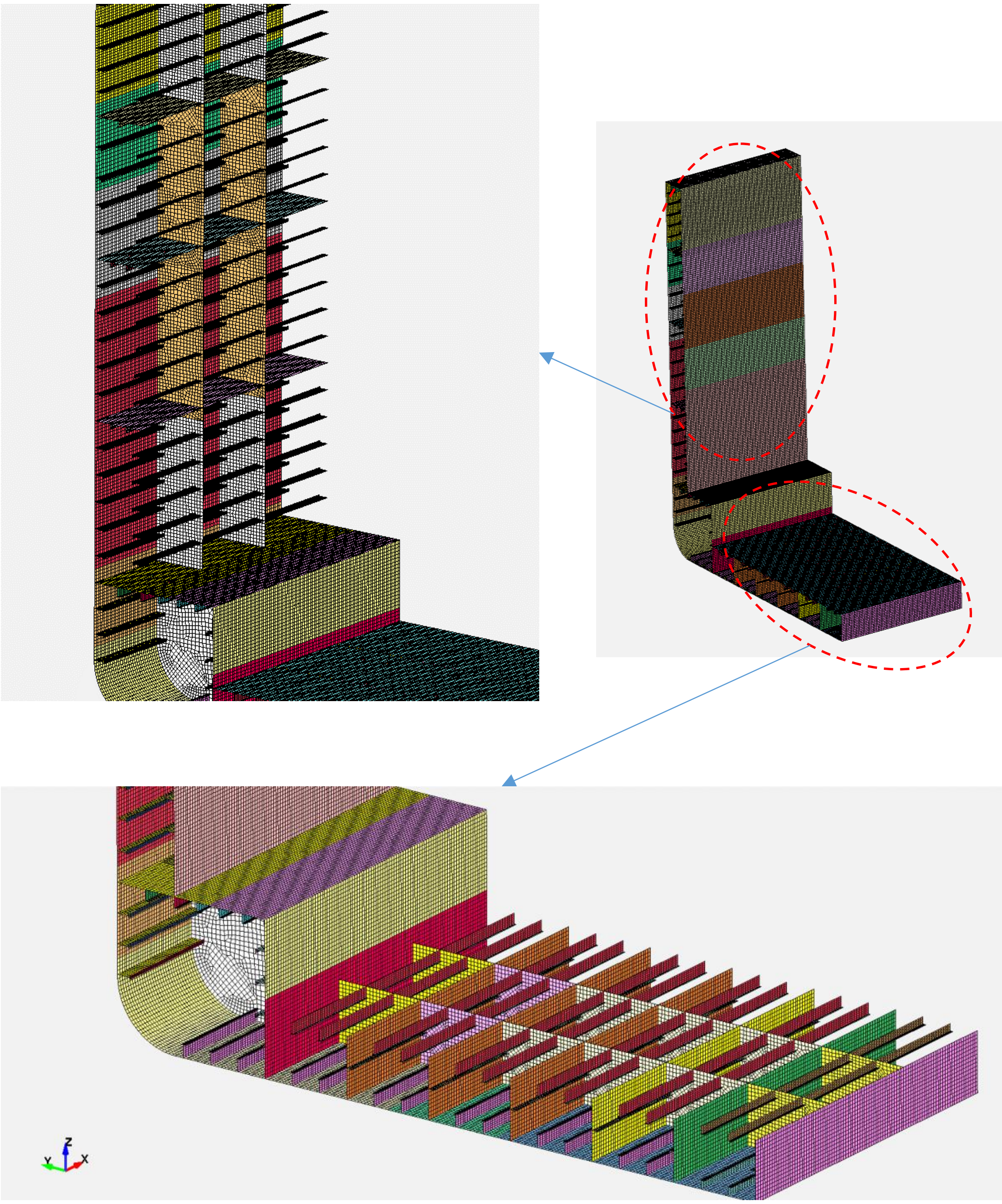

Figure 6.5 Structural details of the targeted mid-ship used in Beam-Shell model

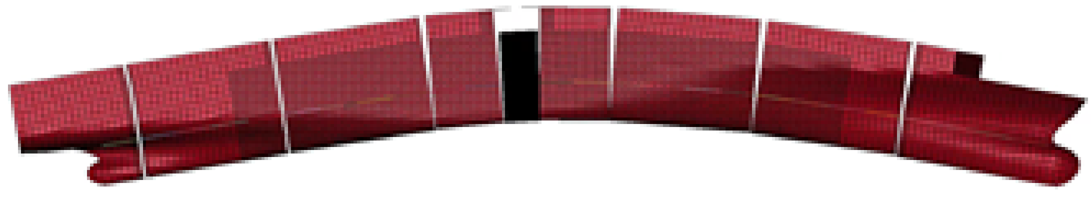

Figure 6.6 Two-node bending of the subject ship (1.1 Hz full scale)

6.4 Static Strength Analysis

First, a static bending collapse analysis has been performed to understand the failure behavior using beam shell model mentioned in (Figure 6.5). A moment is applied at the extreme ends of the hull towards hogging direction to implement this test. The moment is slowly increased till the targeted section collapses as shown in Figure 6.7. For this analysis, only dead weight has been applied (see Figure 6.1). The bending moment - curvature relationship of the static collapse analysis is shown in Figure 6.8 and compared with the Han et al. [29].

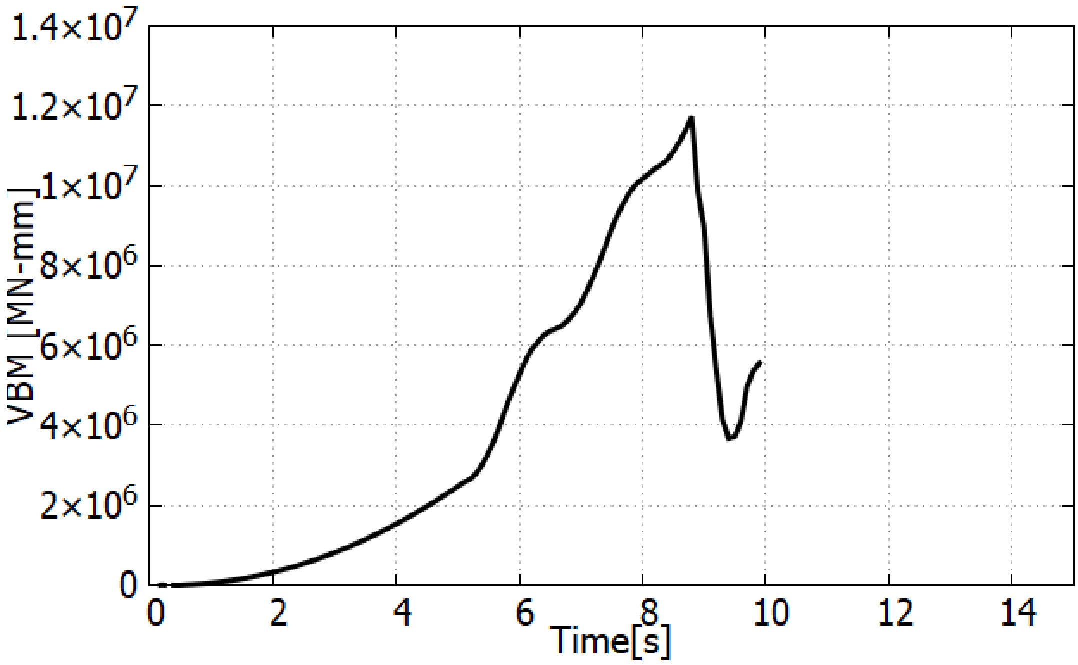

Figure 6.7 Moment time history at the targeted section due to applied moment

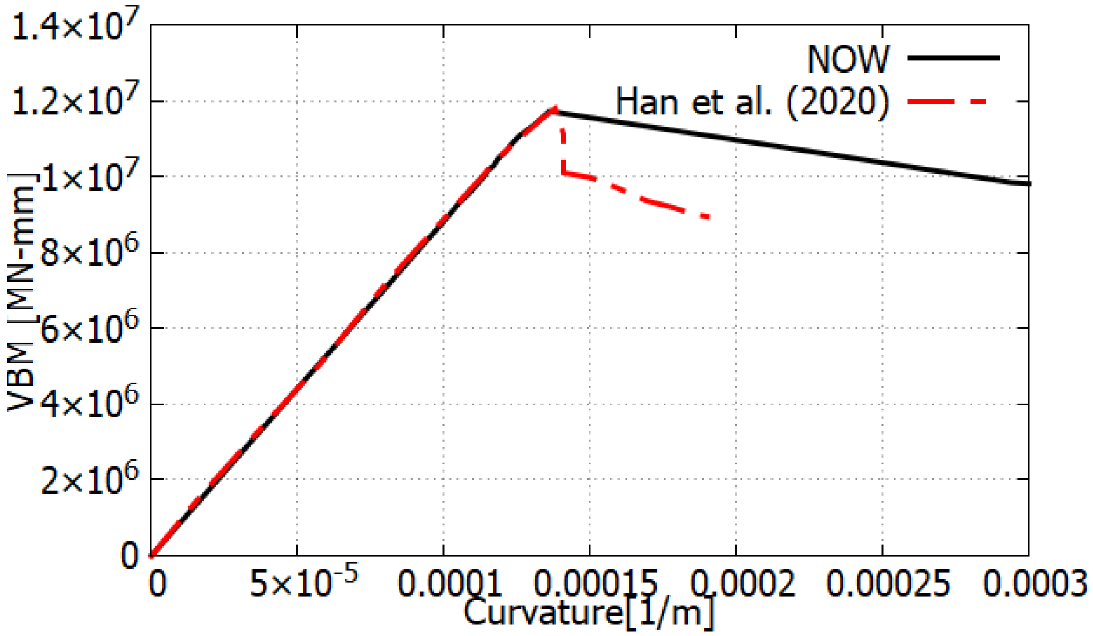

Figure 6.8 Moment-curvature relationship at the targeted section

The curvature is calculated by dividing the difference of Y rotational angle of two connecting node of the collapse section with length of the collapse part. From the figure it can be stated that the hogging strength of the targeted collapse section is 1.1815E+07 MN-mm which is very similar with Han et al. [29]. And also, it can be seen that, the stiffness of these two models are same. However, it can be pointed out from moment-curvature relationship that the post collapse behavior is different in both cases. This is maybe due to absence of supporting translational spring and viscous damper at the base of the hull used by Han et al. [29]. As the spring and damper can slightly contribute to the relative motion of connection points of collapse part, hence can contribute to the collapse of the section. In the present analysis, the gravity force is balanced with hydrostatic force automatically and use of springs and dampers are avoided. Plastic strain is initiated at both sides of the frame at the outer plate of the keel. Then it concentrates in one side and reaches the collapse (Figure 6.9).

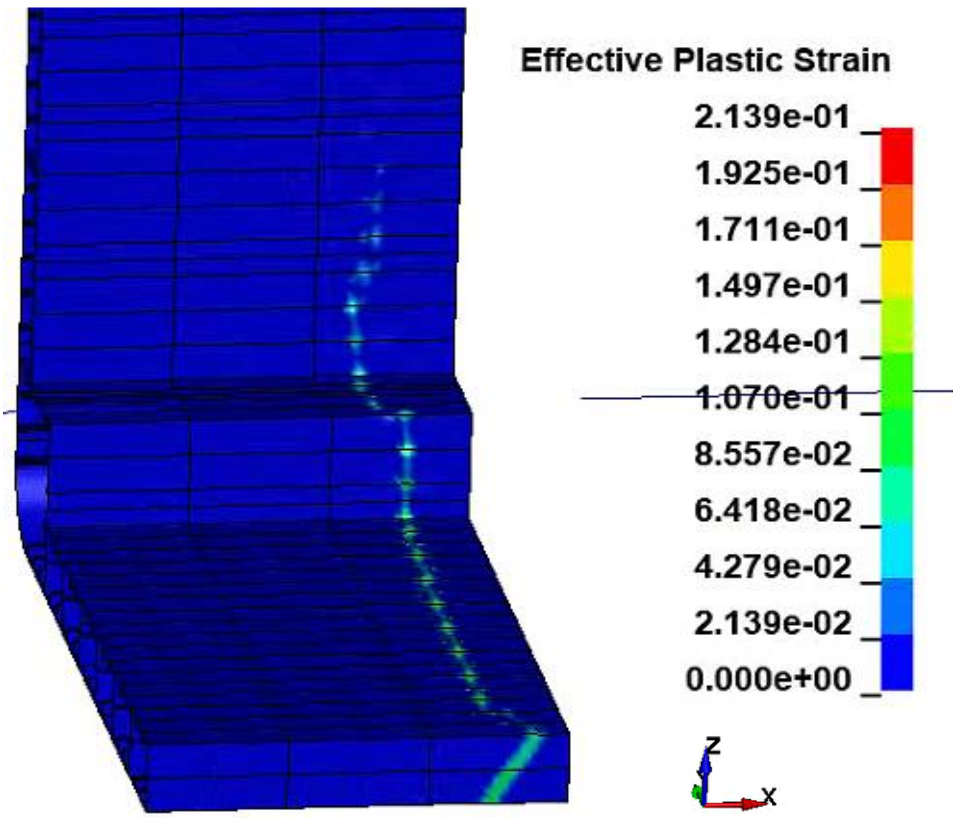

Figure 6.9 Plastic strain distribution at the ultimate strength

6.5 Collapse Comparison Between One-way and Two-way Coupling

As discussed in section 2.3, in one-way coupling analysis first fluid pressures on the hull surface due to the generated design wave are extracted. Then, the obtained pressures are mapped into defined panels of the FE model. These mapped pressures can be used directly to perform the FE analysis or can be converted in to segment forces to carry out FE analysis. While the mapped pressure can be used on the outer skin of the beam-shell model (Figure 6.4), on the other hand segment forces can be applied in backbone nodes of the FE model (Figure 6.4) to conduct FE analysis. In this section, the direct mapped pressure in shell centroid of FE panels, are used to conduct one-way and two-way coupling analysis. The method of load application is kept same between one-way and two-way coupling analyses to avoid any significant difference while comparing the results between two methods.

In Figure 6.10, vertical bending moment time histories are plotted from one-way and two-way coupling analysis for the generated MPWE (Figure 6.2). The offset from the x-axis represents the applied still water vertical bending moment in FE solver. Along with it the wave force is applied by extracting the pressure profiles from CFD solver. Static strength derived from section 6.4 is also plotted herewith. It can be seen that in both analysis the structure has reached its ultimate strength around 42.1 s. From the MPWE and VBM time series it can be seen that the wave peak corresponds to 30 s, causes the structure to go almost near failure. However, as the wave load reduces the structure returned back to its elastic region with some plastic deformation. Also, in Figure 6.10 the VBM time series due to one-way coupling analysis considering the structure as a 1D elastic beam is presented. In all these models the 2-node vertical dry natural frequency is kept 1.1 Hz. It can be seen that the slamming induced whipping vibrations are somewhat prominent in this case, however the effect on the ultimate strength due to increased whipping vibrations is still need to be investigated by lowering the structural natural frequency [36]. In Figure 6.11-6.13, moment versus curvature is plotted for one-way and two-way coupling analysis. In Figure 6.12-6.13, it can be confirmed that the plastic deformation occurred around 30 s and the hull continue to operate after that until it came across the highest peak at round 42.1 s. The moment-curvature relationship for 0-30s is plotted with black line and rest is plotted with red line in case of one-way and two-way coupling analysis. From the Figure 6.11-6.12 it can also be noticed that the two-way moment-curvature plot is not straight forward like one-way. In case of two-way a slight difference between inertia and total external force causes the structure to drift. However, as we remove the rigid body motion from the FE analysis at every inner iteration, and only import deformation to morph the rigid structure in CFD solver, the simulation does not get affected by this. Also, the current analysis is done with only two inner iterations (i.e. prediction and correction in Figure 2.9), there might be accumulation of small imbalance force as the time progresses. In the future analysis, a greater number of inner iterations between CFD-FEM will be considered to see its effect on the calculation.

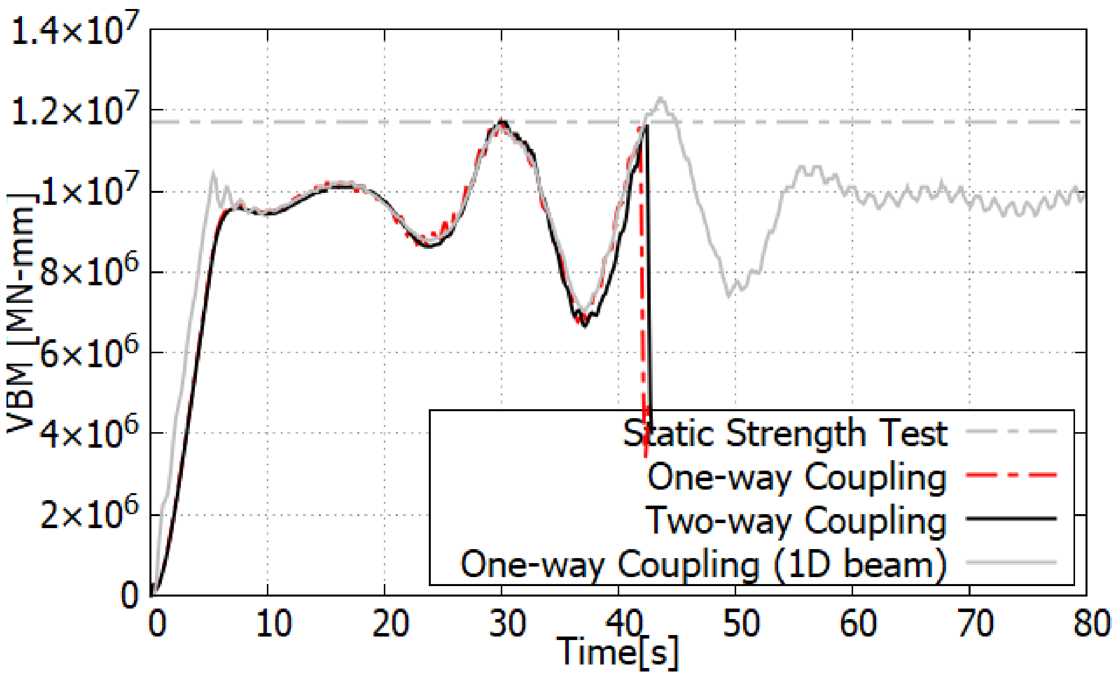

Figure 6.10 VBM time series at midship in case of a total failure condition

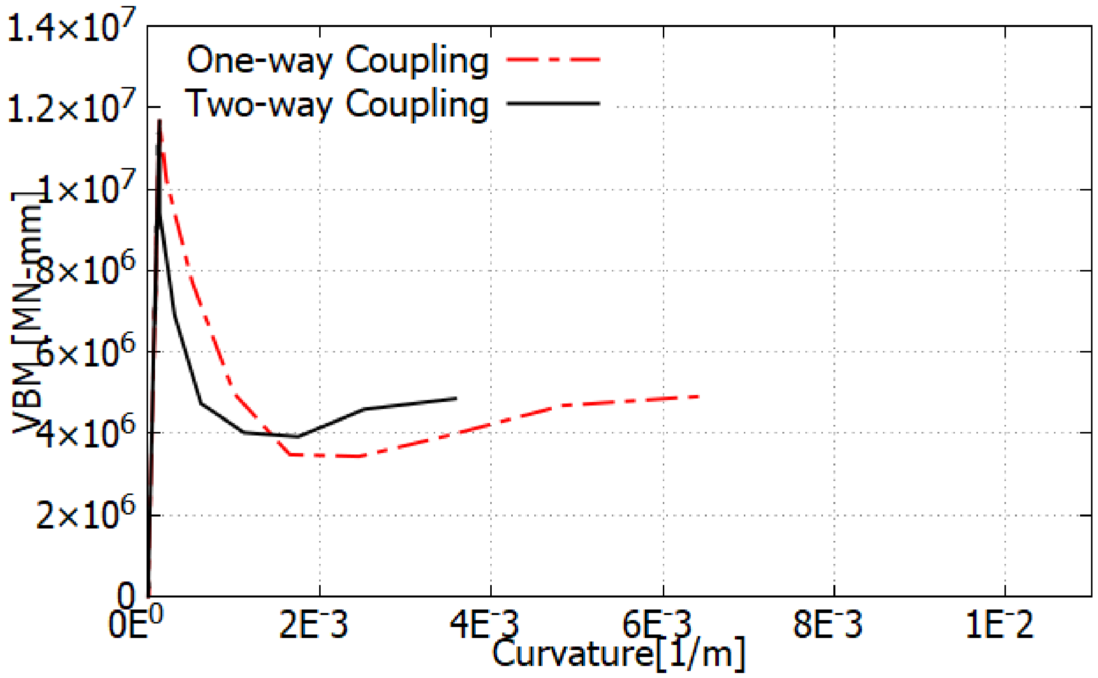

Figure 6.11 Moment-curvature relationship at the targeted section in case of a total failure condition

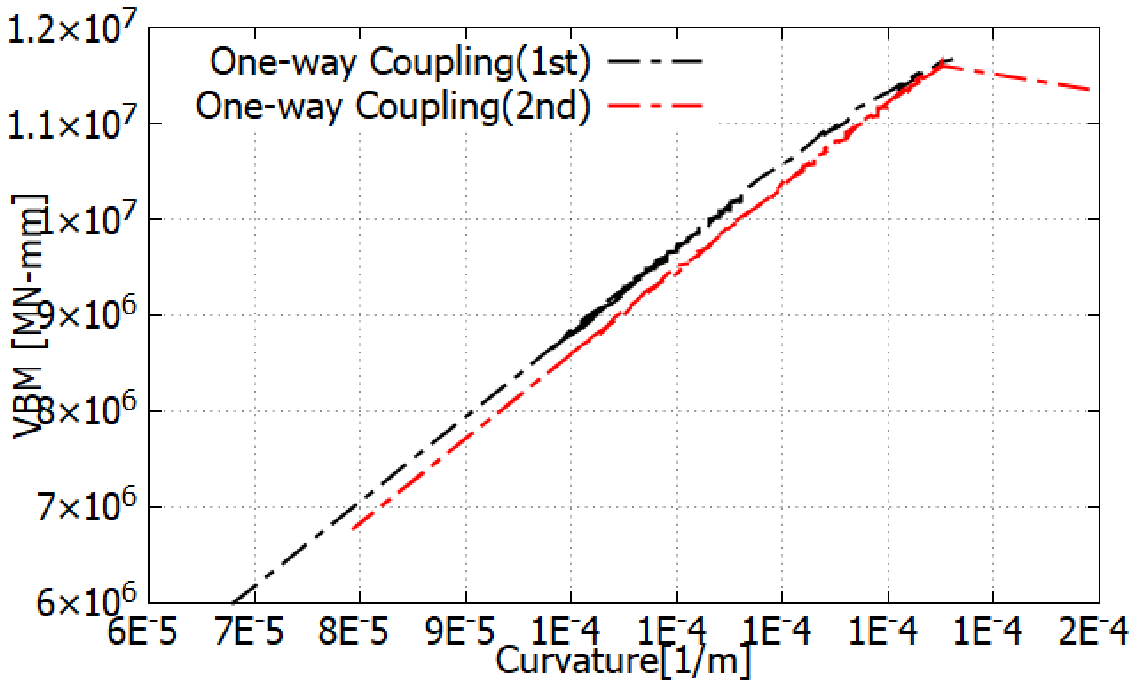

Figure 6.12 Zoomed moment-curvature plot near ultimate strength for one-way coupling

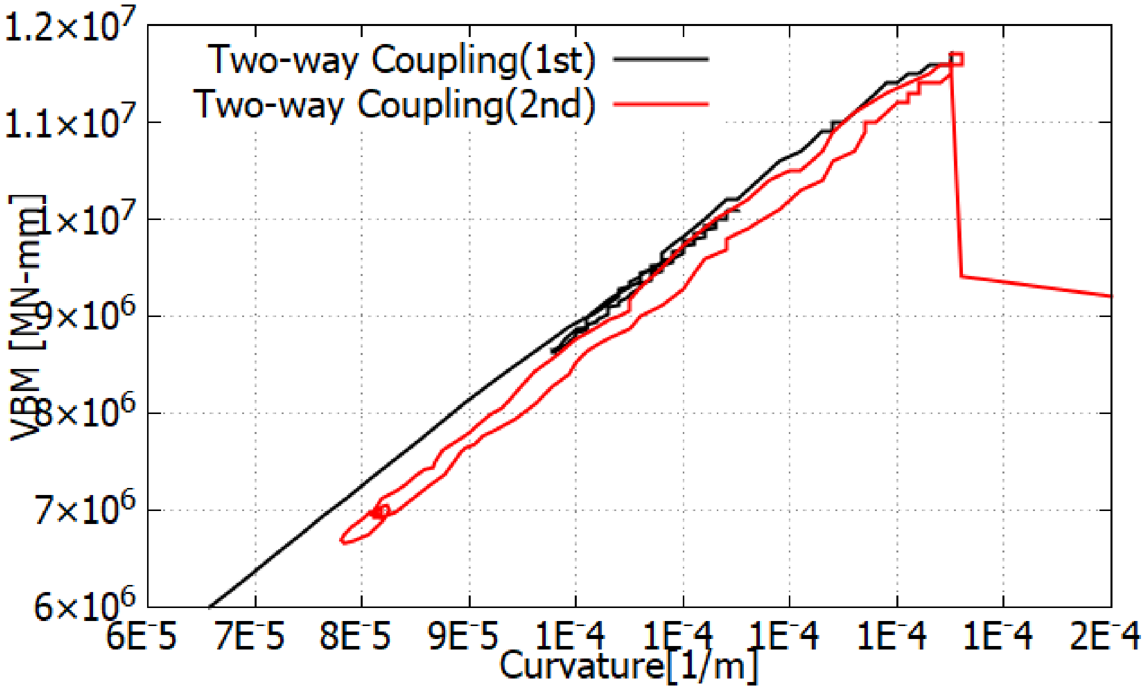

Figure 6.13 Zoomed moment-curvature plot near ultimate strength for two-way coupling

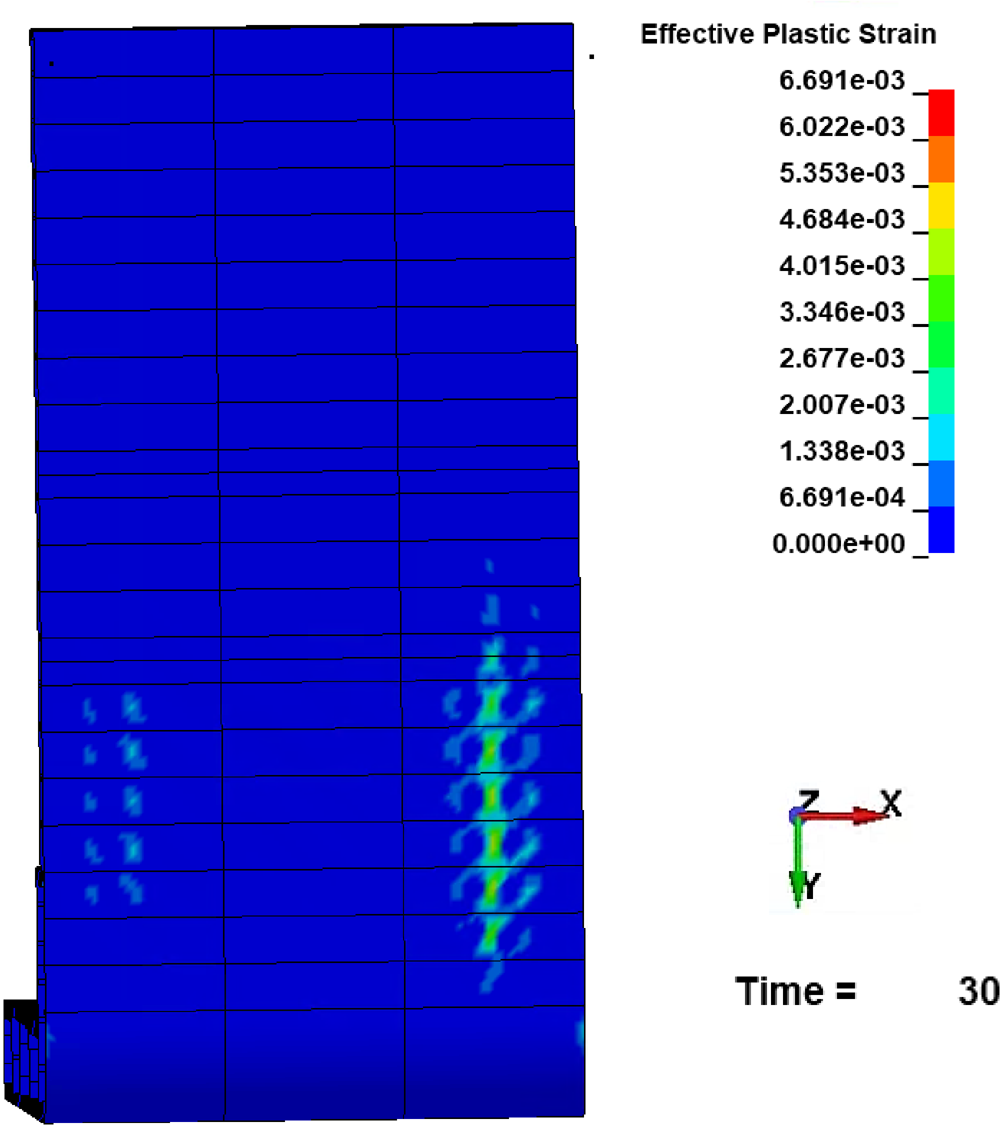

Figure 6.14 Plastic strain distribution at around 30 s in one-way coupling

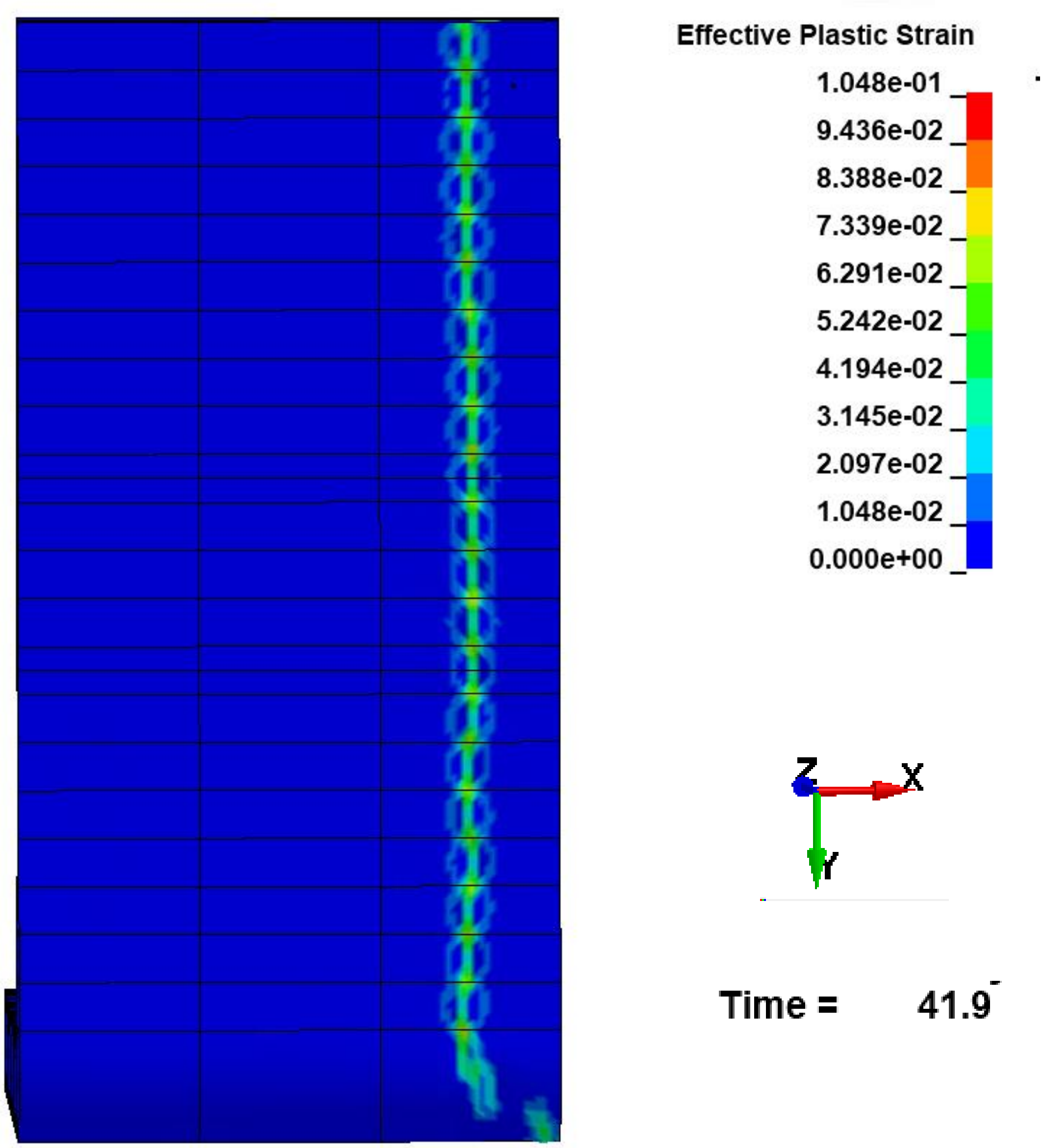

Figure 6.15 Plastic strain distribution at around 42 s in one-way coupling

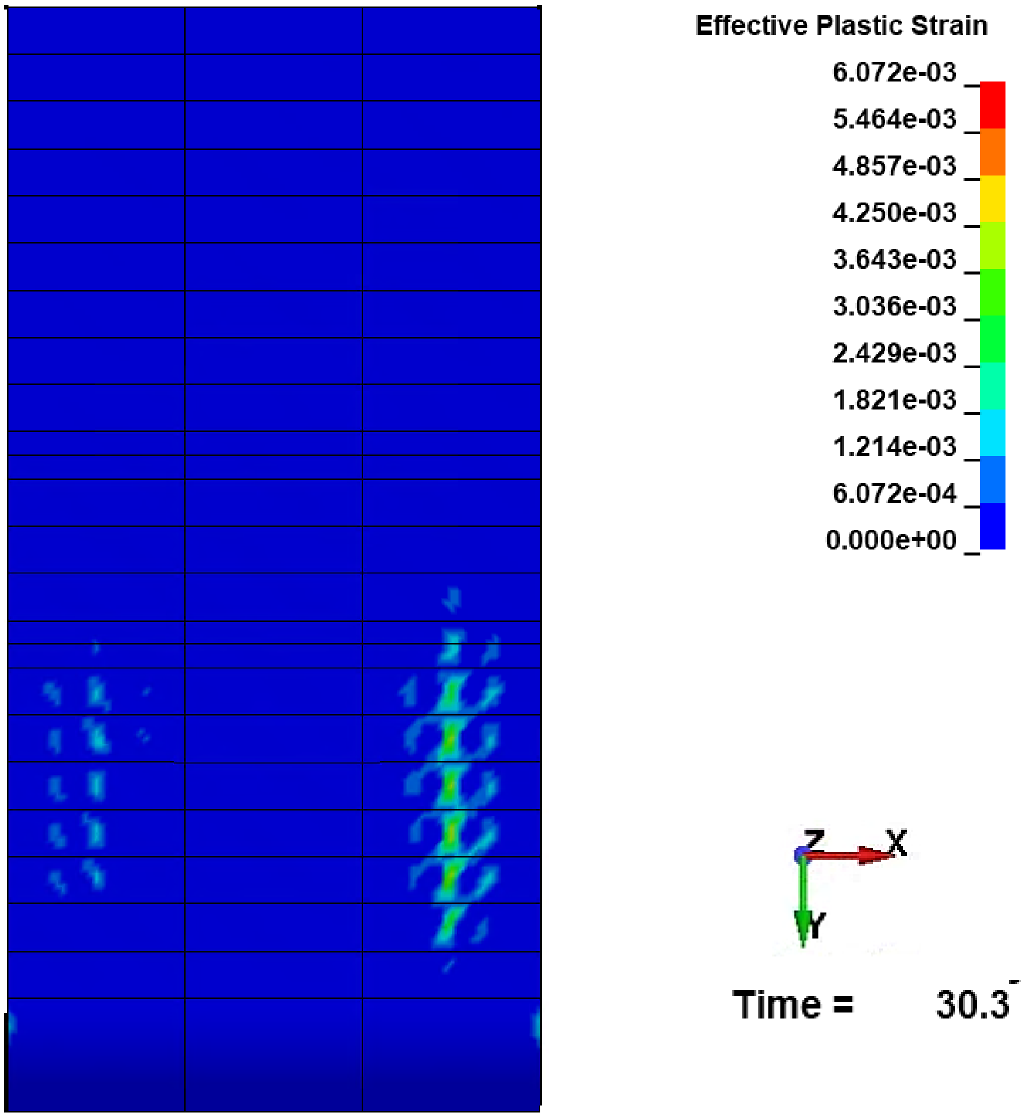

Figure 6.16 Plastic strain distribution at around 30 s in two-way coupling

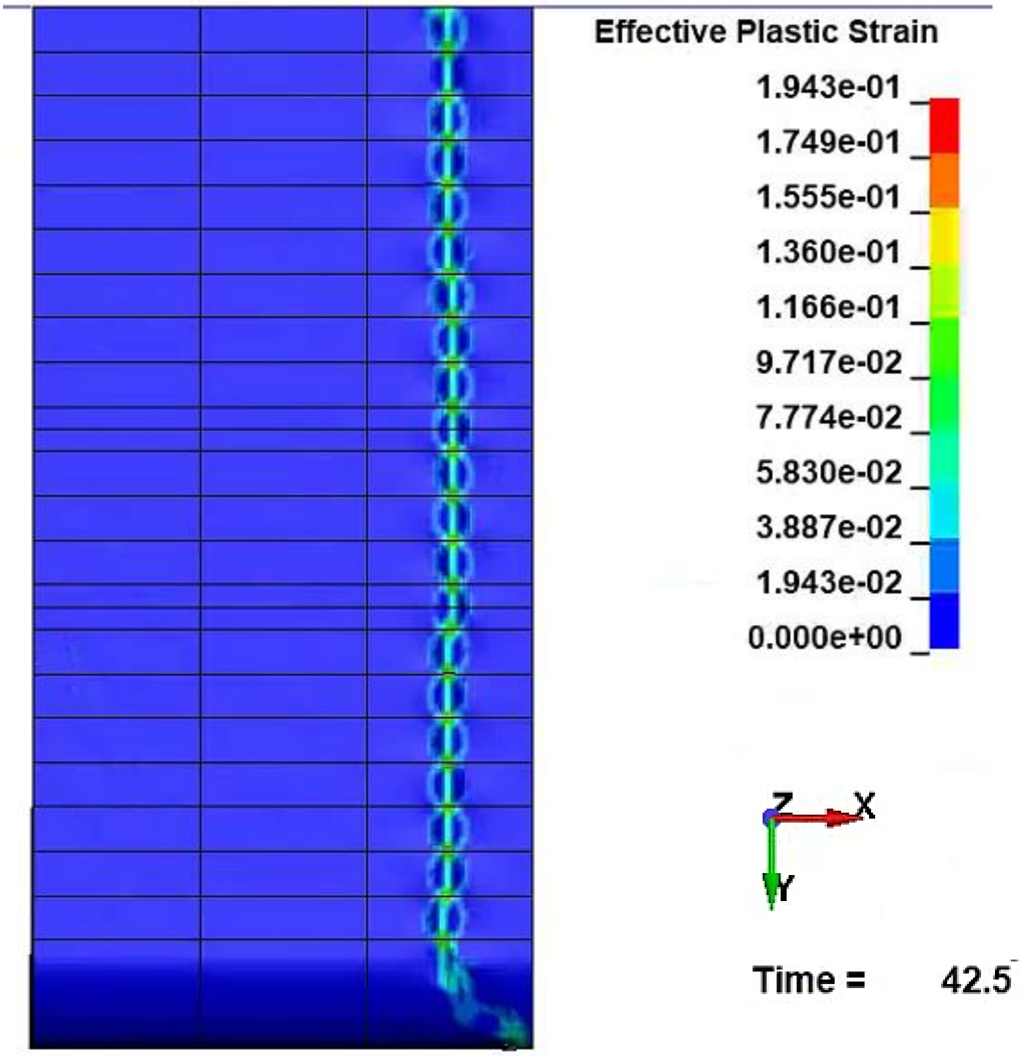

Figure 6.17 Plastic strain distribution at around 42 s in two-way coupling

From Figure 6.14-6.17, plastic strain distribution at the outer bottom plate of the targeted collapse section is shown for one-way and two-way couplings respectively. It can be seen that although the positions of plastic deformations are similar between one-way and two-way couplings, the magnitude of the deformation is different. In both cases first, plastic strain was developed at both sides of the frame at around 29.9 s, which accentuates more on the right side of the collapse part which leads to the ultimate collapse of the section at around 42.3 s.

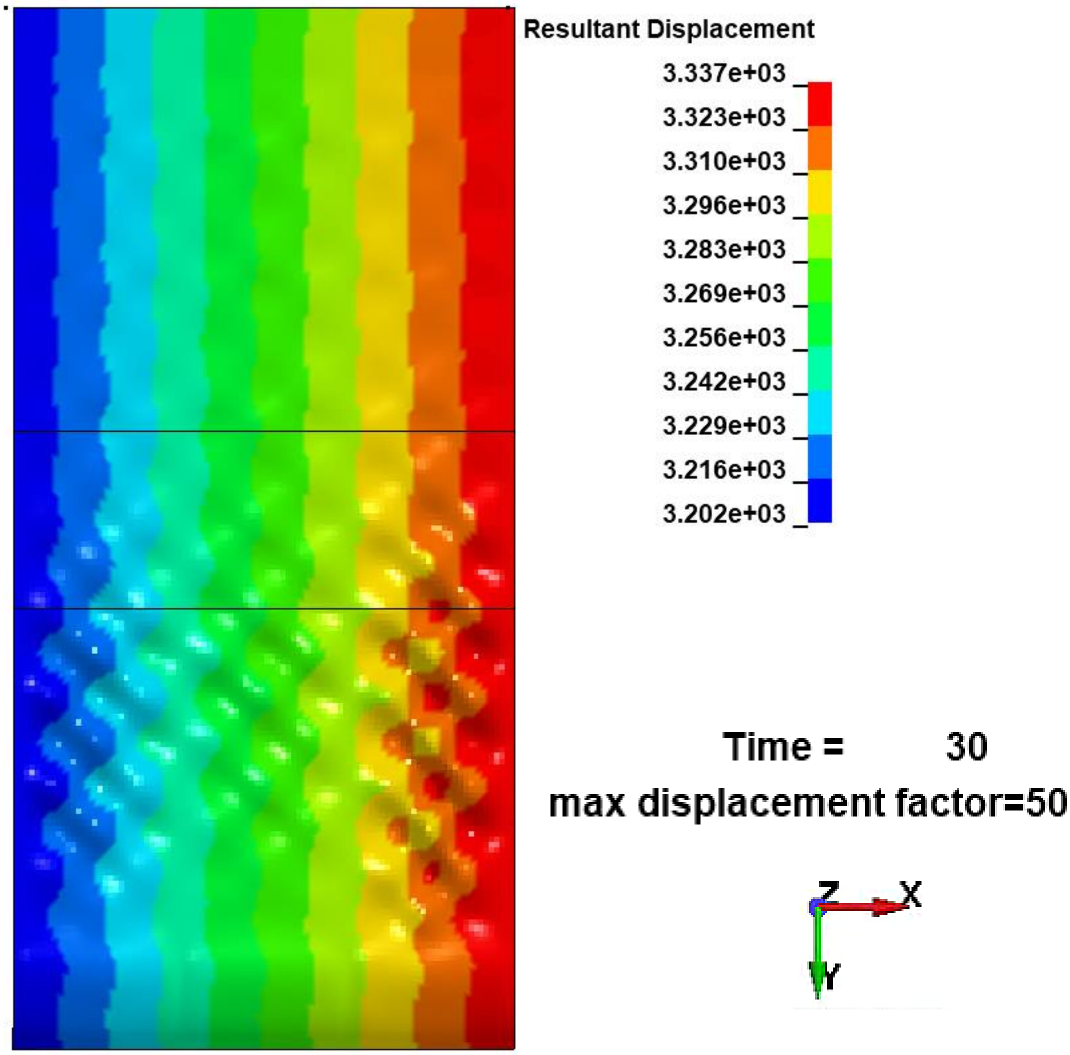

Figure 6.18 Resultant displacement distribution at around 30 s in one-way coupling

The resultant displacement at the outer bottom plate of the collapse section by one-way and two-way coupling analyses are compared at around 30 s in Figure 6.18-6.19. It can be seen that the local deformation of the plate is almost similar between these cases except the rigid body motions. This is due to the difference between global motions of the hull between one-way and two-way coupling analyses.

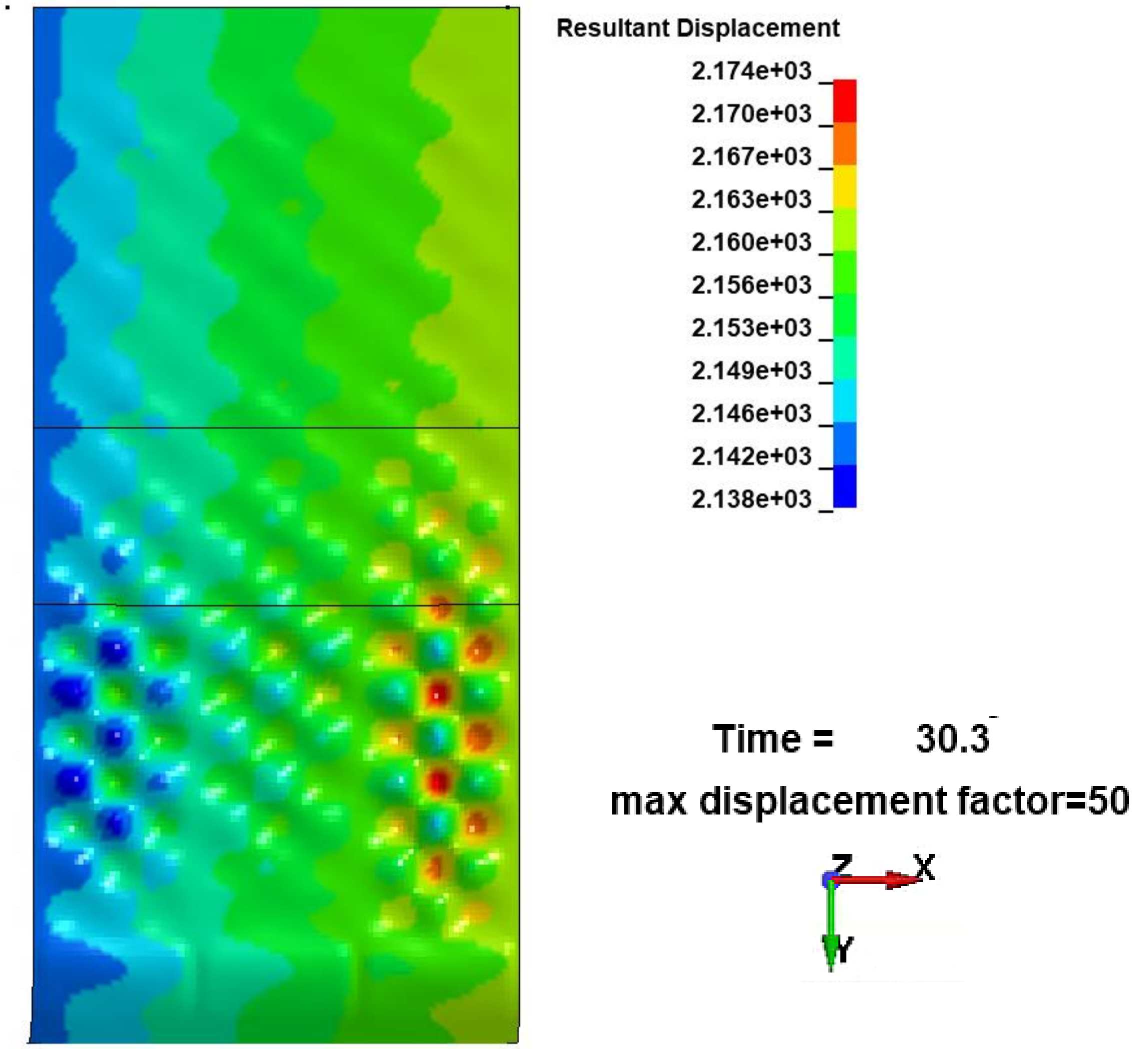

Figure 6.19 Resultant displacement distribution at around 30 s in two-way coupling

6.5.1 Comparison of Deformation Contour between Different Forms of External Load

In this section, the deformation contour at the outer bottom plate is investigated using one-way coupling for different forms of external loads. In the previous section the external load was chosen as direct pressure on the outer skin of the beam-shell FE model. However, it is also interesting to see what is the difference if we use the segment load time series at the nodes of the backbone beam. The goal here is to observe the change in local deformation profile when easiest form of load is applied.

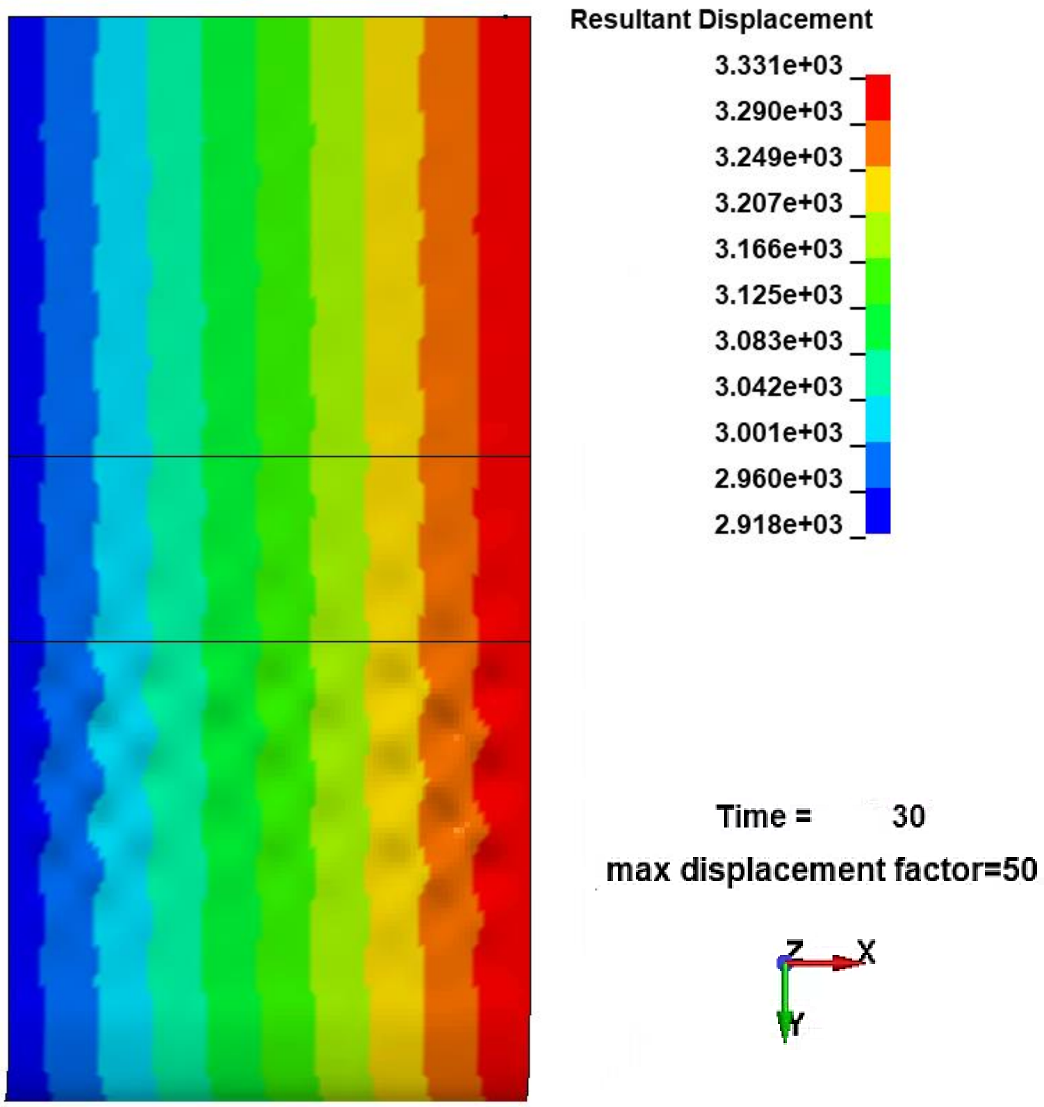

Figure 6.20 Resultant displacement distribution at around 30 s in one-way coupling by just applying the segment load

In Figure 6.20 the resultant displacement at the outer bottom plate of the collapse section is plotted. It can be seen that, the deformation contour compared to the direct pressure case (Figure 6.18) is somewhat similar, however, it is more prominent in case of a direct pressure load case. This is because of the application of direct pressure locally, which is missing in the case of segment load case.

6.5.2 Local Collapse Behavior

To understand the behavior of the collapse at the local scale (see Figure 6.21), average stress - average strain curve in the longitudinal direction is plotted for local stiffener using one-way and two-way coupling analysis in Figure 6.22. This is the same analysis as of Figure 6.10. The yield strength of the material is 315 MPa. It can be seen that the local stress-strain plots between one-way and two-way couplings are different although the failure stress is similar in both these methods. This is maybe due to slight difference in global motion of the hull. It can be also commented that local collapse behavior by the two-way coupling method exhibit almost similar nature to the global one.

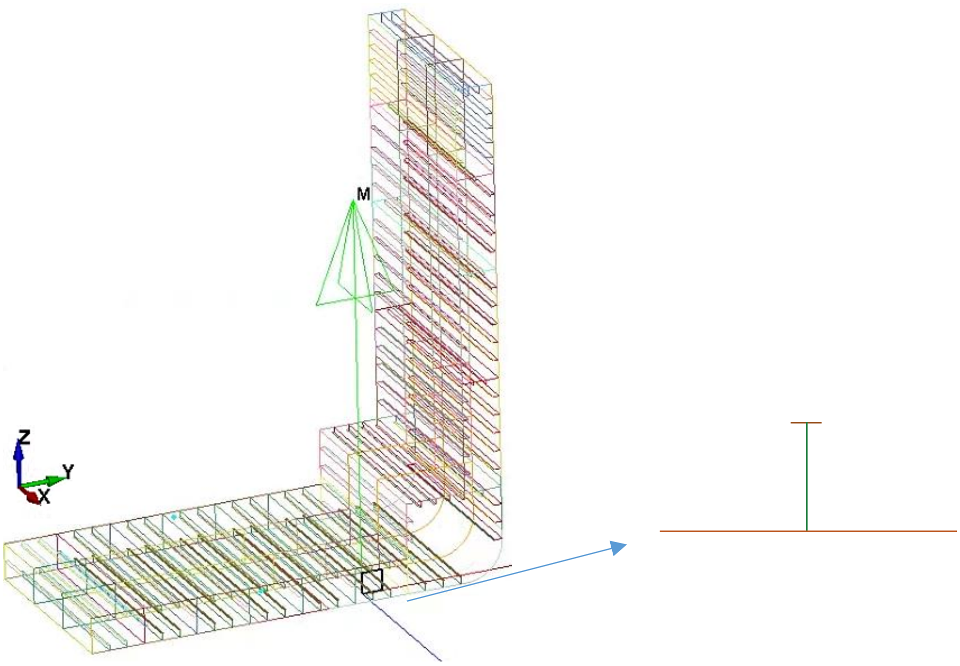

Figure 6.21 Highlighted cross-section for checking the local collapse behavior

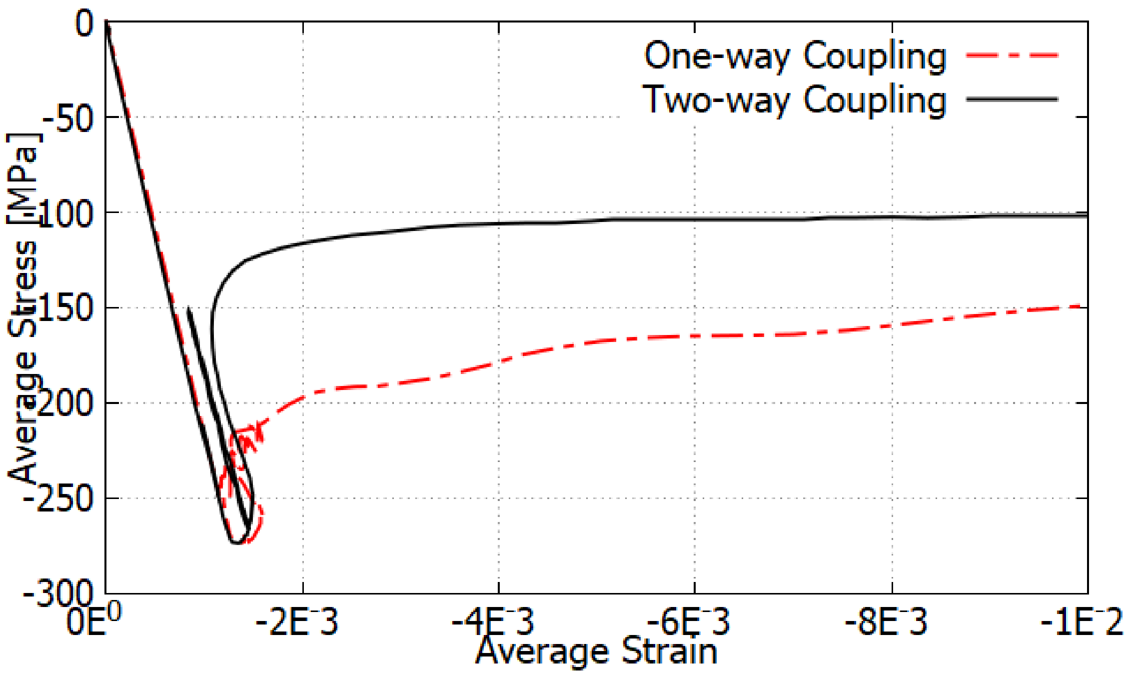

Figure 6.22 Average stress versus average strain plot for the bottom element in Figure 6.21 (Small strain region).

6.6 Summary

In this chapter, the hull girder collapse analysis under extreme waves is investigated using direct CFD and FEM coupling. Two kinds of analysis are considered, namely one-way and two-way coupling. In both these analyses, loads are applied as a form of direct pressure locally at each outer shell of the hull. The collapse behavior is compared between two methods using vertical bending moment time histories, moment-curvature plots, plastic strain distribution profiles, and resultant displacement profiles. It can be commented that the collapse behavior predicted by both these analyses are similar. It is pointed out that the local deformation contour is almost similar between one-way and two-way coupling analyses. It is noted that the deformation plot was more prominent when direct pressure is applied instead of segment load. Later, to confirm the collapse behavior in the local regions, one element is chosen at the transverse floor of a double bottom to look at average stress-average strain curve. From which it can be commented that local stress – strain plots between one-way and two-way couplings are different although failure stress is similar in both these methods. In this two-way coupling analysis only two iterations per time-step are performed due to computational constraint. However, in the future it is important to increase the number of iterations and compare the effects.

7 Conclusions and Future Works

7.1 Conclusions

In this thesis an in-house one-way and two-way coupling methods between CFD and FEM are developed to investigate the effect of wave-induced vibrations on the hull girder strength of ships. First, one-way and two-way coupling methods are detailed with different CFD and FE models used in this thesis. Later, the coupling methods are used to validate the rigid body motions of a flexible barge against experimental results. The coupled CFD-FEA method is further applied to investigate the springing by comparing with experimental results. Later, it is also used to develop the reduced order model, which in turn used for calculating the extreme value distribution of VBM. Lastly, the effect of wave induced load on the collapse behavior of a hull girder is investigated using one-way and two-way CFD-FEA coupling schemes. Based on the current observations, derived conclusions are listed below:

- Derived results using one-way and two-way coupling schemes are agreed well with tank test results for the normal wave component.
- The wave-induced vibration components derived from the one-way coupling method, predicts well compare to model test results within engineering accuracy. The added-mass effect is introduced in one-way coupling scheme by increasing the mass of the structure artificially. It is adjusted so that it matches the two-node wet natural frequency of the structure form the experimental and numerical hammering test. High-frequency vibrations in the VBM time series are compared well with experimental results.

- The ROM is developed with the help of CFD-FEA coupling analysis. Along with wave-induced, whipping-induced components of VBM, springing ROM is introduced based on the experimental data. The current ROM is able to predict well the extreme value distribution of VBM in comparison with tank test results. However, the extreme values at the lower probability levels are slightly underestimated.
- With the introduction of the springing ROM, the extreme values of the VBM increased at the probability level of 1/10. On the other hand, there was almost no change in the extreme value distribution due to the effect of springing, indicating that the wave component and the whipping elastic vibration component were dominant at the lower probability regions.
- The effect of wave-induced load on the collapse analysis is investigated by comparing the one-way and two-way coupling results. The collapse behavior is compared for the VBM time series, moment-curvature plots, plastic strain distributions, and resultant displacements at the target collapse part of the containership. It can be commented that, the global collapse behaviors obtained using one-way and two-way coupling schemes are similar.
- The resultant displacement profiles at the outer bottom plate of the collapse part are compared between one-way and two-way couplings. It can be commented that the deformation plot from both one-way and two-way coupling analyses contains distinct local buckling.
- The deformation plot is more prominent when the direct pressure is used as a form of external load in comparison to the segment load case.

7.2 Future Scopes

The possible scopes for the further development of the current work can be done focused on:

- The development of the current ROM towards the inclusion of the complicated consecutive bow-stern slamming is needed. This can improve the probability of exceedance curve more compare to the tank test results.
- The springing reduced order model is still immature and needs further development.
- The current approach should be extended from surge, heave, and pitch towards inclusion of other degrees of freedom. The other wave heading angles should also be considered in this development.
- The two-way coupling code should be improved further to reduce the computational cost involved.
- More extensive investigations on the collapse analysis using the current CFD-FEA schemes are required.
- The collapse behavior study using increased frame length is required in comparison to the present investigations.

References

[1] Marine Accident Investigation Branch, 2008. Investigation report MSC Napoli. Report No 9/2008, UK. URL https://assets.publishing.service.gov.uk/media/547c703ced915d4c0d000087/NapoliReport.pdf

[2] Bahamas Maritime Authority, 2015. Report of the investigation into the sinking of the "MOL Comfort" in the Indian Ocean. URL https://www.bahamasmaritime.com/wp-content/uploads/2020/10/BMA-Investigation-Report-Loss-of-the-MOL-Comfort.pdf

[3] Bahamas Maritime Authority, 2004. Report of the investigation into the loss of the Bahamian registered tanker "Prestige" off the northwest coast of Spain on 19th November 2002. URL https://www.bahamasmaritime.com/wp-content/uploads/2020/10/BMA-Investigation-Report-Hull-failure-and-loss-of-the-Prestige.pdf

[4] Derbanne, Q., Malenica, Š., Tuitman, J.T., Bigot, F., Chen, X.B., 2010. Validation of the global hydroelastic model for springing & whipping of ships. In: Proceedings of PRADS, pp. 331-340. http://resolver.tudelft.nl/uuid:26c07a9b-29be-4a24-8356-742176e5baa0

[5] Ćorak, M., Parunov, J., Guedes Soares, C., 2015. Long-term prediction of combined wave and whipping bending moments of container ships. Ships and offshore structures. 10(1), pp.4-19. https://doi.org/10.1080/17445302.2013.833022

[6] Riesner, M., el Moctar, O., 2021. A numerical method to compute global resonant vibrations of ships at forward speed in oblique waves. Applied Ocean Research. 108, 102520. https://doi.org/10.1016/j.apor.2020.102520

[7] Seng, S, Jensen, JJ, Malenica, S, 2014. Global hydroelastic model for springing and whipping based on a free surface CFD code (OpenFOAM). International Journal of Naval Architecture and Ocean Engineering. 6(4),1024-1040. https://doi.org/10.2478/IJNAOE-2013-0229

[8] Lakshmynarayanana, P. A., Temarel, P., 2019. Application of CFD and FEA coupling to predict dynamic behaviour of a flexible barge in regular head waves. Marine Structures. 65, 308-325. https://doi.org/10.1016/j.marstruc.2019.02.006

[9] Jiao, J., Huang, S., Wang, S., Soares, C. G., 2021. A CFD–FEA two-way coupling method for predicting ship wave loads and hydroelastic responses. Applied Ocean Research. 117, 102919. https://doi.org/10.1016/j.apor.2021.102919

[10] Takami, T., Iijima, K., 2020. Numerical investigation into combined global and local hydroelastic response in a large container ship based on two-way coupled CFD and FEA. Journal of Marine Science and Technology. 25(2), 346-362. https://doi.org/10.1007/s00773-019-00668-7

[11] El Moctar, O., Ley, J., Oberhagemann, J., Schellin, T., 2017. Nonlinear computational methods for hydroelastic effects of ships in extreme seas. Ocean Engineering. 130, 659-673. https://doi.org/10.1016/j.oceaneng.2016.11.037

[12] Der Kiureghian, A., 2000. The geometry of random vibrations and solutions by FORM and SORM. Probabilistic Engineering Mechanics. 15(1), 81-90. https://doi.org/10.1016/S0266-8920(99)00011-9

[13] Jensen, J. J., 2009. Stochastic procedures for extreme wave load predictions–wave bending moment in ships. Marine Structures. 22(2), 194-208. https://doi.org/10.1016/j.marstruc.2008.08.001

[14] Garrè, L., Der Kiureghian, A., 2010. Tail-equivalent linearization method in frequency domain and application to marine structures. Marine Structures. 23(3), 322-338. https://doi.org/10.1016/j.marstruc.2010.07.006

[15] Choi, J. H., Jensen, J. J., Nielsen, U. D., 2019, September. Estimation of Extreme Roll Motion Using the First Order Reliability Method. In: Practical Design of Ships and Other Floating Structures, Springer, Singapore. pp. 682-690. DOI: 10.1007/978-981-15-4624-2_41

[16] Pal, S. K., Ono, T., Iijima, K., 2020. An Efficient Method for Prediction of the Tail of Probability of Exceedance of Vertical Bending Moment in a Ship Based on Nonlinear Time-Domain Simulations. In: The 30th International Ocean and Polar Engineering Conference, Virtual.

[17] Seng, S., Jensen, J. J., 2013, October. An application of a free surface CFD method in the short-term extreme response analysis of ships. In: Proceedings of PRADS. pp. 20-25.

[18] Takami, T., Komoriyama, Y., Ando, T., Ozeki, S., Iijima, K., 2020. Efficient FORM-based extreme value prediction of nonlinear ship loads with an application of reduced-order model for coupled CFD and FEA. Journal of Marine Science and Technology. 25(2), 327-345. https://doi.org/10.1007/s00773-019-00667-8

[19] Van Gunsteren, F. F., 1978. Springing of ships waves. Doctoral thesis, TU Delft. http://resolver.tudelft.nl/uuid:9872113e-381e-4c4d-9a74-f0253291c3b8

[20] Pal, S. K., Iijima, K., Tatsumi, A., Fujikubo, M., Takami, T., 2021. Experimental and numerical investigation of high frequency vibrations in segmented ship model using one-way coupling of CFD and FEM. In: Developments in the Analysis and Design of Marine Structures: Proceedings of the 8th International Conference on Marine Structures, Trondheim, Norway. p. 38. DOI: 10.1201/9781003230373-5

[21] Pal, S. K., Iijima, K., 2022. Investigation of Springing Responses to High Harmonics of Wave Loads by Direct Coupling Between CFD and FEM. In: Proceedings of International Conference on Ocean, Offshore and Arctic Engineering, Hamburg, Germany.

[22] Caldwell, J.B. 1965. Ultimate Longitudinal Strength. Trans Royal Inst Nav Arch 107:411-430.

[23] Masaoka, K. & Okada, H. 2003. A numerical approach for ship hull girder collapse behavior in waves. Proceedings of the 13th international offshore and polar engineering conference, Honoluliu, Hawaii, USA:369-375

[24] Yao, T. & Nikolov, P.I. 1992. Progressive collapse analysis of a ship's hull girder under longitudinal bending (2nd Report). J Soc Nav Arch Jpn 172:437-446.

[25] Smith, C. S. 1977. Influence of Local Compressive Failure on Ultimate Longitudinal Strength of a Ship's Hull. Proc. PRADS, A-10, Tokyo, Japan, pp. 72-79.

[26] Xu, W., Iijima, K., Fujikubo, M. 2011. Investigation into post-ultimate strength behavior of ship's hull girder in waves by analytical solution. In International Conference on Offshore Mechanics and Arctic Engineering, Vol. 44342, pp. 455-462.
[27] Iijima, K., Kimura, K., Xu, W., Fujikubo, M. 2011. Hydroelasto-plasticity approach to predicting the post-ultimate strength behavior of a ship's hull girder in waves. Journal of marine science and technology;16(4):379-89.
[28] Pei, Z., Iijima, K., Fujikubo, M., Tanaka, S., Okazawa, S., Yao, T. 2015. Simulation on progressive collapse behaviour of whole ship model under extreme waves using idealized structural unit method. Marine Structures;40:104-33.
[29] Han, H. K. H., Tatsumi, A., Iijima, K., Fujikubo, M. 2020. Collapse Analysis of Ship Hull Girder Using Hydro-Elastoplastic Beam Model: Part 2. In International Conference on Offshore Mechanics and Arctic Engineering, Vol. 84331, p. V02BT02A032.
[30] SIEMENS, "Simcenter STAR-CCM+-User Guide(html)", 2019
[31] Livermore Software Technology Corporation, LS-DYNA THEORY MANUAL. R10.0 (2017).
[32] Irons, B.M. and Tuck, R.C., 1969. A version of the Aitken accelerator for computer iteration. International Journal for Numerical Methods in Engineering, 1(3), pp.275-277.
[33] Oberhagemann, J., 2017. On prediction of wave-induced loads and vibration of ship structures with finite volume fluid dynamic methods. Doctoral dissertation, Universität Duisburg-Essen.
[34] Jensen J.J. and Capul, J., 2006. Extreme response predictions for jack-up units in second order stochastic waves by FORM. Probabilistic Engineering Mechanics, 21(4):330-337.
[35] International Association of Classification Societies, 2015. Longitudinal Strength Standard for Container Ships. London, UK.
[36] Jagite, G., Bigot, F., Derbanne, Q., Malenica, Š., Le Sourne, H. and Cartraud, P., 2021. A parametric study on the dynamic ultimate strength of a stiffened panel subjected to wave-and whipping-induced stresses. Ships and Offshore Structures, 16(9), pp.1025-1039.